

Electronic Theses and Dissertations, 2004-2019

2011

Perceptual Image Quality Of Launch Vehicle Imaging Telescopes

Joshua K. Lentz
University of Central Florida

 Part of the [Electromagnetics and Photonics Commons](#), and the [Optics Commons](#)
Find similar works at: <https://stars.library.ucf.edu/etd>
University of Central Florida Libraries <http://library.ucf.edu>

This Doctoral Dissertation (Open Access) is brought to you for free and open access by STARS. It has been accepted for inclusion in Electronic Theses and Dissertations, 2004-2019 by an authorized administrator of STARS. For more information, please contact STARS@ucf.edu.

STARS Citation

Lentz, Joshua K., "Perceptual Image Quality Of Launch Vehicle Imaging Telescopes" (2011). *Electronic Theses and Dissertations, 2004-2019*. 1864.
<https://stars.library.ucf.edu/etd/1864>

PERCEPTUAL IMAGE QUALITY OF LAUNCH
VEHICLE IMAGING TELESCOPES

by

JOSHUA K. LENTZ

B.S. East Stroudsburg University of Pennsylvania, 2004

B.A. East Stroudsburg University of Pennsylvania, 2004

M.S. University of Central Florida, 2008

A dissertation submitted in partial fulfillment of the requirements
for the degree of Doctor of Philosophy
in the Center for Research and Education in Optics and Lasers
in the College of Optics
at the University of Central Florida
Orlando, Florida

Summer Term
2011

Major Professor: James E. Harvey

© 2010 Joshua K. Lentz

ABSTRACT

A large fleet (in the hundreds) of high quality telescopes are used for tracking and imaging of launch vehicles during ascent from Cape Canaveral Air Force Station and Kennedy Space Center. A maintenance tool has been development for use with these telescopes. The tool requires rankings of telescope condition in terms of the ability to generate useful imagery. It is thus a case of ranking telescope conditions on the basis of the perceptual image quality of their imagery.

Perceptual image quality metrics that are well-correlated to observer opinions of image quality have been available for several decades. However, these are quite limited in their applications, not being designed to compare various optical systems. The perceptual correlation of the metrics implies that a constant image quality curve (such as the boundary between two qualitative categories labeled as excellent and good) would have a constant value of the metric. This is not the case if the optical system parameters (such as object distance or aperture diameter) are varied.

No published data on such direct variation is available and this dissertation presents an investigation made into the perceptual metric responses as system parameters are varied. This investigation leads to some non-intuitive conclusions. The perceptual metrics are reviewed as well as more common metrics and their inability to perform in the necessary manner for the research of interest. Perceptual test methods are also reviewed, as is the human visual system.

Image formation theory is presented in a non-traditional form, yielding the surprising result that perceptual image quality is invariant under changes in focal length if the final displayed image remains constant.

Experimental results are presented of changes in perceived image quality as aperture diameter is varied. Results are analyzed and shortcomings in the process and metrics are discussed. Using the test results, predictions are made about the form of the metric response to object distance variations, and subsequent testing was conducted to validate the predictions. The utility of the results, limitations of applicability, and the immediate ability to further generalize the results is presented.

This work is dedicated to my Lord Jesus Christ, without whom I would not have been able to pursue or complete this work. I am grateful for the ability to understand just a small part of His magnificent creation. His love and support never failed and He has provided for me through every difficulty and disappointment.

ACKNOWLEDGMENTS

I would like to thank my friends and family who supported and encouraged me through my entire college career. I would also like to acknowledge my parents and Grandmother for instilling within me old-fashioned values and an appreciation for hard work, honesty, and integrity. For that I will never be able to fully express my gratitude as it has fundamentally affected every aspect of my life.

I would also like to thank my advisor Dr. James Harvey for allowing me to pursue the research contained herein in a direction that was of interest to me. His insight yielded confidence that the research would yield results worthy of a degree, even when my confidence in it failed.

I would like to thank Dr. Glenn Boreman for his support of me through the entire program. His practical views and traditional teaching style were especially helpful in my understanding of optics.

TABLE OF CONTENTS

LIST OF FIGURES.....	X
LIST OF TABLES.....	xviii
LIST OF ACRONYMS.....	xx
1.0 INTRODUCTION	1
1.1 Motivation for this Dissertation Research	6
1.2 Technical Approach.....	8
1.3 Organization of Dissertation Content	10
2.0 HUMAN VISUAL SYSTEM	13
2.1 General Properties.....	13
2.2 The Retina.....	14
2.3 Contrast Sensitivity Function.....	15
2.4 Contrast Threshold Function	19
2.5 Modulation Transfer Function.....	22
2.6 Viewing Distance	23
2.7 Conversion of Retinal to Spatial Frequencies	24
3.0 IMAGE QUALITY METRICS.....	26
3.1 Common Image Quality Metrics.....	26
3.1.1 Peak-to-Valley Wavefront Error	27
3.1.2 RMS Wavefront Error.....	28

3.1.3	Strehl Ratio	31
3.1.4	Fractional Enclosed Energy	34
3.1.5	1959 Tri-bar Resolution Target Test	38
3.1.6	National Imagery Interpretability Rating Scale	40
3.1.7	Johnson’s Criteria.....	43
3.1.8	General Image Quality Equation.....	44
3.2	Historical development of OTF-based metrics	46
3.3	Normalized Metrics.....	66
4.0	IMAGE FORMATION THEORY.....	70
4.1	Alternate Approach to Image Formation.....	70
4.2	Object Distance, Magnification, and Image Quality	74
5.0	PERCEPTUAL TESTING	78
5.1	Methods of Testing	79
5.2	Test Conditions	81
5.3	Categorical Sort	81
5.4	Paired Image Comparisons.....	84
5.5	Just Noticeable Differences.....	86
6.0	SIMULATED IMAGERY.....	89
6.1	Size, Resolution, Content	89
6.2	Simulation Generation	94

7.0 RESEARCH ASSUMPTIONS	97
7.1 General Assumptions	98
7.2 Computer Modeling Assumptions	101
7.3 Perception/ Perceptual Testing Assumptions	103
8.0 FOCAL LENGTH INVARIANT PERCEIVED IMAGE QUALITY.....	106
8.1 Perceptual Testing	108
8.2 Experimental Data	110
8.3 Data Analysis	114
9.0 THRESHOLDS FOR CHANGES IN APERTURE DIAMETER.....	117
9.1 Perceptual Testing	117
9.2 Experimental Data	119
9.3 Data Analysis	127
9.4 Threshold Adjustments.....	133
10.0 THRESHOLDS FOR CHANGES IN OBJECT RANGE	135
10.1 Perceptual Testing	135
10.2 Experimental Data	135
10.3 Data Analysis	139
11.0 SUMMARY AND CONCLUSIONS.....	145
REFERENCES.....	151

LIST OF FIGURES

Figure 1. Left, Two DOAMS telescopes in a common mount. In this configuration, the telescopes typically had different focal lengths. Right, a DOAMS facility.	1
Figure 2. Space Shuttle Challenger after exploding minutes into its flight. All persons on board perished.	3
Figure 3. Launch imagery of the Space Shuttle Challenger during liftoff, showing evidence of unexpected black smoke (circled) emitted from the side of one of the solid rocket boosters.	3
Figure 4. Launch imagery of the Space Shuttle Challenger shortly before exploding, showing evidence of unexpected flame (circled) emitted from the side of one of the solid rocket boosters.	4
Figure 5. Space Shuttle Columbia's disintegration upon reentry.	4
Figure 6. Left, Space Shuttle Columbia during liftoff. Right, foam debris causing damage to the vehicle's heat shield.	5
Figure 7. Flow chart of the testing and maintenance process of the TIME Tool.	6
Figure 8. Simplified "ranking" system of the TIME Tool used to describe the image quality or usefulness of imagery to analysts.	8
Figure 9. The human eye showing important dimensions (in mm) and refractive indices.	13
Figure 10. Contrast Sensitivity Function for display brightness values of 10, 75, 100, and 140 cd/m ²	17
Figure 11. Contrast Sensitivity Function for picture areas of 5, 10, 15, and 20 degrees.	17

Figure 12. Logarithmic plot of the Contrast Sensitivity Function for display brightness values of 10, 75, 100, and 140 cd/m ²	18
Figure 13. Logarithmic plot of the Contrast Sensitivity Function for picture areas of 5, 10, 15, and 20 degrees.....	18
Figure 14. Contrast Threshold Function for display brightness values of 10, 75, 100, and 140 cd/m ²	20
Figure 15. Contrast Threshold Function for picture areas of 5, 10, 15, and 20 degrees.....	21
Figure 16. Logarithmic plot of the Contrast Threshold Function for display brightness values of 10, 75, 100, and 140 cd/m ²	21
Figure 17. Logarithmic plot of the Contrast Threshold Function for picture areas of 5, 10, 15, and 20 degrees.	22
Figure 18. The geometry for converting between spatial frequencies in the observation plane and angular frequencies at the retina.....	24
Figure 19. Two images degraded with equal RMS wavefront error (0.4λ) when the aberration is balanced spherical aberration (left) and balanced astigmatism (right).....	31
Figure 20. Diffraction-limited fractional encircled energy for several obscuration ratios.....	34
Figure 21. Fractional encircled energies for an obscuration ratio of 0.3 with of 0λ, 0.5λ, 1.0λ, 1.5λ, and 2.0λ of defocus.	35
Figure 22. Fractional encircled energies for an obscuration ratio of 0.3 with 0.0λ, 0.5λ, 1.0λ, and 1.5λ, of spherical aberration, each balanced with defocus to minimize RMS wavefront error.	36

Figure 23. Fractional encircled energies for an obscuration ratio of 0.3 and 1λ each of spherical aberration, coma and astigmatism, each balanced appropriately to minimize RMS wavefront error.....36

Figure 24. 1959 Tri-Bar Resolution Target.....38

Figure 25. Three bar target simulations for a DOAMS telescope with 1.5λ of astigmatism at the vertical focus (left), medial focus (center) and horizontal focus (right). The circled regions provide a good reference to compare. The image with the vertical focus (left) has the best vertical bar resolution. Likewise, the image with the horizontal focus (right) has the best horizontal bar resolution. The medial focus provides the best compromise for normal imaging applications.39

Figure 26. Measured MTF (Left), MTF^2 (Center), and idealized MTF^2 (Right) with the same area as that of the measured MTF^247

Figure 27. An MTF curve (solid curve) and contrast threshold function (dotted curve). The MTFA would then be the total integrated area between the two curves up to the point of intersection.52

Figure 28. A long-range imaging device creates a non-ideal replication of an object on an image plane (red line) which is displayed visually with some display magnification. The display is then viewed by an observer from a viewing distance d71

Figure 29. Objects represented as 100% contrast black bars are convolved with a PSF.....74

Figure 30. As the width of a feature decreases relative to the PSF width, image contrast decreases and blur becomes more dramatic.....75

Figure 31. Simulated imagery for an object range of 5 miles with the presence of 0.5λ of balanced astigmatism (Left) and 0.75λ of balanced astigmatism (Right).76

Figure 32. Simulated imagery for an object range of 30 miles with the presence of 0.5λ of balanced astigmatism (Left) and 0.75λ of balanced astigmatism (Right).76

Figure 33. Simulated imagery for an object range of 60 miles with the presence of 0.5λ of balanced astigmatism (Left) and 0.75λ of balanced astigmatism (Right).77

Figure 34. Standard analysis of perceptual test data yields a scale value for each “image point” and scale values corresponding to category cutoffs. Using the linear relationship, boundary cutoffs can be converted to metric values.83

Figure 35. Hypothetical results of perceptual image quality testing at three data points.84

Figure 36. A sample pair of images presented to an observer in the paired image comparison test. The observer’s task is to select which image of the pair is of higher quality.84

Figure 37. Just Noticeable Differences are determined from a sequence of paired comparisons. The reference image (outlined in red) is paired with each of the remaining 6 test images, creating six pairs of images.....85

Figure 38. After a sequence of image pairs has been presented to a group of observers, the fractional selection of the reference image over the test image is determined for the group. The change in image attribute necessary to generate a 0.75 fractional selection defines the Just Noticeable Difference of that attribute, here, about 0.25 units.87

Figure 39. Image of the Space Shuttle Atlantis on the pad, used extensively throughout perceptual tests conducted for this research. The image is shown here at 50% of its actual 8”×10” size.....91

Figure 40. House with fence image used in paired image comparisons. This image shown at actual size.....92

Figure 41. Trees image used in paired image comparisons. This image is shown at actual size. 93

Figure 42. House with shrub image used in paired image comparisons. This image is shown at actual size.....94

Figure 43. Left to Right, a bitmap image representing the “object” , is split into its red, green, and blue constituent color planes, each color plane is convolved with a single monochromatic PSF. The color planes are recombined into a single output bitmap file representing the “image”.....96

Figure 44. MTF curves for obscuration ratios of 0.3 (solid curves) and 0.35 (dashed curves) for diffraction-limited, 1.25λ of balanced spherical aberration, and 2λ of balanced spherical aberration.103

Figure 45. MTF curves for $f=200''$, and $f=400''$ are identical. (a) CTF curves vary for fixed display magnification (M). (b) CTF curves are identical when the display magnification (M) is varied in reciprocal proportion to the change in optical magnification (m).....107

Figure 46. Although a shorter focal length yields a smaller PSF, the smaller resulting magnification creates a smaller geometrical image. The result is a PSF which is the same size relative to image features as for a larger focal length. The focal length then does not affect image content.....107

Figure 47. Fractional selection of the reference image as having higher usefulness for the HQ house/fence data set.111

Figure 48. Fractional selection of the reference image as having higher usefulness for the HQ trees data set.....	112
Figure 49. Fractional selection of the reference image as having higher usefulness for the LQ trees data set.....	113
Figure 50. Fractional selection of the reference image as having higher usefulness for the LQ house/shrub data set.....	114
Figure 51. Normalized SQRI (SQRI norm) boundary values resulting from categorical sort testing for aperture diameter trends. Solid curves are inversely proportional to the aperture diameter with excellent R^2 values.....	120
Figure 52. Normalized TTP (TTP norm) boundary values resulting from categorical sort testing for aperture diameter trends. Solid curves are proportional to the aperture diameter with excellent R^2 values.	121
Figure 53. SQRI boundary values resulting from categorical sort testing for aperture diameter trends. Solid curves are cubic with excellent R^2 values.	122
Figure 54. TTP boundary values resulting from categorical sort testing for aperture diameter trends. Solid curves are quadratic with excellent R^2 values.....	124
Figure 55. SQF boundaries resulting from categorical sort testing for aperture diameter trends. Solid curves are cubic curves with excellent R^2 values.....	125
Figure 56. Relative spatial frequency weighting functions for the SQRI, TTP, and SQF.....	129
Figure 57. MTF curves for 24 inch and 30 inch diameter telescopes at diffraction limit, and in the presence of aberrations. Also shown is the SQRI spatial frequency weighting function (bold dashed curve).	132

Figure 58. TTP boundary curves (solid lines) modified to asymptotically approach the horizontal axis (dashed segments).133

Figure 59. TTPnorm boundary curves (solid lines) modified to reflect the expected asymptotic behavior in as the boundaries approach the horizontal axis (dashed segments).134

Figure 60. SQRI boundary curves (solid lines) modified to asymptotically approach the horizontal axis (dashed segments).134

Figure 61. SQRI boundary values resulting from categorical sort testing for object range trends. The data appears linear and is fitted with lines.136

Figure 62. TTP boundary values resulting from categorical sort testing for object range trends appears linear and is fitted with lines.137

Figure 63. SQF boundary values resulting from categorical sort testing for object range trends appears linear and is fitted with lines.138

Figure 64. Predicted boundary curve forms of the SQRInorm.140

Figure 65. Predicted boundary curve forms of the TTPnorm shown with third order polynomial approximations.141

Figure 66. Predicted boundary curve forms of the SQF shown with third order polynomial approximations.142

Figure 67. TTPnorm data shown with predicted curve form best fit polynomials.143

Figure 68. SQF data shown with predicted curve form best fit polynomials.144

Figure 69. Perceptual image quality boundary curves for spherical aberration as a function of aperture diameter.148

Figure 70. Perceptual image quality boundary curves for spherical aberration as a function of object distance149

LIST OF TABLES

Table 1. Summary of the Eastern Range launch vehicle imaging telescopes.	2
Table 2. Peak-to-Valley wavefront expressions for annular apertures. The right-most column provides the simplified expressions for the case of a circular pupil.....	28
Table 3. Combinations of aberrations to minimize RMS wavefront error along with the resulting minimum RMS wavefront error.....	29
Table 4. Theoretical RMS Wavefront Error expressions derived from Equation (5-2).....	30
Table 5. Theoretical expressions for the Strehl Ratio of balanced aberrations.	32
Table 6. Theoretical expressions for Strehl Ratio of pure aberrations.....	33
Table 7. Selected portions illustrating the type of task required to achieve a rating level for the October 1995 Civil National Imagery Interpretability Rating Scale [8].	42
Table 8. SMT Acutance value correlates.	49
Table 9. Object and PSF widths (arbitrary units) and resulting image contrast for the illustrations of Figure 29 and Figure 30.....	75
Table 10. Example of a data matrix resulting from Categorical Sort Testing. Columns correspond to categories and rows correspond to images.....	82
Table 11. Paired comparison data. The left column is the attribute value, the right is the number of times the reference image was selected by the group.....	86
Table 12. Parameters used for simulating the four data sets used in paired image comparisons.	108
Table 13. Summary of the results of data presented in the previous section.	114
Table 14. Coefficients of cubic curves fit to the SQRI data shown in Figure 53.....	123

Table 15. Coefficients of cubic curves fit to the TTP data shown in Figure 54.....	124
Table 16. Coefficients of quartic curves fit to the SQF data shown in Figure 55.	126
Table 17. Summary of boundary forms for each of the metrics investigated.	127
Table 18. Summary of spatial frequency weighting for the metrics of interest.	128
Table 19. SQRI _{norm} slopes and constants resulting from the data fitting shown in Figure 61 with resulting coefficients of determination listed.....	136
Table 20. TTP _{norm} slopes and constants resulting from the data fitting shown in Figure 62 with resulting coefficients of determination listed.....	137
Table 21. SQF slopes and constants resulting from the data fitting shown in Figure 63 with resulting coefficients of determination listed.....	138
Table 22. Diameters at a constant range (left column) are converted to ratios of diameter to range (center column), from which corresponding ranges can be found for a constant diameter (right column).....	140
Table 23. Resulting second order polynomial curves from fitting to the data.	143
Table 24. Resulting third order polynomial curves from fitting to the data.....	144

LIST OF ACRONYMS

ASF – Amplitude Spread Function

ATOTS – Advanced Transportable Optical Tracking System

COTS – Commercial Off The Shelf

CREOL – Center for Research and Education in Optics and Lasers

CRT – Cathode Ray Tube

CSF – Contrast Sensitivity Function

CTF -- Contrast Threshold Function

DOAMS -- Distant Object Attitude Measurement System

GIQE -- General Image Quality Equation

GSD – Ground Sample Distance

HVS – Human Visual System

IIRS – Image Interpretability Rating System

IQI – Image Quality Index

ISV – Image Sharpness Value

JND – Just Noticeable Difference

LVIT – Launch Vehicle Imaging Telescope

MIGOR – Mobile Intercept Ground Optical Recorder

MSE – Mean Square Error

MTF – Modulation Threshold Function

MTFA – Modulation Threshold Function Area

MTFV – Modulation Threshold Function Volume

NIIRS – National Image Interpretability Rating Scale

OTF – Optical Transfer Function

PMTF – Polychromatic Modulation Threshold Function

PSF – Point Spread Function

RER – Relative Edge Response

RMS – Root Mean Square

RMSE – Root Mean Square Error

ROTI -- Recording Optical Tracking Instrument

SLRS – Space Lift Range Systems

SMTA -- System Modulation Transfer Acutance

SNR – Signal to Noise Ratio

SQF – Subjective Quality Factor

SQRI – Square Root Integral

TIME Tool – Telescope Interferometric Maintenance Evaluation Tool

TQF – Threshold Quality Factor

TTP – Targeting Task Performance

UIQI – Universal Image Quality Index

UQI -- Universal Image Quality Index

1.0 INTRODUCTION

In the 1960s, during the era known as the “space race”, a set of telescopes was designed and constructed for the sole purpose of tracking and monitoring launch vehicles. The telescopes were of exceptional quality and allowed various tasks to be accomplished. Larger telescopes like the Advanced Transportable Optical Tracking System (ATOTS), the Distant Object Attitude Measurement System (DOAMS) such as shown in Figure 1, and the Mobile Intercept Ground Optical Recorder (MIGOR) were typically used for detailed monitoring or tracking of vehicles during ascent. Smaller telescopes like the Cinetheodolite, Davro, and Questar were commonly used as sighting telescopes for the larger systems. Initially, more than 200 total telescopes were constructed and placed in service. Table 1 summarizes the telescopes and their configurations.



*Reproduced from <http://www.nasa.gov>

Figure 1. Left, Two DOAMS telescopes in a common mount. In this configuration, the telescopes typically had different focal lengths. Right, a DOAMS facility.

Table 1. Summary of the Eastern Range launch vehicle imaging telescopes.

Telescope	Built	In Service	Diameter	Focal Length	Configuration
ATOTS	unknown	unknown	18"	180", 400", 500"	Cassegrain
Cine.	150	55	7"	60", 120"	Folded Catadioptric Refractor
Davro	unknown	unknown	7"	100", 120"	Schmidt-Cassegrain
DOAMS	25	12	24"	400", 200"	Cassegrain
MIGOR	≥ 3	3	18"	90", 180", 360", 500"	Ross-Corrected Newtonian
Questar	unknown	unknown	7"	120"	Schmidt-Cassegrain
ROTI	unknown	unknown	24"	100", 200", 300", 400", 500"	Newtonian

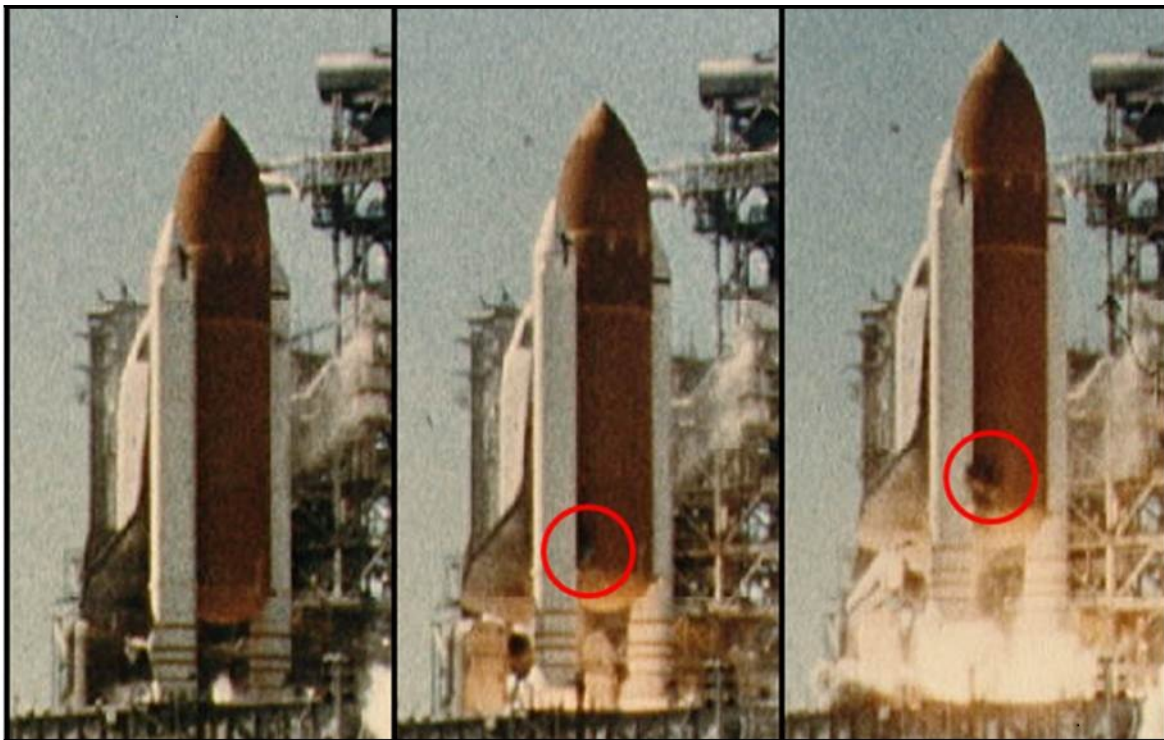
As technology progressed, launch vehicles became more complex and their maintenance followed suit. However, the launch vehicle tracking and imaging telescopes remained with little or no maintenance. Coatings on optics deteriorated in the particularly humid Florida climate and any realignments and other maintenance performed were left undocumented, and in some cases, unperformed.

On January 28, 1986, the Space Shuttle Challenger exploded only minutes into its flight. The source of failure that led to the disaster was visible through the telescopes during liftoff (Figure 3) and throughout the ascent (Figure 4), revealing the importance of high quality imagery in recognizing atypical vehicle behavior. However, maintenance procedures for the tracking and imaging telescopes remained unchanged.



*Reproduced from <http://www.nasa.gov>

Figure 2. Space Shuttle Challenger after exploding minutes into its flight. All persons on board perished.



*Reproduced from <http://www.nasa.gov>

Figure 3. Launch imagery of the Space Shuttle Challenger during liftoff, showing evidence of unexpected black smoke (circled) emitted from the side of one of the solid rocket boosters.



*Reproduced from <http://www.nasa.gov>

Figure 4. Launch imagery of the Space Shuttle Challenger shortly before exploding, showing evidence of unexpected flame (circled) emitted from the side of one of the solid rocket boosters.

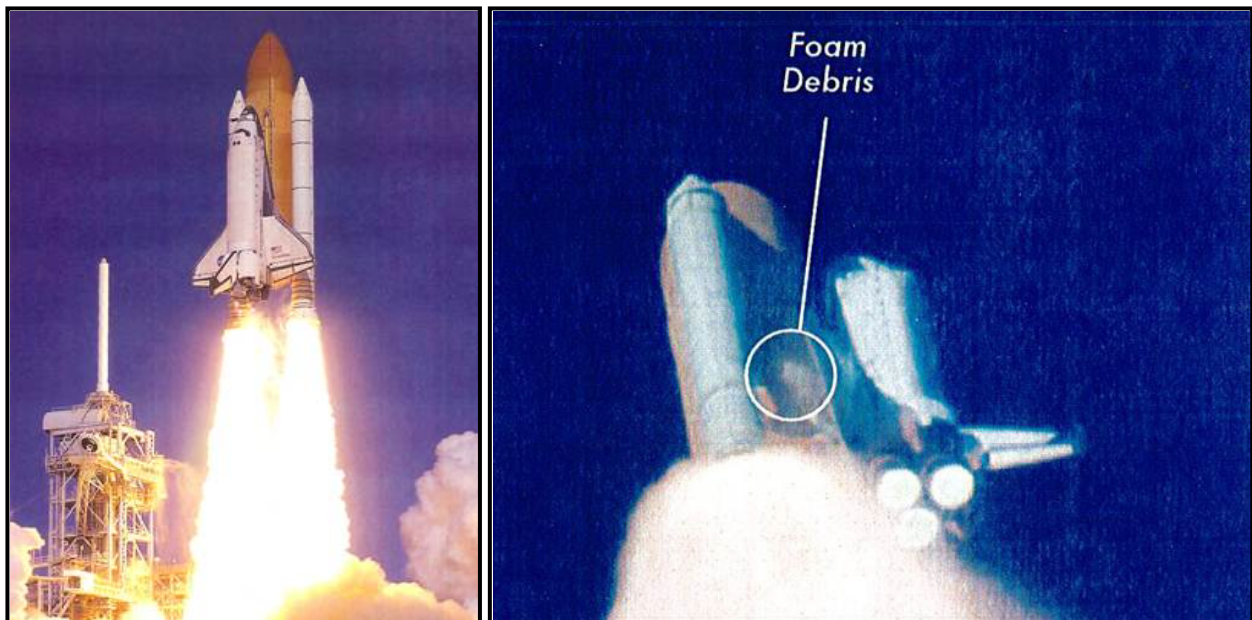
On February 1, 2003, the Space Shuttle Columbia disintegrated on reentry to the earth's atmosphere (Figure 5).



*Reproduced from <http://www.nasa.gov>

Figure 5. Space Shuttle Columbia's disintegration upon reentry.

The ensuing investigation revealed foam debris damaging the heat shield during ascent (Figure 6). The source of the damage was visible through the telescopes, again revealing the importance of high quality tracking and imaging devices. After this tragedy, a major review of the condition of the telescopes was investigated and a maintenance process was developed. This maintenance process is a multi-level baseline, measurement, and prediction process known as the Telescope Interferometric Maintenance Evaluation (TIME) Tool.



*Reproduced from <http://www.nasa.gov>

Figure 6. Left, Space Shuttle Columbia during liftoff. Right, foam debris causing damage to the vehicle's heat shield.

1.1 Motivation for this Dissertation Research

In November 2000 ITT Space Systems was awarded a contract to modernize the U. S. Air Force Spacelift Range System (SLRS). The SLRS contract provides the Department of Defense, NASA, and commercial customers with a highly reliable, integrated system to support space missions including spacecraft launch, ballistic missile and aeronautical testing. The initial award was for \$81.2 million with total contract value expected to be \$1.3 billion over the 10-year contract period. For the period of 2005 through 2010, the Optical Design and Image Analysis Laboratory at CREOL supported ITT in that task, specifically in development of the maintenance methodology and implementation, software to simulate images degraded by telescopes, and establishment of well-defined perceptual metric thresholds for any eastern range telescope.

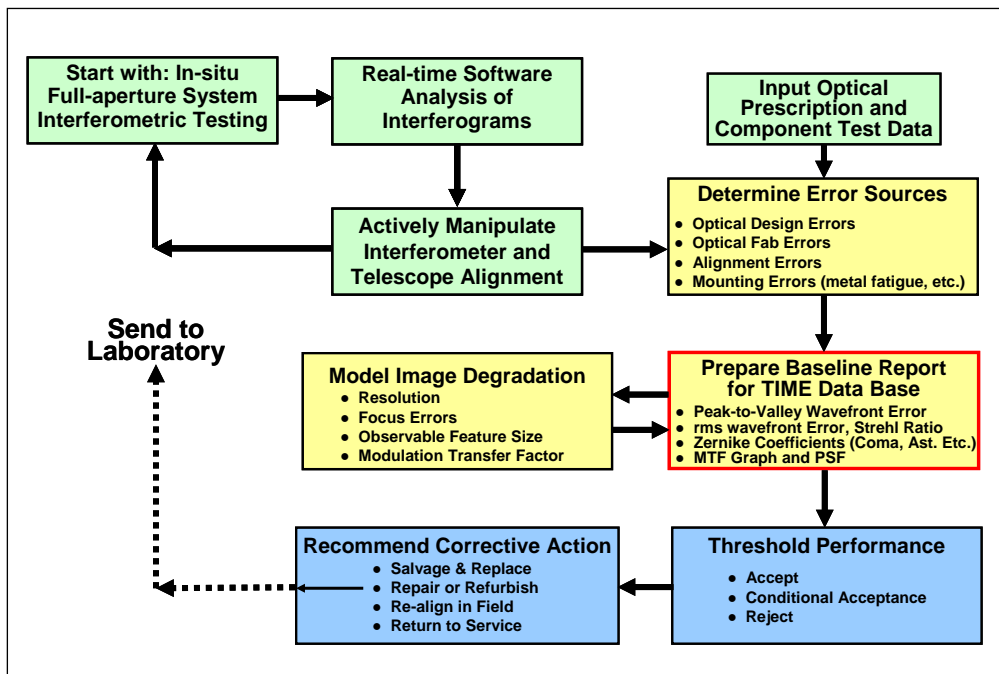


Figure 7. Flow chart of the testing and maintenance process of the TIME Tool.

The TIME Tool process developed for preservation of the fleet of launch vehicle imaging telescopes (LVIT) is a multi-stage process summarized in Figure 7. The process begins with in-situ, full-aperture interferometric testing. The telescope and interferometer are aligned and the aberrations are minimized through an iterative process. The remaining aberrations are compared with the optical prescription and component test data to determine the sources of the aberrations. The sources can be design errors, fabrication errors, alignment errors or mounting errors. In some cases, depending on the error sources determined, little or no compensation can be made for the remaining aberrations. Next, a TIME Database report is prepared based on the measured wavefront errors, Strehl Ratio, aberration coefficients, the point spread function (PSF) and the modulation transfer function (MTF) and including a digitally simulated image as would be generated by the telescope in its current condition.

Several perceptual image quality metrics are computed and used in conjunction with perceptual image quality test results to establish a simplified “ranking” of the telescope’s condition in terms of its ability to provide imagery useful to analysts and photo-interpreters.

Based on the ranking, the telescope is left in service, used conditionally based on performance objectives and task requirements, or removed from service. Telescopes removed from service will likely undergo a complete refurbishment in an attempt to restore it to a usable condition. If this fails, salvage and/or replacement is likely.

Descriptor	Numerical Ranking	Associated Color Code	
Excellent	5	Blue	} Ready for use
Good	4	Green	
Fair	3	Yellow	} Conditional use
Poor	2	Orange	
Unusable	1	Red	} Remove from service

Figure 8. Simplified “ranking” system of the TIME Tool used to describe the image quality or usefulness of imagery to analysts.

The methodology was developed and refined to that described, but it had one serious deficiency—there was no ability to quantitatively define thresholds for the image quality rankings desired, with an application to launch imagery analysis. This was complicated by a desire for the capability of comparing the quality of one telescope to that of another with potentially different parameters such as focal length or aperture diameter. The need to develop such thresholds for the necessary parameters motivated the research presented in this dissertation.

1.2 Technical Approach

Establishing the necessary image quality thresholds required investigation into the manner in which focal length, aperture diameter, obscuration ratio, and object distance affected the perceived quality of imagery. The perceptual nature of the imagery dictated that perceptual testing be employed, not to create any new perceptual metrics, but rather, to investigate their

behavior as parameters varied. The perceptual testing required images created from a variety of parameters as well as in the presence of varying quantities of aberrations. To accomplish this, software was developed to synthetically generate images with freedom to select parameters and aberrations as necessary. Though simulation of degraded images was not new at the time of the research, no Commercial Off The Shelf (COTS) software was available that allowed the necessary control in simulations. An overview of the manner in which the software operates is provided in Chapter 6, though the details are not particularly useful in the description of this research and its results.

The investigation into metric response to variation of parameters was conducted in a combination of methods including theoretical, numerical justification, and perceptual testing. The focal length parameter was investigated theoretically with experimental validation of a portion of the obtained results. The ability to consider the obscuration ratio variation inconsequential over the range of interest was established through numerical justification. The aperture diameter variation behavior was found through perceptual testing, the results of which were used to theoretically predict the behavior of thresholds as object distance is varied. This prediction was validated through experiment.

1.3 Organization of Dissertation Content

Since this dissertation is heavily dependent on human perception, Chapter 2 is dedicated to a review of pertinent aspects of the Human Visual System (HVS). General properties are described, including dimensions of the eye. Retinal properties are discussed briefly, but the majority of attention is given to the Contrast Sensitivity Function (CSFF) and Contrast Threshold Function (CTF), required in evaluation of the perceptual image quality metrics chosen for this research. A short sensitivity analysis is provided for several parameters that influence the CSF and CTF such as display brightness, picture size, and viewing distance. Finally, since the metrics are discussed in the object plane and image plane, the method for relating the CTF and CSF of the retinal plane to those planes is presented.

In Chapter 3 common image quality metrics are presented with attention given to which metrics are not useful for this application and why. A historical review of OTF-based image quality metrics is then presented, beginning with an overview of the origin of the Optical Transfer Function (OTF). Finally, the relative benefits of normalizing perceptual image quality metrics to a diffraction-limited value are presented. For contrast, a mathematical description of the shortcomings of this normalization is provided.

In Chapter 4, a less common approach to describing image formation is presented. This information is critical to later conclusions, particularly discussing the manner in which image quality decays as object distance increases. Theory as well as simulations are presented as evidence.

Chapter 5 begins with an overview of perceptual test methods and their uses. The conditions under which tests are generally performed are presented and compared to the conditions under which the perceptual testing of this research was conducted.

An overview of the process used to generate synthetic imagery is provided in Chapter 6 along with the basic images used. The image sizes, content, and resolution are provided.

As with most scientific research, some assumptions were required to make the research manageable. A reasonably exhaustive list of the most important assumptions is presented in Chapter 7, along with a discussion of the consequences expected if the assumptions are violated or invalid.

Chapter 8 presents a theoretical derivation to justify the lack of effect focal length has on perceived image quality as applied in this research. The theoretical development is provided, followed by illustrations of the underlying mechanisms, and finally, results are presented of perceptual testing used for validation.

Chapter 9 is experimental in nature, describing a perceptual test designed and conducted to establish image quality metric thresholds for the five rankings of interest (Excellent, Good, Fair, Poor, and Unusable) as aperture diameter varies. The data analysis and results are shown,

followed by a discussion of unrealizable data values and adjustments to more realistic forms of better-behaved metric and test analysis processes.

Based on the results of Chapter 9, theoretical predictions of the image quality metric thresholds are presented for the five ranking categories as object distance is varied. Following the theoretical predictions is a description of a perceptual test used to experimentally validate the predictions. The resulting data is presented, analyzed, and discussed.

The results of the research in its entirety and its ability to accomplish the desired goals are presented in Chapter 11.

2.0 HUMAN VISUAL SYSTEM

Several aspects of the human visual system are important to the application of perceptual image quality. It is impossible to discuss perceived image quality without including the human observer's optical system, composed of the eye, optic nerves, and the brain. Although color channels are a significant part of the human process of visual perception, color effects in images are not discussed in this dissertation, and are therefore not discussed.

2.1 General Properties

The adult human eye has a diameter of 24mm and a focal length in air of approximately 17.1mm, a foveal field of view of 5° and a maximum field of view of nearly 180° .

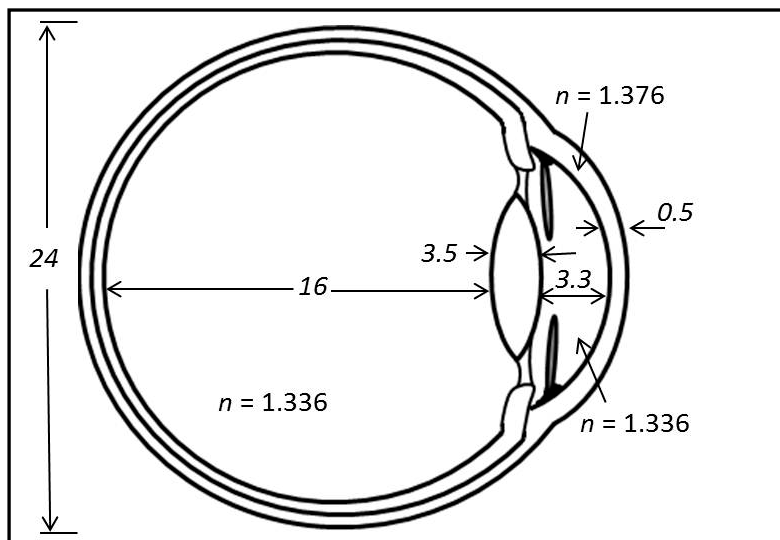


Figure 9. The human eye showing important dimensions (in mm) and refractive indices.

The pupil diameter is variable from 2mm to 8mm and has a significant impact on image quality since aberrations and diffraction are both affected by the pupillary diameter. Although smaller diameter pupils restrict the aberrations, a larger diffraction spot results which may or may not improve the quality of the image on the retina. There is then a tradeoff between aberrations and diffraction in the human eye. Furthermore, the diameter of the pupil controls the irradiance of the retinal image, affecting the signal to noise ratio, important for the detection and identification of image features.

Although the foveal field of view is limited to an angle substantially smaller than that encountered in viewing large images at a normal distance, it is this field of view that is of interest. With the rapid scanning motion of the human eye, the region of an object undergoing foveated imaging constantly moves and covers the entire image being studied. The brain then processes this information and constructs an image of overlapping foveal regions which are imaged at a much higher quality than if the eye's attention was fixed and content at larger field angles remained at its inherently lower quality.

2.2 The Retina

The retina, located at the back of the eye, performs the function of light detection. There are several layers in the retina including membranes, fibre layers, ganglion cells, etc. Of most interest in the retina though, are the two types of photoreceptors, namely the rods and cones.

The density of cones varies with angle from the fovea, the density being maximum at 0° (at the fovea) and decreasing with angle. The cones are responsible for imaging at higher illumination levels (photopic vision) and contribute little to low light imaging.

The density of rods also varies with angle from the fovea, the rod density being very low at angles both near the fovea and large angles (greater than 70°), and having a maximum density around 15° . The rods are responsible for low light level imaging (scotopic vision), providing an optimum viewing angle between 10° and 15° . Since image analysts will normally have illumination controlled environments for viewing images, light levels will undoubtedly be increased to photopic levels, leaving scotopic conditions unnecessary in analysis provided in this dissertation.

2.3 Contrast Sensitivity Function

The quality of images as perceived by a human observer is dependent on the contrast and spatial frequency of each image feature. As spatial frequency increases, the contrast required to resolve a detail is increased. At some spatial frequency, the required contrast becomes greater than unity. At this and higher frequencies, the human visual system cannot resolve a feature and it is invisible without additional magnification or contrast stretching. The ease with which an observer can resolve spatial frequencies is known as the Contrast Sensitivity Function (CSF). The CSF is also the inverse of the Contrast Threshold Function (CTF) described in the following

section. For higher values of the CSF, the human observer is more sensitive to a given spatial frequency, and less contrast is needed for such features to be visible.

The CSF is a single curve depending on the field angle and on-axis brightness. The maximum sensitivity shifts to higher spatial frequencies as the brightness increases, and the entire CSF curve shifts generally to lower values as the field angle increases. The maximum CSF curve occurs for a 0° field.

The CSF applied to calculate image quality metric values is that measured by Barten [2] , having the form shown in Equation (2-1), in which L is the display luminance and w is the square root of the picture area in degrees.

$$CTF(u_{ret}) = \frac{a}{bu_{ret}e^{-cu_{ret}}\sqrt{1+0.06e^{cu_{ret}}}} \quad (2-1)$$

Here, a, b and c are given by

$$a = \left(1 + \frac{12}{w \left(1 + \frac{u_{ret}}{3} \right)^2} \right), \quad b = \frac{540}{\left(1 + \frac{0.7}{L} \right)^{0.2}}, \quad c = 0.3 \left(1 + \frac{100}{L} \right)^{0.15} \quad (2-2)$$

Linear plots of Equation (2-1) are shown in Figure 10 as L is varied and in Figure 11 as w is varied. Logarithmic plots of equation (2-1) are shown in Figure 12 as L is varied and in Figure 13 as w is varied.

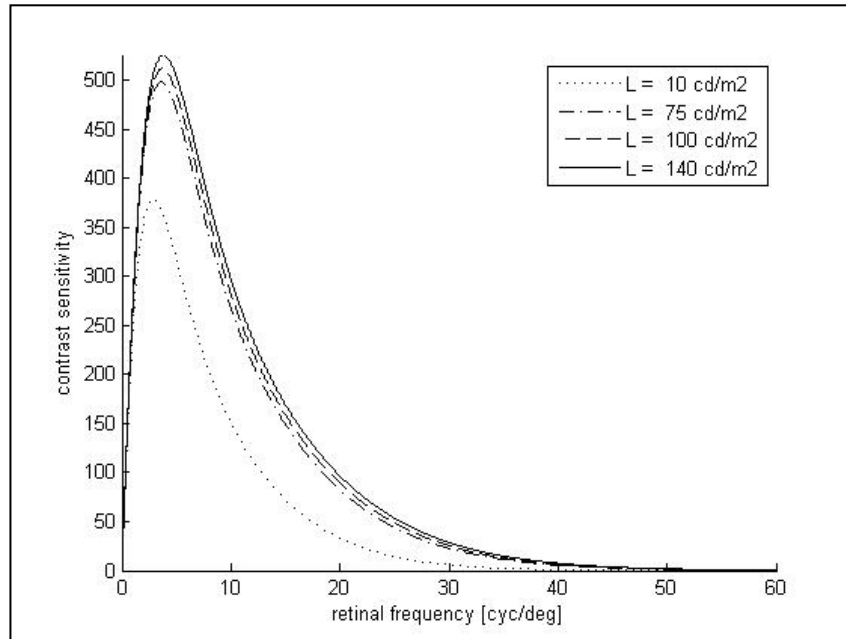


Figure 10. Contrast Sensitivity Function for display brightness values of 10, 75, 100, and 140 cd/m2.

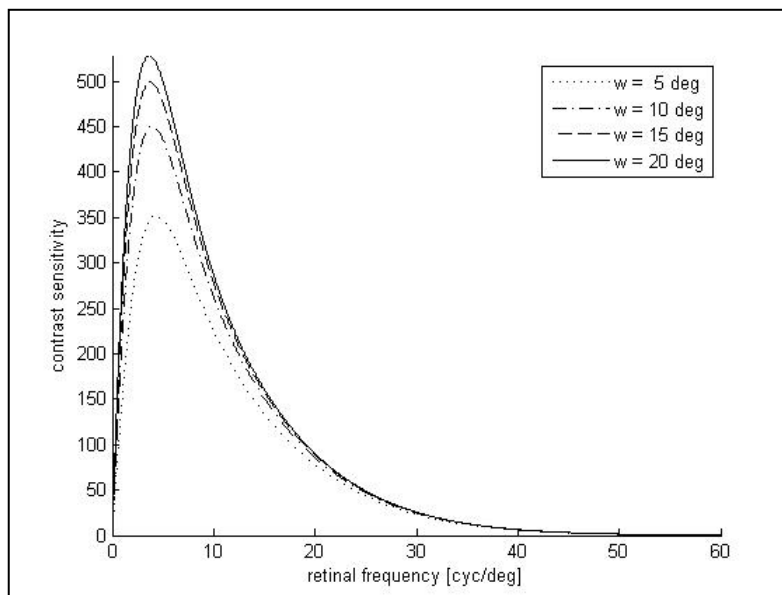


Figure 11. Contrast Sensitivity Function for picture areas of 5, 10, 15, and 20 degrees.

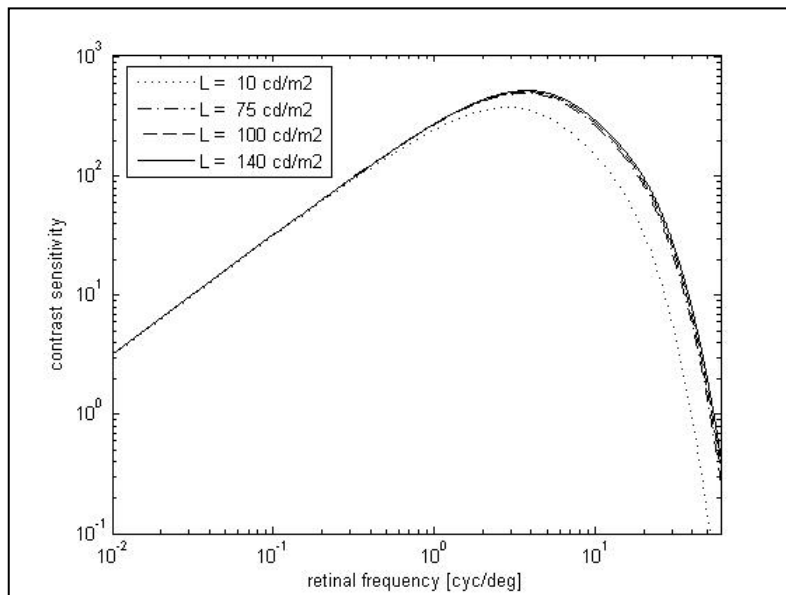


Figure 12. Logarithmic plot of the Contrast Sensitivity Function for display brightness values of 10, 75, 100, and 140 cd/m^2 .

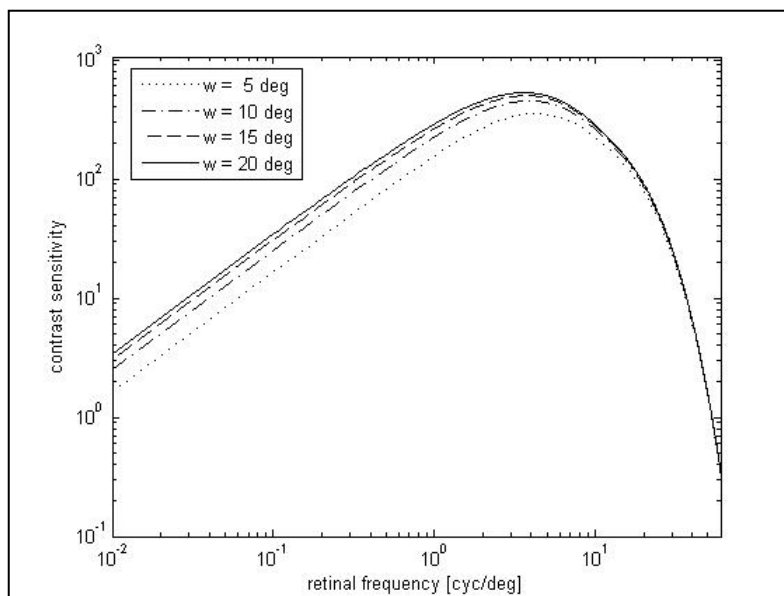


Figure 13. Logarithmic plot of the Contrast Sensitivity Function for picture areas of 5, 10, 15, and 20 degrees.

Although an asymmetric two dimensional CSF is most accurate to represent the sensitivity of the human visual system, a radially symmetric CSF was applied for simplicity. The retinal angular frequency u_{ret} of equation (2-1) is then a radial retinal angular frequency. A 100 cd/m^2 display luminance and an angular subtense of 13° is assumed based on approximate average room lighting, average viewing distance of 30 inches, and image dimensions of 5 inches by 9 inches. By applying the parameters above, the cutoff spatial frequency for the human visual system (the spatial frequency at which the CSF reaches a value of zero or the CTF reaches a value of unity) is 53.15 cyc/deg and the maximum contrast sensitivity is 441.5 and occurs at a spatial frequency of 4.5 cyc/deg.

2.4 Contrast Threshold Function

The Contrast Threshold Function (CTF) is the inverse of the Contrast Sensitivity Function (CSF) and provides the minimum contrast required to observe the presence of a given retinal frequency. This minimum contrast is a threshold contrast, yielding the functional title of Contrast Threshold Function. Since the CTF and CSF are inverses of each other, the same parameters discussed under the CSF are applied, namely a display luminance of 100 cd/m^2 and an angular subtense of 13° .

The CTF curves found from inverting the CSF curves of Figure 10 through Figure 13 are shown in Figure 14 through Figure 17.

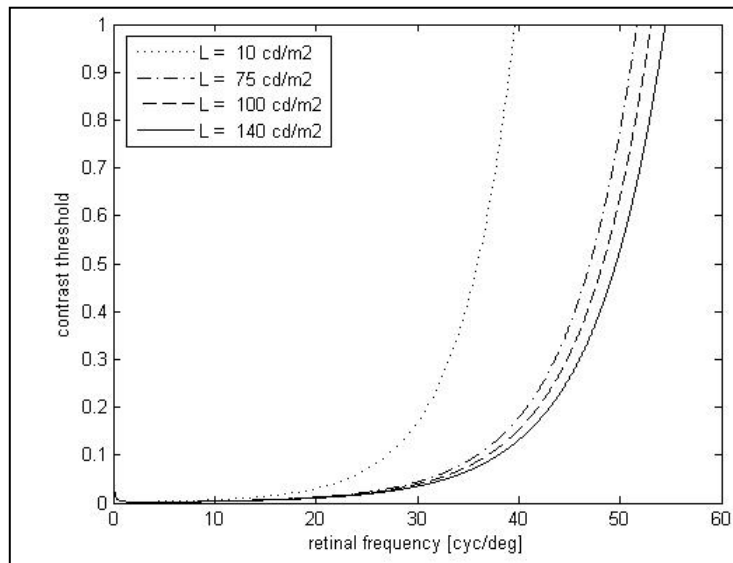


Figure 14. Contrast Threshold Function for display brightness values of 10, 75, 100, and 140 cd/m^2 .

Figure 14 reveals that for display luminances within approximately 25% of the value chosen (100 cd/m^2) the cutoff retinal frequency occurs around 53 cyc/deg and varies only about 3%. This means that the chosen CTF is fairly insensitive to changes around the selected display luminance and that the “average” conditions encountered by image analysts will be closely approximated.

Figure 15 indicates that for significant changes in image area (from 50% to 200% for the assumed $5'' \times 9''$ image size), essentially no change in the CTF occurs. The results of analysis then will be applicable to a broad range of image sizes and is not restricted to the particular size used in psychometric testing. Since w is an angle subtended by the square root of the image area, the viewing distance is inherently included in w . Thus, a significant change in viewing distance (a factor of 2 higher or lower) can be tolerated with little or no change in the CTF.

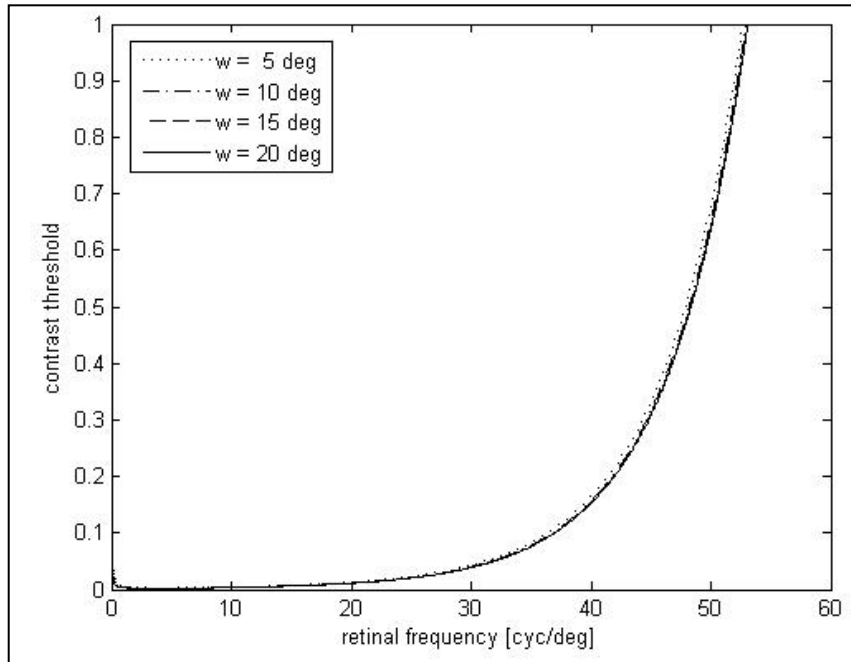


Figure 15. Contrast Threshold Function for picture areas of 5, 10, 15, and 20 degrees.

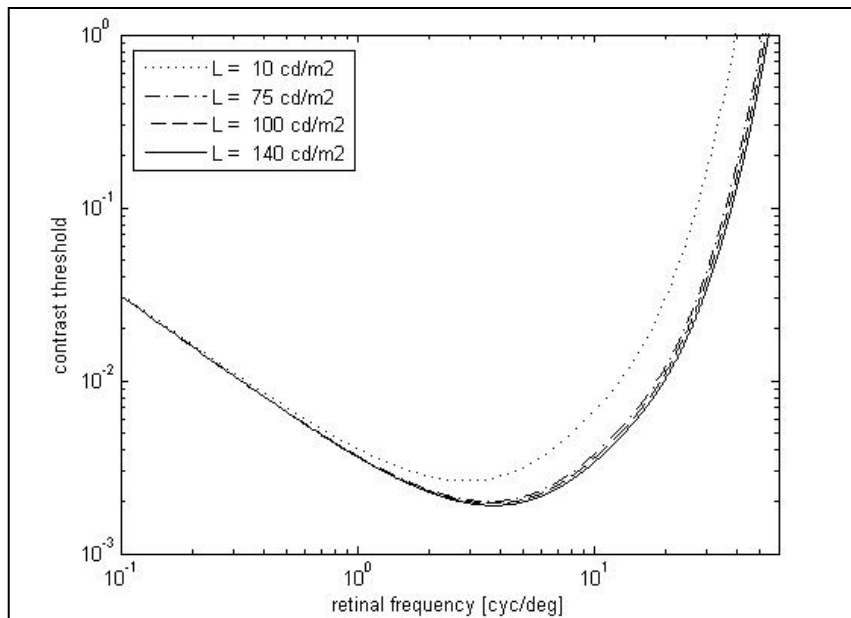


Figure 16. Logarithmic plot of the Contrast Threshold Function for display brightness values of 10, 75, 100, and 140 cd/m^2 .

This removes the requirement to fix the position of observers' heads with respect to the image in an attempt to maintain a particular viewing distance. The “average” image analyst condition model which allows observers to vary the viewing distance for their optimal viewing is supported by the indicated parametric insensitivity.

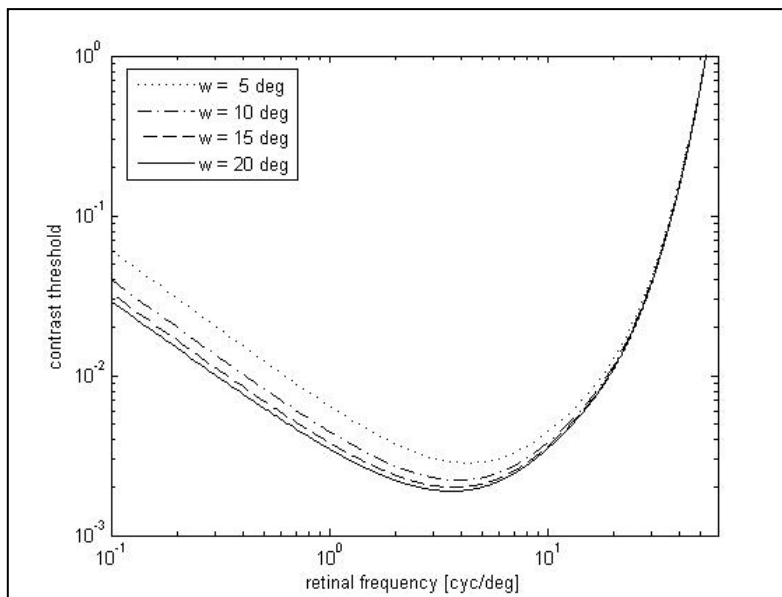


Figure 17. Logarithmic plot of the Contrast Threshold Function for picture areas of 5, 10, 15, and 20 degrees.

2.5 Modulation Transfer Function

Typically, when modeling optical systems, Modulation Transfer Functions (MTFs) are cascaded through the system, even in violation of the space invariant assumption required for such analysis. Close approximations occur, particularly if a spatially averaged MTF is used for a detector MTF. The system is then typically modeled using the optics MTF, detector MTF,

electronic transmission MTF, display MTF, and possibly an eye MTF. If a perceptual image quality metric including the CSF or CTF is used to describe the quality of the system, the eye MTF is then neglected and not cascaded with the system MTF. Since CTF measurements are made through perceptual image testing, the eye is a necessary part of the measurement. Thus the CTF includes not only effects of perception (optical nerve transmission characteristics, mental interpretation, preferences, image processing performed by the brain, color channel effects, etc.), but also the transfer characteristics of the eye optics. Including the eye MTF in the cascaded system MTF, then applying the CSF or CTF in the metric would be a redundant inclusion of the eye MTF, over-weighting its effects. Since the MTF of the eye is already accounted for in the CSF and CTF, no further discussion of the eye MTF is necessary for this application.

2.6 Viewing Distance

Although viewing distance is considered important in perceptual testing since the CSF is dependent on the viewing angle and hence the viewing distance, the viewing angle is essentially fixed by the fovea. Since the observer is allowed to shift their attention around an image, the imaging is assumed to be always foveal in nature. Thus, although an image may subtend a much larger angle, the observer's attention is limited to a very small viewing angle. The viewing distance is then relatively constant for calculating a CSF. The viewing distance is very important for creating the link between retinal frequencies and image spatial frequencies.

2.7 Conversion of Retinal to Spatial Frequencies

Typically, image quality is discussed in terms of the system MTF at the image plane, a function of spatial frequency. For perceptual image quality, this is also true, but since the Contrast Sensitivity Function is commonly specified as a function of retinal frequencies in cyc/deg or cyc/rad, it is necessary to convert between retinal frequencies and spatial frequencies of an image. From spatial frequency of an observed image, spatial frequencies of any other plane (object plane, optical image plane, intermediate display planes, etc.) can be found from simple scaling of the frequencies using the appropriate magnifications.

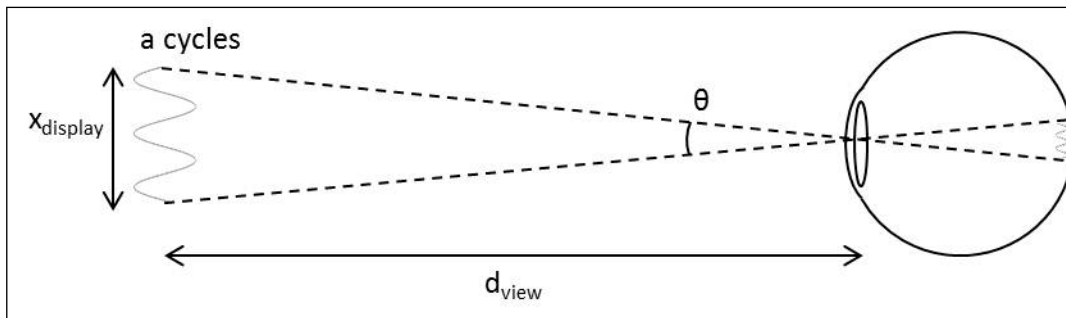


Figure 18. The geometry for converting between spatial frequencies in the observation plane and angular frequencies at the retina.

Figure 18 shows that a spatial frequency of a cycles spanning a lateral distance of $x_{display}$ subtends an angle θ when viewed at a distance of d_{view} . The spatial frequency in the display plane ($u_{display}$) is simply the number of cycles divided by the distance spanned by those cycles.

$$u_{display} = \frac{a \text{ cycles}}{x_{display}} \quad (2-3)$$

The angle θ in radians is given as the ratio of $x_{display}$ to the viewing distance.

$$\theta[rad] = \frac{x_{display}}{d_{view}} \quad (2-4)$$

The retinal frequency is given as the ratio of the number of cycles divided by the angular subtense of such.

$$u_{retina} = \frac{a \text{ cycles}}{\theta[rad]} = \frac{d_{view} a \text{ cycles}}{x_{display}} = d_{view} u_{display} [\text{cyc} / \text{rad}] \quad (2-5)$$

Simply converting radians to degrees yields the final scaling term to relate retinal frequencies to observation plane spatial frequencies.

$$u_{retina} = d_{view} u_{display} \left[\frac{\text{cyc}}{\text{rad}} \right] = d_{view} u_{display} \left[\frac{\text{cyc}}{\text{rad}} \right] \left[\frac{\pi \text{ rad}}{180 \text{ deg}} \right] = 0.01745 * d_{view} u_{display} \left[\frac{\text{cyc}}{\text{deg}} \right] \quad (2-6)$$

Thus, one obtains retinal frequencies by multiplying display spatial frequencies by the viewing distance and a constant conversion factor. This is true for any plane that is observed directly.

3.0 IMAGE QUALITY METRICS

This chapter contains three sections on image quality metrics. First, common image quality metrics such as wavefront aberrations and Strehl Ratio are presented with special attention given to why these are not suitable for application to this research. The Optical Transfer Function based image quality metrics are more robust than the common metrics, but few have matured to any reasonable level. However, these are the metrics of interest, and so, a section is dedicated to the historical development of OTF-based metrics. Finally, a section is included to discuss the benefits and shortcomings of using OTF-based metrics that are normalized to a diffraction limited value.

3.1 Common Image Quality Metrics

Of the common image quality criteria, wavefront errors and Strehl Ratio are frequently used as optical design criteria. Resolution targets have had wide applications, most frequently for measuring a maximum observable resolution. Fractional enclosed energy criteria such as fractional encircled, fractional ensquared, or fractional enslitted energy are most often used in optical specifications for systems with non-imaging applications. Though it is a reasonable system, Johnson's Criteria has been applied most frequently to military infrared applications. The General Image Quality Equation and the National Imagery Interpretability Rating Scale are two specialized evaluation systems used primarily for evaluating imagery for very particular tasks. The above criteria will be reviewed individually in an attempt to reveal their deficiencies in application to this research.

3.1.1 Peak-to-Valley Wavefront Error

Peak-to-valley wavefront error is a measure of the maximum wavefront error occurring in the exit pupil of an optical system. It is highly dependent on the obscuration ratio (ϵ) of the system and is NOT the same as the peak wavefront error. For a system with 1λ of defocus, the peak wavefront error is 1λ . The peak-to-valley wavefront error depends on the obscuration ratio. For $\epsilon=0$, the peak-to-valley wavefront error is simply the peak wavefront error of 1λ . For $\epsilon=0.5$, the peak-to-valley wavefront error is reduced to 0.75λ , and for larger obscurations, the peak-to-valley wavefront error will continue to decrease. Note that this is not the case for all aberrations.

Unfortunately, the peak-to-valley wavefront error is not a particularly useful measure of image quality. For 1λ of pure defocus and 1λ of pure spherical aberration in a system with a circular pupil ($\epsilon=0$), both have a peak-to-valley wavefront error of exactly 1λ . However, how much the wavefront differs from an ideal wavefront for each case is a difference of r^4 versus r^2 , leading to a noticeable difference in image quality.

Theoretical expressions for Peak-to-Valley wavefront errors are available from Mahajan [3]. It is worth noting that Peak-to-Peak Wavefront Error is synonymous with Peak-to-Valley Wavefront Error, but both differ from Absolute Peak Wavefront Error for the cases of balanced coma and balanced astigmatism. The expressions for the peak-to-valley wavefront error for an obscured aperture are summarized in Table 2.

Table 2. Peak-to-Valley wavefront expressions for annular apertures. The right-most column provides the simplified expressions for the case of a circular pupil.

Aberration	Peak-to-Valley Wavefront Error	Peak-to-Valley Wavefront Error for $\epsilon=0$
Defocus	$W_{020}(1-\epsilon^2)$	W_{020}
Spherical Aberration	$W_{040}(1-\epsilon^4)$	W_{040}
Balanced Spherical Aberration	$W_{040}\left(\frac{1-2\epsilon^2+\epsilon^4}{4}\right)$	$\frac{W_{040}}{4}$
Astigmatism	W_{222}	W_{222}
Balanced Astigmatism	W_{222}	W_{222}
Coma	$2W_{131}$	$2W_{131}$
Balanced Coma	$2W_{131}\left(1-\frac{2(1+\epsilon^2+\epsilon^4)}{3(1+\epsilon^2)}\right)$	$\frac{2W_{131}}{3}$

3.1.2 RMS Wavefront Error

The Root Mean Square (RMS) wavefront error is a measure of the phase difference between an aberrated wavefront and that of an ideal planar wavefront. The RMS wavefront error (σ_{RMS}) is related to the wavefront variance (σ^2) by (3-1).

$$\sigma_{RMS} = \sqrt{\sigma^2} \quad (3-1)$$

The wavefront variance is given by (3-2).

$$\sigma^2 = \langle W^2 \rangle - \langle W \rangle^2 = \left(\frac{1}{\pi} \int_0^1 \int_0^{2\pi} W^2(\rho, \theta) \rho d\rho d\theta \right) - \left[\frac{1}{\pi} \int_0^1 \int_0^{2\pi} W(\rho, \theta) \rho d\rho d\theta \right]^2 \quad (3-2)$$

Table 3 shows the results of solving Equation (3-2) for combinations of aberrations (astigmatism with defocus, spherical aberration with defocus, and coma with tilt). The appropriate amount of lower order aberrations needed to minimize the RMS wavefront error for each aberration present as well as the total minimum RMS wavefront for each “balanced” combination of aberrations are shown. The general expressions for RMS wavefront error are listed in Table 4.

Table 3. Combinations of aberrations to minimize RMS wavefront error along with the resulting minimum RMS wavefront error.

Aberration	Balancing aberration to minimize σ_{RMS}	Minimum σ_{RMS}
Spherical Aberration (W_{040})	$W_{020} = -(1 + \varepsilon^2)W_{040}$	$\frac{2\pi}{6\sqrt{5}}(1 - \varepsilon^2)^2 W_{040}$
Astigmatism (W_{222})	$W_{020} = -\frac{W_{222}}{2}$	$\frac{2\pi}{2\sqrt{6}}\sqrt{1 + \varepsilon^2 + \varepsilon^4} W_{222}$
Coma (W_{131})	$W_{111} = -\frac{2}{3} \frac{(1 + \varepsilon^2 + \varepsilon^4)}{(1 + \varepsilon^2)} W_{131}$	$\frac{2\pi(1 - \varepsilon^2)}{6\sqrt{2}} \sqrt{\frac{1 + 4\varepsilon^2 + \varepsilon^4}{1 + \varepsilon^2}} W_{131}$

Table 4. Theoretical RMS Wavefront Error expressions derived from Equation (3-2).

Aberration	RMS Wavefront Error
Defocus	$\frac{\pi W_{020}}{\sqrt{3}}(1-\varepsilon^2)$
Spherical Aberration	$\frac{2\pi W_{040}}{3\sqrt{5}}\sqrt{4-\varepsilon^2-6\varepsilon^4-\varepsilon^6+4\varepsilon^8}$
Balanced Spherical Aberration	$\frac{\pi W_{040}}{3\sqrt{5}}(1-\varepsilon^2)^2$
Astigmatism	$\frac{\pi W_{222}}{2}\sqrt{1+\varepsilon^2}$
Balanced Astigmatism	$\frac{\pi W_{222}}{\sqrt{6}}\sqrt{1+\varepsilon^2+\varepsilon^4}$
Coma	$\frac{\pi W_{131}}{\sqrt{2}}\sqrt{1+\varepsilon^2+\varepsilon^4+\varepsilon^6}$
Balanced Coma	$\frac{\pi W_{131}}{3\sqrt{2}}\frac{(1-\varepsilon^2)\sqrt{1+4\varepsilon^2+\varepsilon^4}}{\sqrt{1+\varepsilon^2}}$

Although the RMS wavefront error gives a good indication of how much the actual wavefront differs from an ideal planar wavefront, an equal amount of RMS wavefront error of a single balanced aberration may not have the same effect on image quality as a different single balanced aberration. In fact, for a 24" diameter telescope with an RMS wavefront error of 0.4λ and an obscuration ratio of 0.35, there will be 6.97λ of pure spherical aberration appropriately balanced with defocus (-7.82λ) or 1.84λ of pure astigmatism appropriately balanced with defocus (-0.92λ). The difference in image quality for these two is obvious (Figure 19).



*Original image used in simulations from <http://www.nasa.gov>

Figure 19. Two images degraded with equal RMS wavefront error (0.4λ) when the aberration is balanced spherical aberration (left) and balanced astigmatism (right).

3.1.3 Strehl Ratio

The Strehl Ratio is defined as the ratio of the central irradiance in an aberrated Point Spread Function to the central irradiance of the diffraction limited Point Spread Function [4].

Analytically, the Strehl Ratio (S) is given by:

$$S = \frac{1}{\pi^2(1-\varepsilon^2)} \left| \int_{\varepsilon}^1 \int_0^{2\pi} e^{i\Phi(\rho,\theta)} \rho d\rho d\theta \right|^2 \quad (3-3)$$

where ε is the obscuration ratio of the exit pupil, ρ and θ are the polar coordinates of the exit pupil, and $\Phi(\rho,\theta)$ is the phase aberration across the exit pupil [3].

The Strehl Ratio is frequently applied to systems with pure aberrations as well as with aberrations which have been balanced with lower order aberrations to minimize the RMS wavefront error. Because of the frequency of use, solutions have been derived for the Strehl Ratio for balanced (Table 5) and pure (Table 6) aberrations [3].

It is important to note that several of the solutions are not closed form solutions and require numerical methods to obtain a solution. For a system in the presence of mixed aberrations, the Strehl Ratio can be found by applying the Equation (3-3) for Strehl Ratio.

Table 5. Theoretical expressions for the Strehl Ratio of balanced aberrations.

Aberration	Theoretical Strehl Ratio
Balanced Spherical Aberration	$\frac{1}{4W_{040}(1-\varepsilon^2)^2} \left[C^2 \left((1-\varepsilon^2)\sqrt{4W_{040}} \right) + S^2 \left((1-\varepsilon^2)\sqrt{4W_{040}} \right) \right]$
Balanced Astigmatism	$\left[\frac{2}{\pi W_{040}(1-\varepsilon^2)} \sum_{k=0}^{\infty} J_{2k+1}(\pi W_{040}) - J_{2k+1}(\varepsilon^2 \pi W_{040}) \right]^2$
Balanced Coma	$\frac{1}{(1-\varepsilon^2)^2} \left \int_{\varepsilon^2}^1 J_0(2\pi x^{3/2}) dx \right ^2$
W=Aberration Coefficient in waves ε =obscuration ratio $C(\alpha) = \int_0^\alpha \cos\left(\frac{\pi x^2}{2}\right) dx \quad S(\alpha) = \int_0^\alpha \sin\left(\frac{\pi x^2}{2}\right) dx \quad H(\alpha) = \sqrt{J_0^2(\alpha) + J_1^2(\alpha)} \quad \alpha(\alpha) = \tan^{-1}\left(\frac{J_1(\alpha)}{J_0(\alpha)}\right)$	

Table 6. Theoretical expressions for Strehl Ratio of pure aberrations.

Aberration	Theoretical Strehl Ratio
Spherical Aberration	$\frac{1}{4W_{040}(1-\varepsilon^2)^2} \left[\left\{ C(\sqrt{4W_{040}}) - C(\varepsilon^2 \sqrt{4W_{040}}) \right\}^2 + \left\{ S(\sqrt{4W_{040}}) - S(\varepsilon^2 \sqrt{4W_{040}}) \right\}^2 \right]$
Astigmatism	$\frac{1}{(1-\varepsilon^2)^2} \left\{ H^2(\pi W_{040}) + \varepsilon^2 H^2(\varepsilon^2 \pi W_{040}) - 2\varepsilon^2 H(\pi W_{040})H(\varepsilon^2 \pi W_{040}) \times \right. \\ \left. \cos[\pi(1-\varepsilon^2)W_{040} - \alpha(\pi W_{040}) + \alpha(\varepsilon^2 \pi W_{040})] \right\}$
Coma	$\frac{1}{(1-\varepsilon^2)^2} \left \int_{\varepsilon^2}^1 J_0 \left(2\pi x^{3/2} - \frac{2(1+\varepsilon^2+\varepsilon^4)}{3(1+\varepsilon^2)} x^{1/2} \right) dx \right ^2$
<p>W=Aberration Coefficient in waves ε=obscuration ratio</p> $C(\alpha) = \int_0^\alpha \cos\left(\frac{\pi x^2}{2}\right) dx \quad S(\alpha) = \int_0^\alpha \sin\left(\frac{\pi x^2}{2}\right) dx \quad H(\alpha) = \sqrt{J_0^2(\alpha) + J_1^2(\alpha)} \quad \alpha(\alpha) = \tan^{-1}\left(\frac{J_1(\alpha)}{J_0(\alpha)}\right)$	

It has been reported that only for very high values of Strehl Ratio do Strehl Ratio and minimum RMS wavefront error correspond [3]. For the case of large enough aberrations to significantly reduce the Strehl Ratio, balancing the aberrations such that the RMS wavefront error is minimized will not only fail to maximize the Strehl Ratio, but may in fact reduce it [3].

The advantage of the Strehl Ratio is its wide acceptance by the optical community and the associated understanding of it. Its usefulness is hindered by the inability to modify it to account for the human visual system and perception.

3.1.4 Fractional Enclosed Energy

Fractional enclosed energy is an important image quality criterion for systems with digital detectors, and is frequently used as a top level image quality requirement for systems design. The encircled energy provides a measure of the fraction of the Point Spread Function's (PSF's) energy contained within a given radius. For a given radius, the fractional encircled energy of the PSF irradiance ($I(r,\theta)$) is given by :

$$P(r_c) = \int_0^{r_c} I(r,\theta) r dr d\theta \quad (3-4)$$

By performing this integral for values of r_c of interest, a plot can be generated which necessarily begins at $P(0)=0$, and asymptotically reaches $P(\infty)=1$. Since the PSF of a system is highly dependent on the obscuration ratio ϵ , the fractional encircled energy is then highly dependent on ϵ as well.

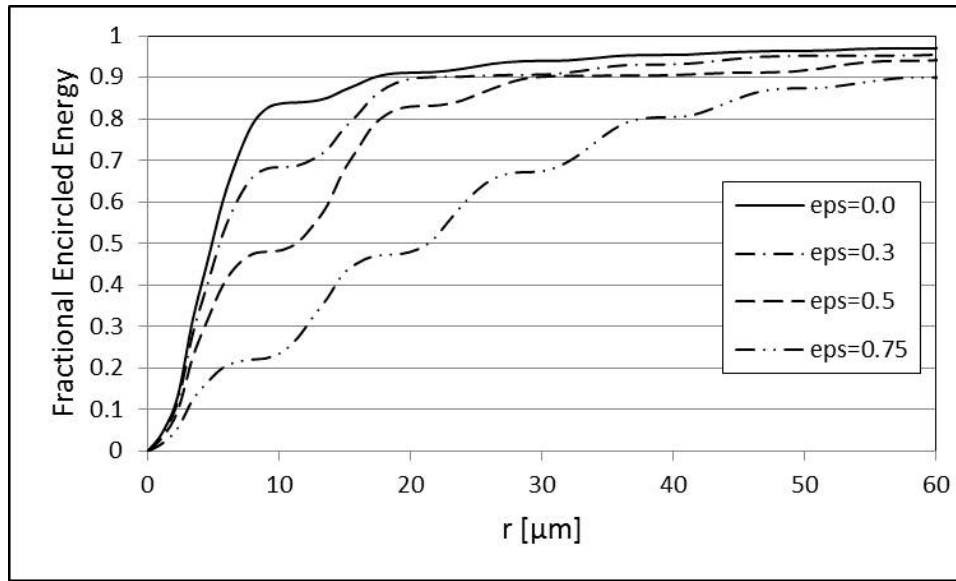


Figure 20. Diffraction-limited fractional encircled energy for several obscuration ratios.

The information required for calculating the fractional encircled energy is a high resolution image of the PSF, or more practically, measurements of the aberrations present in the system, such as would be obtained through interferometry. With this information, the PSF could be digitally generated and the integration defined in Equation (3-4) can be performed numerically. Numerical methods are most likely to be needed since only irradiance distributions for defocus, tilt, and spherical aberration exist in closed form solution.

Numerically calculated encircled energies are plotted for several values of defocus (Figure 21), several values of spherical aberration balanced with defocus to minimize RMS wavefront error (Figure 22), and several different aberrations balanced appropriately to minimize RMS wavefront error (Figure 23).

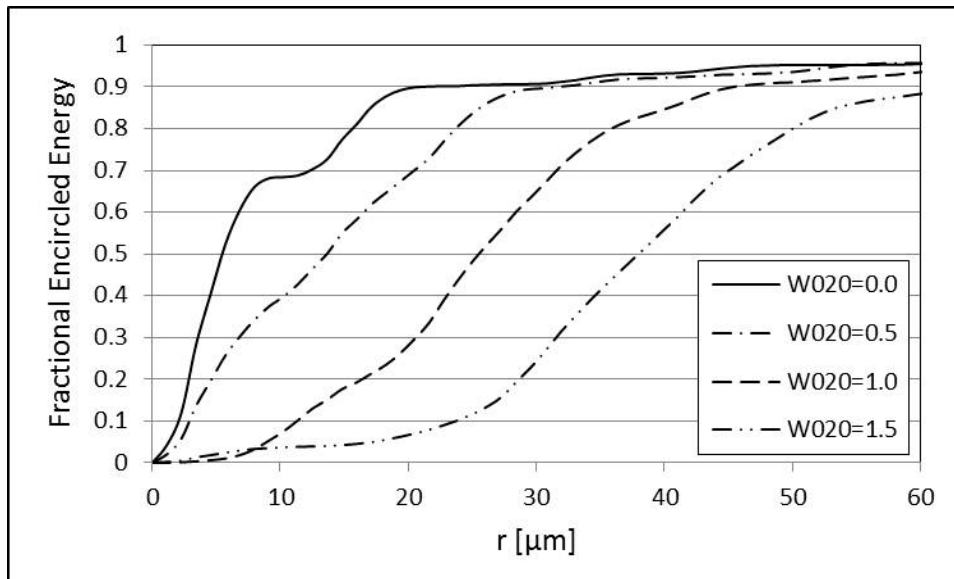


Figure 21. Fractional encircled energies for an obscuration ratio of 0.3 with of 0λ , 0.5λ , 1.0λ , 1.5λ , and 2.0λ of defocus.

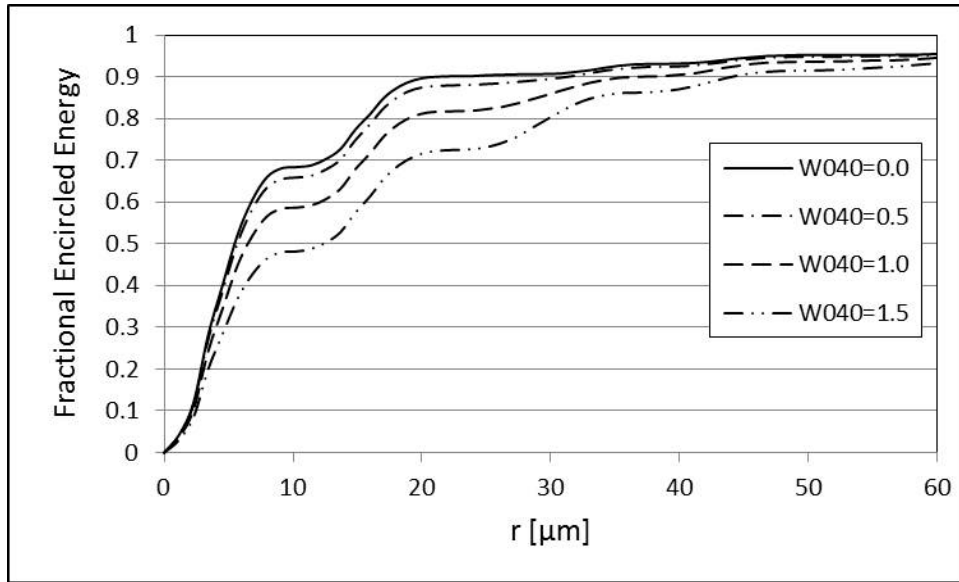


Figure 22. Fractional encircled energies for an obscuration ratio of 0.3 with 0.0λ , 0.5λ , 1.0λ , and 1.5λ , of spherical aberration, each balanced with defocus to minimize RMS wavefront error.

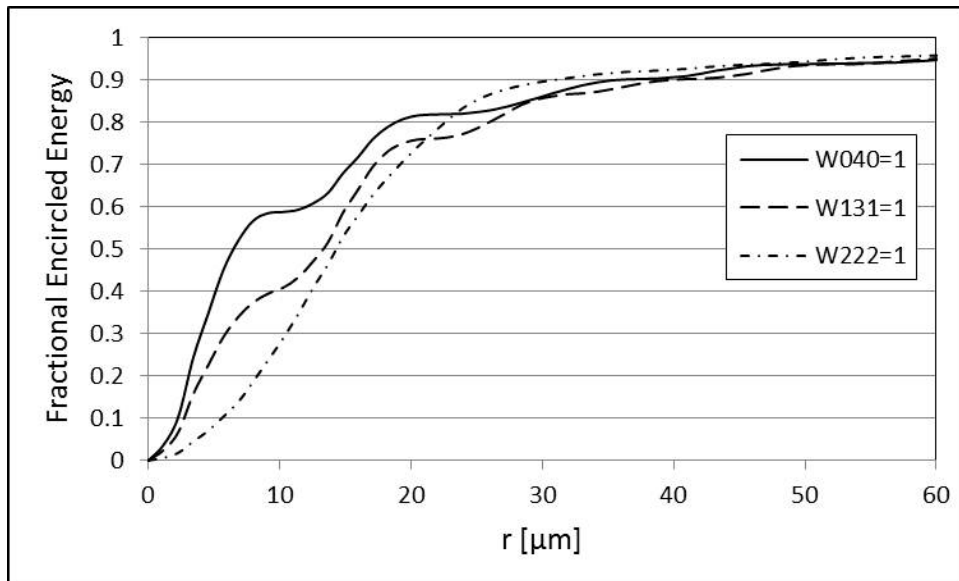


Figure 23. Fractional encircled energies for an obscuration ratio of 0.3 and 1λ each of spherical aberration, coma and astigmatism, each balanced appropriately to minimize RMS wavefront error.

The importance of this criterion can be seen by looking at detector arrays. For arrays of smaller detector pixels, image quality improves if the PSF is completely or nearly contained within a detector pixel. So, for a given detector array with fixed pixel dimensions, it is desirable to design an optical system which has a PSF that fits within that pixel. However, making the PSF significantly smaller than the pixel size wastes money in designing and fabricating a system whose image quality will not improve past that obtained with PSF size slightly smaller than the pixel dimensions.

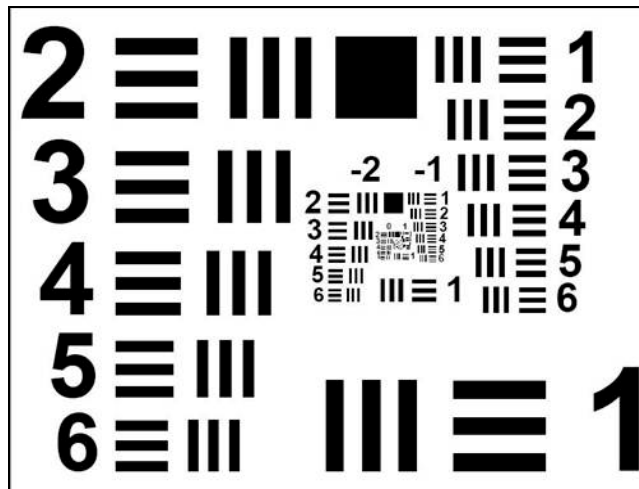
A better measure of image quality for use with digital detectors is fractional ensquared energy which is again a measure of the total integrated energy of the PSF, but this time, instead of being contained by a circle of radius r , it is enclosed in a square or rectangle of given dimensions. This allows a direct measure of the percentage of power in the PSF that could actually be contained within a single detector pixel. The general trends of fractional Ensquared energy follow those of fractional encircled energy.

Although widely used and of great use for systems with detector arrays, the enclosed energy does not provide direct image quality information. The Weber-Fechner Law states that the human visual system is most dependent on contrast, not on absolute illumination. Enclosed energy does not provide information on contrast and so, does not predict perceived image quality.

3.1.5 1951 Tri-bar Resolution Target Test

The 1951 3-bar resolution target (Figure 24) consists of a series of bars of graduated size (generally, the relative size between successive bar groups is the sixth root of 2) with each size group consisting of a set of three black bars separated by two white bars, one set oriented in the vertical direction, and one set oriented horizontally. This allows an effective measurement to be made regarding the finest resolvable object size for an imaging system, assuming a minimum contrast has been selected to define “resolvable”.

Unfortunately, when the test is applied, if a sub-standard telescope quality is discovered, no information about the aberration types and quantities is available from the test to aid in the maintenance process. Using a resolution target only provides pass/fail information.



*Reproduced from <http://wikipedia.org>

Figure 24. 1951 Tri-Bar Resolution Target

A second drawback of the bar target is the orientation of information. All of the bars are oriented in either the horizontal or vertical direction. Since the human visual system is more

sensitive to contrast along the horizontal or vertical directions than along a diagonal [5], much information about the image quality obtainable from the optical system under test is absent. The only way to fix this with the bar resolution target is to rotate the target and repeat the measurement for every desired orientation.

Further problems with the bar target are encountered when the optical system under test exhibits astigmatism. The minimum resolvable size for the system could be defined as the smallest bar group that has a minimum contrast (0.3 for instance) for both orientations, or the smallest bar group that has the minimum contrast (only one orientation must meet the contrast requirement). This is a significant issue for astigmatism where a line focus for either the vertical (Figure 25 left) or horizontal (Figure 25 right) could be chosen, providing good image quality for bars oriented parallel to the line focus but poor image quality for bars oriented perpendicular to the line focus. Instead of using a line focus, the medial focus (Figure 25 center) could be used so that the minimum contrast is reached for both orientations of bars for a single bar size.

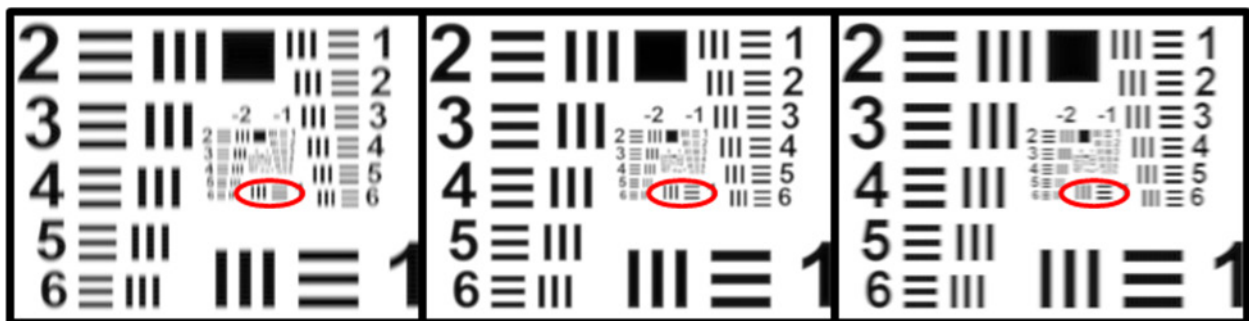


Figure 25. Three bar target simulations for a DOAMS telescope with 1.5λ of astigmatism at the vertical focus (left), medial focus (center) and horizontal focus (right). The circled regions provide a good reference to compare. The image with the vertical focus (left) has the best vertical bar resolution. Likewise, the image with the horizontal focus (right) has the best horizontal bar resolution. The medial focus provides the best compromise for normal imaging applications.

The three bar resolution target may be used to create an MTF plot if the contrast (modulation) is measured for each bar group. The MTF could then be constructed for the spatial frequencies corresponding to those of the bar groups, but only the principal directions of the MTF would be available unless the target is rotated and the measurements repeated for each new orientation.

It has been shown by Charman and Olin that results of tri-bar target tests are so unreliable that individual observers were unable to remain consistent with their own measurements of resolving power (or resolution) within a span of a couple of days [6].

3.1.6 National Imagery Interpretability Rating Scale

The National Image Interpretability Rating Scale (NIIRS) is a previously classified method of rating images on their ability to provide useful information to experienced observers. Originally intended for military applications, particularly for satellite imagery, it has also been updated in 1997 [7] to include interpretability rating definitions for civil applications.

The NIIRS system (and its closely related unclassified version released in 1978 called IIRS—Imagery Interpretability Rating Scale) focuses on the ability of observers to perform particular tasks with an image. Image interpretability is ranked on a 0-9 scale with 0 corresponding to poor imagery, and 9 corresponding to the ability to perform the most stringent of the NIIRS tasks. The

tasks, a subset of those found in the Johnson's Criteria, are detection and identification of smaller and smaller objects as the ranking increases.

The NIIRS scale was constructed using a multi-step process, heavily dependent on subjective quality assessments made by a particular chosen group of expert observers. The expert group was asked to sort a set of images along a rating scale with only two marked points—0 and 100. After this was completed, images representative of the quality at points 0, 25, 50, 75, and 100 were selected and placed on the scale. The ten criteria chosen were then sorted relative to these five points on the scale so that a number on the scale corresponds to each criteria.

The actual NIIRS scale was then constructed using several requirements:

- Linearity—a unit change of scale value anywhere on the scale should have the same perceived image quality change as a unit change of scale at any other scale location.
- Separability—a one unit change in the NIIRS quality of images provides a clear difference in perceived image quality.
- System Independence—the results of scale development can be applied to rate imagery obtained from any imaging system.
- Usability—consistent easy use of the scale by observers is necessary.

- Criteria Set Equivalence—any two images of the same quality should be ranked equally by the NIIRS scale regardless of the content of the image (i.e. open fields or military installations).

The NIIRS ratings provide a list of tasks, at least one of which must be able to be performed for imagery to obtain a given rating. Table 7 is a sample task from each list of the rating levels from the October 1995 Civil National Imagery Interpretability Rating Scale [8].

Table 7. Selected portions illustrating the type of task required to achieve a rating level for the October 1995 Civil National Imagery Interpretability Rating Scale [8].

Rating	Sample Required Task
0	Interpretability of the imagery is precluded by obscurity, degradation, or very poor resolution.
1	Detect a medium-sized port facility and/or distinguish between taxi-ways and runways at a large airfield.
2	Detect large buildings (e.g., hospitals, factories).
3	Detect trains or strings of standard rolling stock on railroad.
4	Identify individual tracks, rail pairs, control towers, switching points in rail yards.
5	Identify individual rail cars by type and/or locomotives by type.
6	Identify automobiles as sedans or station wagons.
7	Identify individual railroad ties.
8	Identify windshield wipers on a vehicle.
9	Detect individual spikes in railroad ties.

It is important to note that to obtain a NIIRS rating, imagery must provide the information necessary for that rating level as well as provide the information necessary for ALL lower rating levels.

3.1.7 Johnson's Criteria

Closely related to 3-bar resolution targets is Johnson's Criteria, whereby the resolvable bars of a bar target are related to such optical tasks as detection, orientation, recognition, and identification [2]. It is considered adequate for detecting the presence of an object to have a minimum contrast (set at some constant level) for one bar pair (one black and one white) across the minimum dimension of the object observed. Orientation information is obtainable if there are 1.4 bar pairs across the minimum dimension of the object. Recognition requires 4 bar pairs and identification requires 6.4 bar pairs, again, across the minimum dimension of the object.

Johnson's Criteria is helpful in cases where object characteristics are known and allow discernment between items within the class (i.e. cockpit shapes are known, allowing discernment between different aircraft). A common task in launch vehicle imaging is to observe any debris falling from the vehicle during ascent. Debris can be of any size and shape and fails to lend itself well to application of Johnson's Criteria.

Johnson's Criteria assumes that perceived image quality and the limiting resolution of an optical system are well correlated, a relation demonstrated to be unreliable [9].

3.1.8 General Image Quality Equation

In 1994, the original General Image Quality Equation (GIQE) was released, used to provide NIIRS with a predictive capacity. In 1997, the GIQE was updated to improve accuracy [10], and it is this version of the GIQE that will be discussed.

The development of the GIQE was primarily through regression analysis, converting the GIQE values to the ten levels of NIIRS. GIQE depends on several parameters—the relative edge response (RER), the ground-sampled distance (GSD), the gain from edge sharpening (G), overshoot from edge sharpening (H), and the signal to noise ratio (SNR). Considering these parameters, it becomes immediately evident that the GIQE includes digital image processing performed by cameras, particularly changes due to sharpening.

The GIQE is then given (in a slightly simplified form) by:.

$$NIIRS = 10.25 - a \log(GSD) + b \log(RER) - 0.656 H - 0.344 \frac{G}{SNR} \quad (3-5)$$

Note that the GSD, RER, and H parameters are geometric means. Also, a and b are constants whose values are respectively 3.32 and 1.559 if $RER \geq 0.9$, or 3.16 and 2.817 if $RER < 0.9$.

The results of the regression show an adjusted coefficient of determination of 0.986, indicating very good modeling results. The quoted results were for hard-copy tests, and the author states that testing experience shows equal or better performance for soft-copy tests.

The author indicates that the validity of this model is in question when the following condition is not met:

$$\frac{\lambda * F\#}{\text{pixel pitch}} \leq 1 \quad (3-6)$$

For the launch vehicle imaging telescopes, it is likely that this condition will never be met. The applicability of the GIQE to the TIME Tool is then unlikely.

3.2 Historical development of OTF-based metrics

The work of Otto Schade, beginning in 1948, began a new era of optical performance testing and prediction. Although a fair amount of his work was originally directed toward television and motion picture technologies with less abundant applications in photographic technology, he derived the Optical Transfer Function (OTF) and its applications to resolution and image sharpness. Since then, the OTF has gained general acceptance as being paramount in the measurement and performance characterization of optical imaging systems.

Schade provides a good review of the characteristics of human vision and perception, and discusses sources of lowered quality including graininess, flicker, and brightness errors [11]. He further considers the camera response, including lens and aperture effects, and also considers television camera tube response [12, 13]. The entire electro-optical system is then considered as a single imaging device and is analyzed and comparisons are made to perceptual results [14]. Perceptual data is compared with theoretical “subjective sharpness” curves derived by Schade which considers the human visual system through “aperture theory”. Schade further claimed that resolution, detail contrast, and image sharpness can be well characterized with such theory.

In 1951, Schade published the first part of another four part series, this one to characterize televisions in terms of electro-optics. The first part discusses image quality and size, image structure, sampling and overall transfer characteristics for the entire motion picture process. [15] In parts 2 and 3, Schade characterizes graininess and quality for motion pictures [16] and

television [17], using “sine-wave response” and his equivalent passband theory. After presenting the theory he provides experimental results as validation [17]. The series is concluded with the application of linear systems theory and Fourier transforms of apertures.[18]

Schade’s equivalent passband (N_e) of the optical system, was originally introduced in journals [15-19] but is still discussed in several textbooks [2, 20, 21]. By squaring the MTF, an expression for energy transmitted by an optical system at each spatial frequency is obtained. By integrating the square of the MTF, the total energy transferred is obtained. Now reshaping the squared MTF such that only two squared modulation values exist (unity and zero), there exists a unique spatial frequency such that the areas of the actual squared MTF and the reshaped MTF are equal (Figure 26). The spatial frequency for which this condition is satisfied, is the equivalent passband, stated mathematically in Equation (3-7).

$$N_e = \int_{-\infty}^{\infty} MTF^2 df \quad (3-7)$$

The usefulness of the equivalent passband is restricted to monotonically decreasing MTFs (a rare case for LVIT) and for comparing similar systems[2].

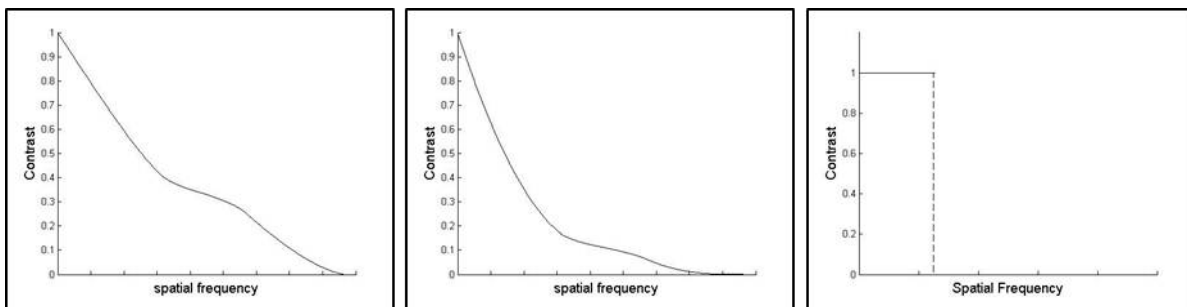


Figure 26. Measured MTF (Left), MTF^2 (Center), and idealized MTF^2 (Right) with the same area as that of the measured MTF^2 .

In 1958, with the aid of Higgins and Wolfe, Lamberts published original work on what was being called the “sine wave response” [22] which, along with the frequency response and contrast transfer, would later be relabeled the modulation transfer function by the International Commission for Optics [23]. A second publication in 1958, was a continuation of the same “MTF” work and considered line spread functions [24]. Further work was done by Lamberts in extending MTF theory to practical applications in photographic emulsions [25], photographic printing [26], and to image-forming systems [27].

1964 saw the empirical System Modulation Transfer Acutance (SMTA) developed by Crane [9]. He admits that the approach to image quality prediction based on MTF data is more empirical than theoretical. However, he also claims that subjective testing confirms that it is a good measure. The SMTA is a logarithm of a summation over all components in the imaging-observing chain. The terms within the summation are the square of 200 times the magnification, divided by the Modulation Transfer Function Area (MTFA) for the given component. This measure then accounts for the human observer through the magnification, modulation transfer, and contrast threshold of the eye. Edward Crane’s System Modulation Transfer Acutance (SMTA) was developed empirically to predict perceived image “sharpness” or “crispness” [9]. It is important to make the distinction between sharpness and overall image quality, sharpness being a single attribute within image quality. The SMTA was designed to account for all components of the system, including development, image transfer, printing, and human observation. Image vibration could also be included. The general SMTA formula is defined mathematically by Equation (3-8).

$$SMTA = 120 - 25 \log \left(\sum_{\text{all components}} \left(\frac{200 * m}{MTFA} \right)^2 \right) \quad (3-8)$$

In Equation (3-8), m is the magnification of the component being considered, defined as the ratio of the image width in the retina to the image width in the previous component of the system, the constant 25 was chosen so that one SMT Acutance unit corresponds exactly to one Just Noticeable Difference (JND), and the MTFA is in units of mm^{-1} . The constants of 120 and 200 were chosen empirically to shift the SMTA scale such that a value corresponded to the perceptual sharpness qualities listed in Table 8. Even with the shift, the SMTA can allow values greater than 100.

Table 8. SMT Acutance value correlates.

SMT Acutance Value	Qualitative Sharpness
>99	Excellent
>90	Good
>80	Fair
>70	Passing

The SMTA was developed as an empirical formula and has little theoretical foundation. The first concerns arise in the MTFA values. The published material does not specify if a modulation threshold should be accounted for, and considering the units the MTFA is assumed to be in, it MUST assume a uni-dimensional or angle-averaged MTF. This ignores information about human thresholds and the anisotropic characteristics of the eye.

The origins of applying the MTF as an image quality measure grounded in theory can be traced back to 1965 with the work of Charman and Olin [6]. The MTF was not initially known as such -- rather, it was known by the name "Threshold Quality Factor" (TQF). The TQF integrated the difference between $0.2 \times \text{MTF}$ and the threshold rather than simply the MTF minus the threshold. This was based on assumptions of image content for aerial imagery. Closely related to the MTF, and quite possibly its predecessor (the first publication of the MTF was in 1970 but non-located, unpublished references were made to earlier work on or similar to the MTF), the threshold Quality Factor (TQF) was developed for rating aerial reconnaissance imagery for usefulness to photo-interpreters. Although this is a very closely related application to that of the TIME Tool, it is important to note that the TQF was developed specifically for reconnaissance imagery and assumptions about typical images was made in the TQF development. For instance, it was recognized that most aerial images consisted of low contrast scenes with a fairly short range of luminance across the images. Based on this information and the fact that resolution targets used at the time for rating such imagery had a log luminance difference of 0.20 between bright and dark bars (or other objects depending on the particular target in use), the log luminance was converted to a modulation of 0.23, which was rounded to 0.20 and used as an average object modulation.

The TQF thus assumes uniform object modulation of 0.20 and is then not applicable to the optical imagery produced by the launch vehicle imaging telescopes for range applications (except on days with very poor atmospheric effects and thus very low contrast). Mathematically,

the TQF is found by integrating the “object” information transferred to the image by the imaging system ($0.20 \times \text{MTF}$) minus the modulation threshold, labeled here as CTF (Equation (3-9)).

$$TQF = \int_0^{f_{cutoff}} 0.20 * MTF - CTF \, df \quad (3-9)$$

TQF values are then a measure of the object information (having a constant modulation of 0.20 at all frequencies), transferred to the image plane, with a subtracted sub-threshold term to account for human, film, or detector threshold effects.

The TQF was later modified to not assume an object modulation, therefore generalizing the quality measure, and becoming known as the MTFA. Based on notation, it is assumed that a one-dimensional MTF was used in experimental work, but the equation could easily be extended to two dimensions.

The experimental validation provided by Charmin and Olin consisted of only four expert observers who took several measurements of the resolving power of a system (using resolution targets) and averaging them. These results were considered to be the subjective test results and a linear relation between resolving power and TQF are demonstrated. The author also states that for most aerial camera systems, resolving power tests had good correlation with “an observer’s impression of the detail content of photographs produced by the systems” [6]. This has been demonstrated by others to be unreliable at best [9], leading one to question the validity of the TQF image quality metric.

In 1970, Snyder presented the usefulness of the MTFA, [28] quoting work performed by Brainard and Borough (a frequently quoted unpublished work). The work presented by Snyder was to relate the interpretability (or usefulness) of aerial reconnaissance imagery to the MTFA value. His conclusion is that it is unclear what measure of image quality should be used universally for all imaging systems, but for typical photographic imaging, the MTFA is a valid measure. However, the method of subjective ranking was complex, involving rank-ordering of nine images and answering eight multiple choice questions regarding information present in the images. The Modulation Transfer Function Area (MTFA) reported on by Harry Snyder [28] and commonly discussed in textbooks, [20] is a fairly simple image quality metric. Introduced in one dimensional form, it is the area between the one-dimensional MTF or angle averaged MTF and the contrast threshold function (Figure 27). The threshold function used will depend on SNR, glare, vibration, and eye adaptation level.

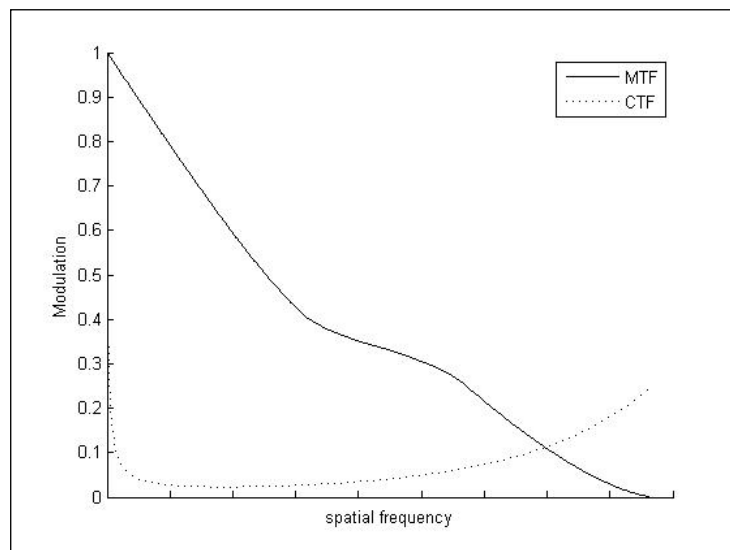


Figure 27. An MTF curve (solid curve) and contrast threshold function (dotted curve). The MTFA would then be the total integrated area between the two curves up to the point of intersection.

By extending the MTFA to the two dimensional MTF, this would yield a volume under the MTF and will be denoted MTFV (Modulation Transfer Function Volume).

The results quoted by Snyder were for a one dimensional application and the correlation coefficients reported for 36 trained photo interpreters were between 0.93 and 0.97. Three attributes were varied in the image generation, namely grain noise, contrast, and the MTF. The reported correlation coefficients are quite good, but it is important to note the MTF variation that was actually used. Of the four MTF curves used, all appeared to be diffraction-limited systems with varying $F^\#$. The MTF essentially only varies in $F^\#$ and ignores aberrations which have a very different role in perceptual image quality. The results of Snyder's testing was then in demonstrating that the MTFA for a diffraction-limited optical system is well correlated to perceptual image quality and image interpretability.

The MTFA and MTFV can be considered to be measures of the total image resolution capability of an optical system for all spatial frequencies and at all orientations. The human visual system is accounted for in cascading the MTF curves for all components, as well as in inclusion of the contrast threshold for the human eye.

Since the MTF and PSF are Fourier transform pairs, the Central Limit Theorem can be applied [29]. If the contrast threshold function is neglected and the normalized MTF is used, the MTFA degenerates to exactly the Strehl Ratio as seen in Equation (3-10).

$$\mathfrak{Z}(PSF) = OTF \Rightarrow \text{/Central Limit Theorem/} \Rightarrow \int_{-\infty}^{\infty} OTF = PSF(0)$$

$$\frac{\int_{-\infty}^{\infty} OTF_{\text{aberrated}}}{\int_{-\infty}^{\infty} OTF_{\text{diff.-lim}}} = \frac{PSF_{\text{aberrated}}(0)}{PSF_{\text{diff.-lim}}(0)} = \text{Strehl Ratio} \quad (3-10)$$

Granger and Cupery attempted improvement over the MTFA in 1971 with the MTF-based Subjective Quality Factor (SQF), [30] by taking a logarithmic integral of the MTF over the range of 10 cycles/degree to 40 cycles/degree. They obtained excellent correlation between the SQF and an existing print standard known as the Image Sharpness Scale [31] (a scale made of ordered images separated noticeably by defocus) which they demonstrate is linear in Just Noticeable Differences (JND)s. The Subjective Quality Factor (SQF) developed by Granger and Cupery [30] was an effort to predict perceived image quality of realizable optical system conditions. The SQF is defined mathematically in Equation (3-11).

$$SQF = \int_{10}^{40} \int_0^{2\pi} MTF(f, \theta) d\theta d \log(f) \quad (3-11)$$

In Equation (3-11), $MTF(f, \theta)$ is the two dimensional MTF of the system, and the frequency limits of integration are given in lines/mm at the retina.

The SQF makes several assumptions which ultimately limit its accuracy:

1. Weber's Law, which is logarithmic in nature, suggests that the OTF should be logarithmically weighted in spatial frequency.

2. The Human Visual System can be assumed to have a rectangular bandpass between 10 and 40 lines per millimeter at the retina.
3. Perceived image quality results from an equal weight angular average of image information.

The first assumption is based on the statement of Weber's Law, which, as applied to image evaluations, can be restated as a just noticeable difference occurs with a constant percentage change in attribute. Thus, for larger attributes, the constant percentage change requires more absolute change than at lower attribute levels. The assumption then does not account for such perceptual effects as preference of contrast to sharpness, or one image quality attribute to another. Neither does Weber's Law make any statement about the preference of certain spatial frequencies.

The second assumption is known to be invalid but the bandpass shape was chosen to simplify calculations. The limits of integration are chosen based on the peak of the Human Visual System (HVS) MTF occurring in the range of 10-20 lines/mm. How the exact limits of integration were chosen is unclear.

The final assumption listed is based on the performance of previous OTF-based image quality measures which relied on angle averaged OTFs. The assumption was tested by Granger and Cupery for the case of astigmatism (both large and small amounts of astigmatism), and their

results supported the assumption. With the conditions and qualities tested, it may well be a reasonable assumption.

Testing of the SQF was done using black and white images, a series of a single image, presented to approximately 30 observers. Some tests used the paired image comparison method, while others used rank order tests.

In 1973, Donofrio suggested integrating under a modified MTF for color Cathode Ray Tubes [32]. The MTF was measured by taking a line spread of the luminance of the display. This luminance MTF profile was converted to brightness since the human eye responds to brightness and not luminance. The modified MTF was then multiplied by the eye MTF to account for the frequency response of the HVS, and the final result was integrated and labeled as the Image Sharpness Value (ISV). Comparison was made to the subjective ability of viewers to observe raster lines. The results were then highly dependent on cathode current. The approach has not been applied to static images. Furthermore, Donofrio concludes that MTF is a good measure of image sharpness only if perception is not to be considered. Instead, he suggests using the ISV for CRT applications or the SQF method for photographs. Donofrio developed the Image Sharpness Value (ISV) as an analog to the SQF of Granger and Cupery. The SQF was developed for use with photographic image quality whereas the ISV was developed specifically for rating cathode ray tubes (CRTs). The ISV like the SMTA however, was developed to rate the perceived sharpness of an image, not the overall perceived quality of an image.

Donofrio recognized the importance of taking into account that the HVS perceives brightness rather than luminance. He therefore measured CRT line profile luminance and converted it to a brightness distribution using the relation shown in Equation (3-12), where B is then the relative brightness percentage and L is the relative luminance percentage.

$$B = 12.9 L^{0.44} \quad (3-12)$$

The author claims that the relationship holds for the light levels found in most displays.

After converting the line profile to brightness, the brightness profile is used to generate the MTF, which is then multiplied by the MTF of the eye. The ISV is then the area under the MTF product as shown in Equation (3-13), and is shown by the author to correlate well to expert and average viewer perception.

$$ISV = \int_0^{f_{cutoff}} MTF_{Brightness} * MTF_{eye} df \quad (3-13)$$

The perceptual testing tasks performed by viewers were to attempt identification of individual raster lines in bright image regions and observation of evidence of details in shadow regions with low CRT current. The number of viewers used is not provided.

The ISV is then a very application specific measure of image sharpness and not of image quality. Furthermore, evidence of the correlation of ISV values with image sharpness perception may not be good since the number of observers is not disclosed, and the potential exists for extreme bias

in rankings. For example, if the only expert observers used prepared the test images and had a priori knowledge of the detail they were looking for in shadow regions, the perceived sharpness in this area may differ from unbiased observers who are unaware of the image content.

The final concern of the ISV's applicability and accuracy is that it uses a uni-dimensional MTF, not accounting for the anisotropy of the eye, and may only consider sharpness in one direction (details of the line profile and any directional averaging are not included in the publication).

Also in 1973, a collection of perceptual image quality works was published [33]. Within this book, the MTF concept and application are reviewed, particularly the work performed by Snyder.

In 1974, a rating scale was developed by the Imagery Resolution Assessment and Reporting Standards Committee of the US Government to better classify image quality in terms of the ability to perform particular tasks with surveillance imagery [8]. The scale became known as the National Imagery Interpretability Rating Scale (NIIRS) which remained classified until 1991. A modified version of the NIIRS for civil use (Civil NIIRS) was released to the public in 1996 [7]. Further adaptations using the same methodology were made specifically for visible, radar, and multispectral applications.

To further the MTF-based optical system characterizations, the Polychromatic MTF (PMTF) was introduced in 1982 [34]. By taking the PMTF, multiplying it by the transfer function of the eye,

then integrating the result with a linear weighting function, the result was found to correlate well to subjective quality assessments for several amounts of aberration.

Until 1983, two-dimensional MTF data was not generally available, a result of testing techniques, detector limitations, and data storage limitations. As a result, one dimensional MTF cross-sections were used until 1983, when computers were applied to take two-dimensional Fourier transforms of the point spread functions (PSF)s of systems, yielding the two-dimensional MTF [35]. In 1985, this work was extended to the PMTF and guidelines were presented for commercial photographic systems [36]. A method of assessing on- axis and off- axis image quality samples was provided simultaneously. The two-dimensional MTF work was extended in 1985 to provide a method of estimating the volume under the MTF using two one dimensional orthogonal MTF measurements [37]. This allows reduced measurements and increased image quality measurement accuracy.

Barten improved on the method of Carlson and Cohen in 1990 by introducing the Square Root Integral (SQRI) [38]. The HVS is accounted for with the modulation threshold function of the eye and a logarithmic integration over the entire frequency range of 0 to the intersection of the MTF with the modulation threshold function of the eye. The units of this integral are then JNDs and evidence is given of very good consistency with subjective testing. The Square Root Integral (SQRI)[38] is again a method of integrating some function involving the MTF and the eye modulation threshold function (or contrast threshold function). In this case, it is the logarithmic integral of the ratio of MTF to modulation threshold as shown in Equation (3-14).

$$SQRI = \frac{1}{\ln(2)} \int_0^{f_{\max}} \sqrt{\frac{MTF}{CTF}} \frac{df}{f} \quad (3-14)$$

The square root form within the integral is an attempt to account for the nonlinear behavior of the eye, and f_{\max} is the maximum television frequency or the number of addressed pixels. The SQRI values are then in units of JNDs.

This image quality measure was tested extensively and compared to subjective and other measured values obtained from various authors. Results of such tests were excellent, with previously published data and SQRI predictions matching quite well. Furthermore, these tests included effects of resolution, contrast, luminance, picture size, and viewing distance variations.

1990 saw the development of a limited application image quality measure [39]. The MTF based Image Quality Index (IQI) was developed for screen-film mammography and had very good correlation to subjective assessments. However, the IQI operates on several major assumptions preventing it from being applicable to general imagery. The IQI assumes all objects are gaussian shaped, the optical system has a gaussian MTF, all system noise processes are white in nature, and the object size is above the minimum resolution.

With the increase in digital imaging came an increase in demand for image compression. Many full-reference image quality metrics began to emerge, including the now commonly known Signal to Noise Ratio (SNR), Root Mean Square Error (RMSE), etc [40]. Eskicioglu and Fisher

then reviewed several current measures of image quality in 1995 [41], particularly those that are reference or graphical based and not those that are measurement based. The review involved identifying which measures were effective for grayscale image compression. The results found were that no single-valued measure was adequate if multiple degradation mechanisms (noise, blockiness, blur, etc.) were present. By 1998, several more complex metrics emerged including that by Westen and Biemond [42].

During the 1990's, a split in image quality measures began to occur. On one side were the optical systems test based metrics including the MTF based metrics, and on the other side, was a group of "image quality measures" that measured image differences, generally for the use of measuring compression and encoding quality. With the increase in use of personal computers and the internet, the group of image difference measures grew rapidly and now includes more than eighteen different measures. These include full-reference metrics [42-54] requiring the original and deteriorated images, reduced-reference metrics [55, 56], requiring only a portion of the original image, and no-reference measures [57, 58] which are based solely on the output image.

Among these image difference based image quality measures, several claim to account for the human visual system (HVS) in some manner [42, 49, 50, 53, 56].

Rather than measure differences between an ideal image and an image degraded by diffraction and aberrations, the TIME Tool attempts to predict image quality based on test measurements. It

is therefore necessary to apply an image quality metric based on test measurements, particularly an OTF-based measure. For this reason, only the OTF-based image quality measures will be further reviewed.

Human perception of quality remains of high importance, and in 1996, Lee and Harris studied the effects of delaying the presentation of a test image after showing a reference image for forced choice comparisons [59]. The study was performed with gratings and showed that for intervals between 1 and 10 seconds, memory of contrast was affected. This is of particular interest for certain perceptual image test formats.

The General Image Quality Equation (GIQE) was developed as an adaptation of the NIIRS image quality in 1997, to convert it from a subjective ranking to a predictive ranking system [10]. The calculated GIQE value accounts for ground sampled distance, edge-sharpening ringing effects, relative edge response and the ratio of gain noise to signal to noise ratio. Results were well correlated with NIIRS rankings, showing that the GIQE is a good measure of image interpretability as determined by NIIRS objectives.

In 2001, it was discovered that blur threshold depends on edge contrast [60], a result important to image sharpness studies.

2002 saw the introduction of a new type of image quality measure—a structure-based measure [43]. Wang and Bovik claim the ability to model ANY image distortion as a combination of

luminance distortion, contrast distortion, and loss of correlation. The proposed Universal Image Quality Index (UQI or UIQI) does not account for the HVS. They claim better performance than the outdated Mean Square Error (MSE), but fail to compare it to other more recent image quality measures. The UQI has performed as well as any structural or image difference based image quality measures. Further modifications were published in 2006 with the inclusion of color perception through opponent color theory [45].

Also in 2002, Keelan published a book titled *Handbook of Image Quality: Characterization and Prediction* [5], in which he introduced the concept of the quality ruler, along with various information on perception, perceptual image quality testing, and working with multiple image attributes.

This work was later incorporated into an ISO standard [61-63], allowing absolute image quality to be discussed and compared. The work, summarized by Keelan and Urabe [64] is not the creation of a new image quality metric, but instead, presentation of tools to aid in linking metrics to perceptual image quality. Furthermore, it allows calibration of image quality test results such that the results can be communicated unambiguously.

In November 2004, Vollmerhausen et. Al presented a new metric called the Targeting Task Performance (TTP) metric [65]. Similar to the SQRI of Barten, the TTP was an integral of the square-root weighted ratio of the MTF and the CTF. Unlike Barten's SQRI, the TTP applied linear integration rather than logarithmic integration.

$$TTP = \int_0^{f_{\max}} \sqrt{\frac{C_{TGT} MTF}{CTF}} df \quad (3-15)$$

Additionally, the TTP introduces an average target contrast C_{TGT} to account for the reduced contrast typically found in long range imaging applications. Vollmerhausen et al claim a task performance probability proportional to the object range. In May 2006, results of applying the TTP as a predictor of night piloting of helicopters were presented [66].

Also important to mention is the cutoff spatial frequency, likely to have its origins early in the development of the OTF. This MTF-based measure of quality is similar to the limiting resolution. The cutoff-frequency measures the spatial frequency for which the modulation is 0 at all higher spatial frequencies. It is defined in Equation (3-16) in terms of focal ratio ($F^\#$) and can therefore be related to image spatial frequency or object spatial frequency.

$$f_{cut} = \frac{1}{\lambda F^\#} \quad (3-16)$$

For an object at infinity, the focal ratio is defined by Equation (3-17).

$$F^\# = \frac{f}{D} \quad (3-17)$$

Here D is the diameter of the exit pupil, and f is the focal length of the system.

For an object to pupil distance of l and a pupil to image distance of l' , the focal ratio is defined by Equation (3-18).

$$F_{obj}^{\#} = \frac{l}{D} \quad F_{img}^{\#} = \frac{l'}{D} \quad (3-18)$$

The cutoff frequency in the object ($f_{cut,obj}$) can then be related to the cutoff frequency in the image ($f_{cut,img}$) using the magnification (m) of the system as shown in Equation (3-19).

$$f_{cut,obj} = m f_{cut,img} \quad (3-19)$$

Although the presence of aberrations generally reduces the modulation for most spatial frequencies, it does not necessarily reach zero modulation at a frequency below cutoff. In many cases, a zero modulation will be reached in the mid-spatial frequency range but with non-zero modulation existing at higher spatial frequencies. This zero point is by definition NOT the cutoff spatial frequency. For aberrations up to several waves, it is common to have a non-reduced cutoff spatial frequency, and so, the cutoff frequency does not provide a good indicator of image quality.

It is worth noting that a larger diameter telescope (e.g. 24") with several waves of aberrations present may have low but noticeable contrast (around 0.1) for spatial frequencies higher than those that can be reached with a diffraction-limited telescope of significantly smaller aperture diameter (e.g. 7"). It is thus important to consider a telescope's condition relative to itself as well as in an absolute manner.

3.3 Normalized Metrics

The three metrics chosen for analysis throughout this research are the TTP base metric, the SQF, and the SQRI. All of them are applied to the analysis with visibly different results. Both the TTP and SQRI metrics are applied to the analysis in their inherent forms and also in a normalized form where the normalization is to the diffraction-limited value of the metric, found by evaluating the metric using a diffraction-limited MTF. The SQF is naturally normalized, but not to a diffraction limit.

Using normalized metrics for ranking provides additional insight into the relative usefulness of a telescope. To maximize the usefulness of the maintenance process developed for the TIME Tool, perceptual testing was conducted on an absolute basis rather than relative. That means that images were categorized based on their quality without knowledge of the simulation parameters, as opposed to categorization relative to the best imagery possible from a given telescope. This allows for restriction of image quality due to the manifestation of diffraction effects.

When a telescope is modeled in the simulation software, a telescope ranking based on its condition is provided, as well as the metric value and the boundary values for each ranking category. It can be immediately seen if a particular ranking is even possible for a given telescope. As an example, suppose an 18 inch diameter telescope with some aberrations is modeled in the software for a 30 mile object distance. The ranking provided is 3, and the metric value is 72. Then consider that the ranking category thresholds (the values separating adjacent rankings) are 118, 88, 60, and 21. One can see that even if the telescope were realigned and

brought to diffraction-limited performance (metric value of 100), rank 5 performance (capable of providing excellent imagery) could never be achieved for that aperture diameter at that range. This provides information to laboratory personnel for deciding if anything would be gained by working on the optical system. Simply providing a telescope ranking and a metric would not provide such insight since the maximum metric value for that particular telescope is not generally known.

Although the benefit of applying normalized metrics is clear, there are several disadvantages to applying them. In Chapter 4, analysis is provided that indicates the appropriate plane for metric evaluation is the object plane, allowing the metric value to reflect object range variations. However, if the metrics are normalized by their diffraction-limited metric value, the object distance parameter is removed. Consider a simple change of variables (C.O.V.), resulting in the TTP being inversely dependent on the object range, and the SQRI being independent of the object range.

$$TTP = \int_{u_{low}}^{u_{cut}} \sqrt{\frac{C_{TGT} MTF(aRu)}{CTF(bRu)}} du \rightarrow C.O.V \quad w = Ru \rightarrow \int_{Ru_{low}}^{Ru_{cut}} \sqrt{\frac{C_{TGT} MTF(aw)}{CTF(bw)}} \frac{1}{R} dw \quad (3-20)$$

$$SQRI = \int_{u_{low}}^{u_{cut}} \sqrt{\frac{MTF(aRu)}{CTF(bRu)}} \frac{1}{u} du \rightarrow C.O.V \quad w = Ru \rightarrow \int_{Ru_{low}}^{Ru_{cut}} \sqrt{\frac{MTF(aw)}{CTF(bw)}} \frac{1}{w} dw \quad (3-21)$$

Normalizing both metrics yields

$$TTP_{Norm} = \frac{\int_{Ru_{low}}^{Ru_{cut}} \sqrt{\frac{C_{TGT} MTF(a\omega)}{CTF(b\omega)} \frac{1}{R}} d\omega}{\int_{Ru_{low}}^{Ru_{cut}} \sqrt{\frac{CTF(b\omega)}{CTF(b\omega)}} d\omega} = \frac{\int_{Ru_{low}}^{Ru_{cut}} \sqrt{\frac{MTF(a\omega)}{CTF(b\omega)}} d\omega}{\int_{Ru_{low}}^{Ru_{cut}} \sqrt{\frac{MTF_{diff}(a\omega)}{CTF(b\omega)}} d\omega} \quad (3-22)$$

$$SQRI_{Norm} = \frac{\int_{Ru_{low}}^{Ru_{cut}} \sqrt{\frac{MTF(a\omega)}{CTF(b\omega)} \frac{1}{\omega}} d\omega}{\int_{Ru_{low}}^{Ru_{cut}} \sqrt{\frac{MTF_{diff}(a\omega)}{CTF(b\omega)} \frac{1}{\omega}} d\omega} \quad (3-23)$$

Both normalized metrics are then independent of the object distance. If the metrics are applied in this manner, an additional set of perceptual tests is required to establish the object distance dependence which is lost through normalization.

An additional disadvantage of the normalization process is the loss of constants. The TTP base metric naturally accounts for decreased target contrast, allowing for the modeling of low contrast imagery such as that obtained on days with poor atmospheric conditions. This target contrast parameter is lost in the normalization process, but since atmospheric effects are not accounted for in this research, this loss is tolerable.

Finally, in the SQRI metric, a constant value of $1/\ln(2)$ is introduced to scale the metric to units of Just Noticeable Differences. This is lost in the normalization process, and units cannot then be considered to be in JNDs, although evidence indicates that for the current application, the units were not in JNDs even before normalization.

Since both forms (normalized and non-normalized) have advantages, analysis is performed, compared, and presented for both cases as well as for the SQF in its inherently normalized form.

4.0 IMAGE FORMATION THEORY

Although image formation theory has been well developed, it is discussed in terms of image plane convolutions of a Point Spread Function (PSF) with a geometrically magnified image. Though this is correct, when the arguments are extended to Modulation Transfer Functions (MTFs), the effect of magnification is completely neglected. To overcome this deficiency, an alternative method of analysis is introduced in which the analysis is performed in the object plane, eventually yielding a natural MTF for accounting for magnifications and object distance.

4.1 Alternate Approach to Image Formation

The traditional view of the image formation process (illustrated in Figure 28) is the image plane convolution of the point spread function with the geometrically magnified object. A less conventional but equally valid view of imaging is the object plane convolution of the projected PSF with the object, followed by a geometric magnification of the result. The irradiance distribution in the object plane is then the unmagnified representation of the image. This latter approach, although yielding the same irradiance distribution, is the correct one to use for systems operating at non-unity transverse optical magnifications [67]. This approach also naturally leads to using an object plane MTF in calculating metrics.

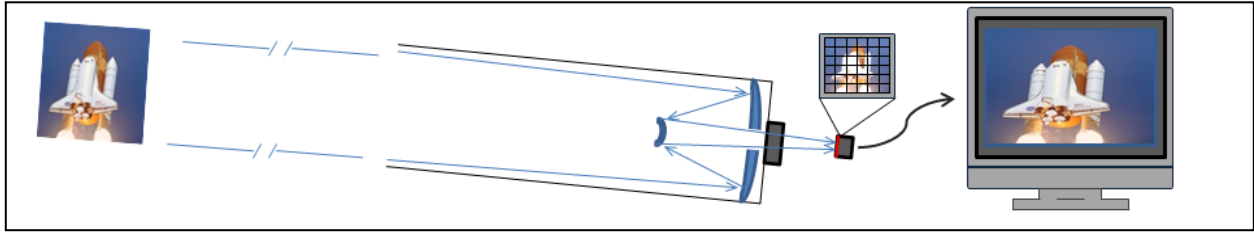


Figure 28. A long-range imaging device creates a non-ideal replication of an object on an image plane (red line) which is displayed visually with some display magnification. The display is then viewed by an observer from a viewing distance d .

Transfer and threshold function curves in the image plane can be transferred to the object plane using the optical magnification (m) of the system. Although it is most accurate to use the absolute value of m , the absolute value sign is dropped from the following analysis since the sign of the magnification has no significance in transfer functions.

$$\text{MTF}_{\text{obj}}(u_x, u_y) = \text{MTF}_{\text{obj}}\left(\frac{u_x}{m}, \frac{u_y}{m}\right) \quad (4-1)$$

The viewing distance (d) allows retinal frequencies to be converted to spatial frequencies at the display ($u_{\text{disp } x}, u_{\text{disp } y}$) which can then be related to image spatial frequencies by a factor of the display magnification (M).

$$\text{CTF}_{\text{obj}}(u_x, u_y) = \text{CTF}_{\text{disp}}\left(\frac{u_{\text{disp } x}}{mM}, \frac{u_{\text{disp } y}}{mM}\right) \quad (4-2)$$

The following assumptions are made regarding the relative usefulness of two images: (i) for two images with equal feature sizes, the image with the smallest visible feature is the image with

greater usefulness, and (ii) if two images are not displayed with equal size, the relative usefulness of the two images cannot in general be determined.

It is well known from linear systems theory [68] that the complex pupil function (p), the point spread function (PSF), and the modulation transfer function (MTF) are all related by Fourier Transform operations.

$$\boxed{
 \begin{array}{ccc}
 p(x, y) & \xrightarrow[\substack{u_x = \frac{x}{\lambda f}, \quad u_y = \frac{y}{\lambda f}}]{|\text{Fourier Transform}|^2} & \text{PSF}(x_o, y_o) \\
 & & \xrightarrow{|\text{Fourier Transform}|} \text{MTF}(u_x, u_y)
 \end{array}
 } \quad (4-3)$$

The complex pupil function is composed of an aperture transmittance function $t(x,y)$ and a phase, both of which are normalized to the pupil diameter (D). Writing the complex pupil function in terms of absolute variables rather than normalized variables yields

$$p(x, y) = t\left(\frac{x}{D}, \frac{y}{D}\right) \exp\left(j \frac{2\pi}{\lambda} W\left(\frac{x}{D}, \frac{y}{D}\right)\right) . \quad (4-4)$$

When transformed, the similarity theorem dictates that the Fourier Transform of the complex pupil function (the Amplitude Spread Function labeled ASF) will be a function (F) of the variables Du_x m and Du_y m.

$$\text{ASF}(u_x, u_y) = F(m D u_x, m D u_y) . \quad (4-5)$$

Solving the thin lens law for image distance, substituting into the expression for magnification and making a long-range imaging approximation such that the object distance (R) is much greater than the focal length (f), yields Equation (4-6).

$$m = -\frac{f R}{R(R-f)} = -\frac{f}{(R-f)} \cong -\frac{f}{R} . \quad (4-6)$$

Given the appropriate substitutions for spatial frequencies from Equation (4-3), and for some constant C, the PSF in the object plane is then a function of the form

$$PSF(x, y) = C \left| F \left(\frac{m D x}{\lambda f}, \frac{m D y}{\lambda f} \right) \right|^2 = C \left| F \left(\frac{f D x}{R \lambda f}, \frac{f D y}{R \lambda f} \right) \right|^2 = C \left| F \left(\frac{D x}{R \lambda}, \frac{D y}{R \lambda} \right) \right|^2 . \quad (4-7)$$

Transforming to obtain the MTF yields a function (G) of variables $R\lambda u_x / D$ and $R\lambda u_y / D$, the result being independent of focal length, but showing the relation of the MTF to the object distance R.

$$MTF_{obj}(u_x, u_y) = G \left(\frac{f \lambda u_x}{m D}, \frac{f \lambda u_y}{m D} \right) = G \left(\frac{R \lambda u_x}{D}, \frac{R \lambda u_y}{D} \right) \quad (4-8)$$

4.2 Object Distance, Magnification, and Image Quality

From the classical approach to image formation, consider an image of an object formed in the image plane as a convolution of the telescope Point Spread Function with the geometric image. As object distance (range) increases, the optical magnification necessarily decreases as indicated by Equation (4-6), resulting in a smaller geometric image. Since the Point Spread Function in the image plane is unaffected by object distance, the PSF remains the same size. The relative size of the PSF to a given feature of the object then increases as the object range increases. This causes a more pronounced blurring of the feature than at a closer range. This is illustrated below Figure 30 by the convolution of a constant diffraction-limited PSF with various sized objects. The objects are dark rectangles on a white background, similar to viewing a seam (black) on a space shuttle wing (white), illustrated in Figure 29. The initial contrast is unity.

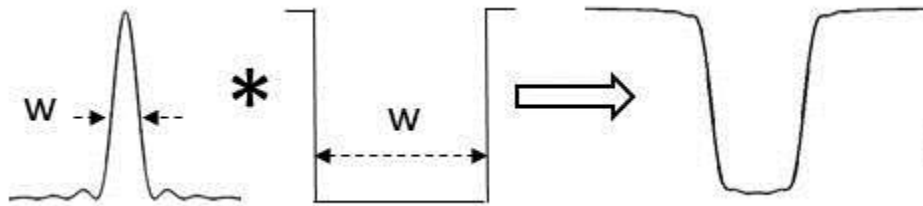


Figure 29. Objects represented as 100% contrast black bars are convolved with a PSF.

As the object (feature) width is decreased (or equivalently as the range increases for an object feature), the total blur width relative to the original feature width becomes larger, and contrast is lost, as illustrated in Figure 30.

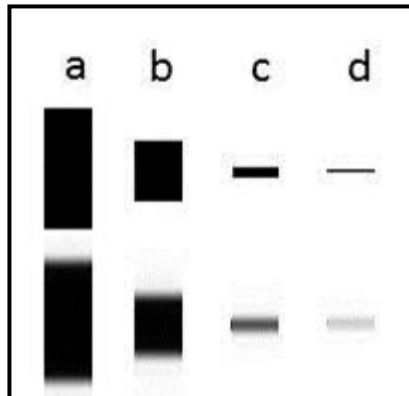


Figure 30. As the width of a feature decreases relative to the PSF width, image contrast decreases and blur becomes more dramatic.

For features which are large compared to the PSF, little contrast is lost. For features approximately equal in width compared to the PSF, contrast loss becomes more appreciable. For features which are small compared to the PSF, a significant loss of contrast occurs. The widths of the PSF and objects shown in Figure 30 as well as resulting image contrast are provided in Table 9.

Table 9. Object and PSF widths (arbitrary units) and resulting image contrast for the illustrations of Figure 29 and Figure 30.

	width (w)	image contrast
PSF	71	
a	241	0.97
b	121	0.93
c	21	0.51
d	5	0.10

This can also be seen with more complex objects by comparing Figure 31 through Figure 33. As the object range increases from 5 miles (Figure 31) to 30 miles (Figure 32) to 60 miles (Figure 33), the change from 0.5λ to 0.75λ of balanced astigmatism has a greater impact on the image quality.

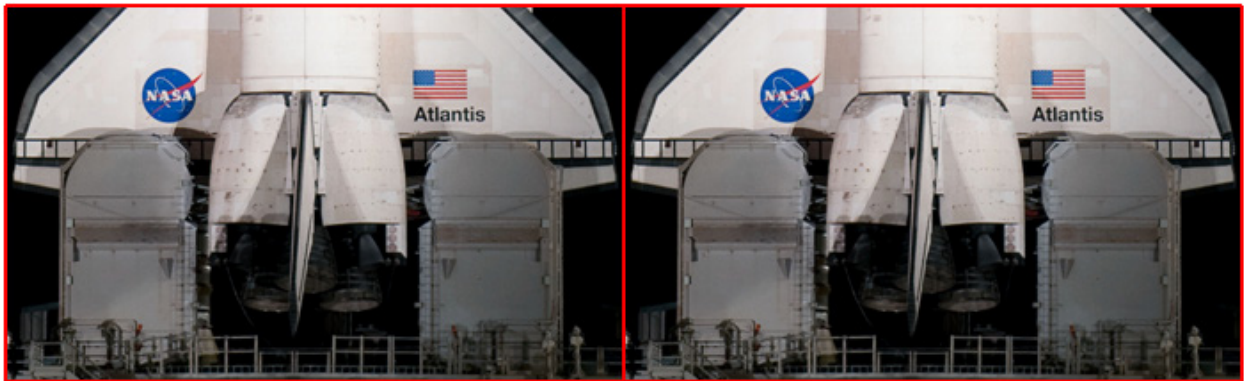


Figure 31. Simulated imagery for an object range of 5 miles with the presence of 0.5λ of balanced astigmatism (Left) and 0.75λ of balanced astigmatism (Right).

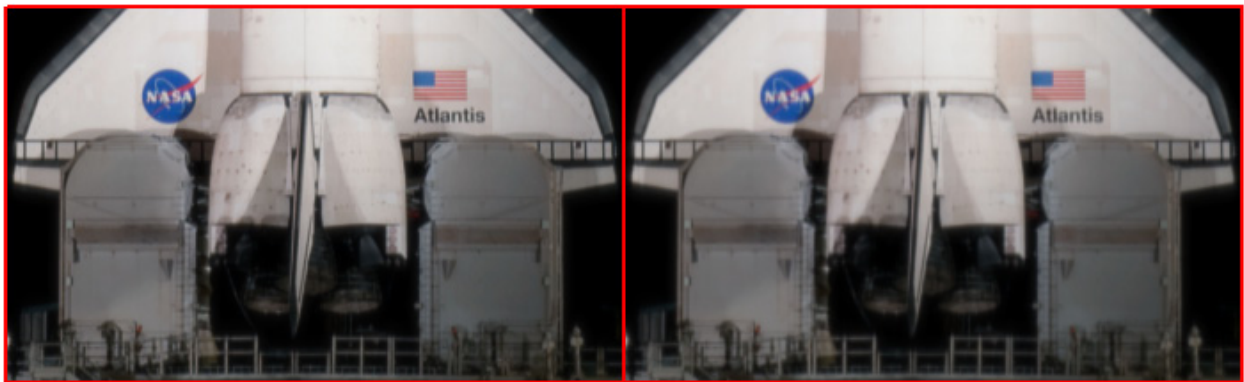


Figure 32. Simulated imagery for an object range of 30 miles with the presence of 0.5λ of balanced astigmatism (Left) and 0.75λ of balanced astigmatism (Right).

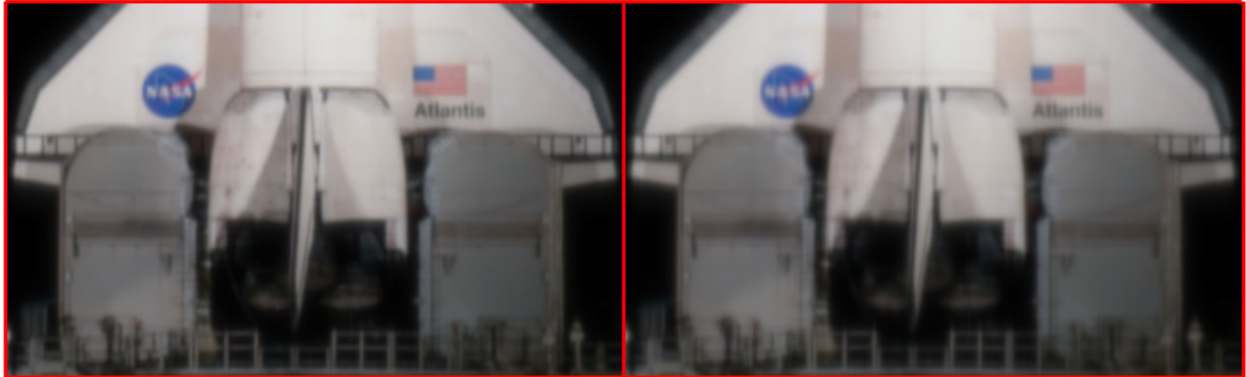


Figure 33. Simulated imagery for an object range of 60 miles with the presence of 0.5λ of balanced astigmatism (Left) and 0.75λ of balanced astigmatism (Right).

In this manner, all features become more blurred at longer object distances although the effect may at times be below the visible threshold. For large features, a larger increase in object distance is necessary to see the difference in blur since the blur width must reach an angular width greater than the resolution of the eye. For small features, the effects may not be visible since they may be below the size of the image sampler resolution.

From the above arguments, it can be immediately concluded that aberrations and diffraction affect image quality more at longer object distances than at close distances. Although decreasing aperture diameter and increasing aberrations increases the PSF size, at close ranges, no change in image quality may be noticeable. At long object distances, only slight variations in aperture diameter or aberrations can significantly affect image quality. Thus, the sensitivity of a system to aberrations is heavily dependent upon object distance.

5.0 PERCEPTUAL TESTING

Perceptual testing is a broad area of psychophysical data collection in which the extraction of a subject's opinion is the fundamental measurement goal. Such testing can be applied to a variety of areas of interest besides that of image quality. Typically during such testing a subject is asked to provide an absolute opinion of a stimulus, or the opinion of a stimulus relative to some reference. Depending on the test being applied, stimuli may be presented one at a time, in pairs, in triplets, or in larger numbers (typical of a sort type of perceptual test). The ability for a subject to make a definite distinction between two stimuli differing in a single attribute is governed by Weber's Law, Fechner's Law, or the Weber-Fechner Law. These laws are the basis for the concept of the Just Noticeable Difference, a unit often encountered in perceptual testing.

Weber's Law, commonly stated, indicates that the minimum stimulus change (Δr) that is detectable depends on the base stimulus quantity (r) present before the change occurs. Further, it indicates that the proportion of detectable stimulus change to the base stimulus level is a constant (k). Mathematically,

$$\frac{\Delta r}{r} = k \quad (5-1)$$

Weber's Law is approximate and typically fails in extreme cases such as very low contrast images, very heavy weights, or other particularly strong or weak stimuli where an equivalent "saturation" or "noise threshold" situation is encountered.

The Fechner Law, similar to Weber's Law, introduces an absolute stimulus threshold parameter r_0 . The magnitude of sensation (s) is then proportional to the natural logarithm of the ratio of stimulus to threshold stimulus.

$$s = c \ln\left(\frac{r}{r_0}\right) \quad (5-2)$$

One or both of the Fechner or Weber Laws are frequently referred to as the Weber-Fechner Law. As applied to this research, there is little need to distinguish between the three Laws, but rather to recognize that they all indicate a constant relationship between the stimulus presented and the stimulus change required for an observer to sense a change.

5.1 Methods of Testing

A large number of psycho-physical image quality tests are available to extract observer opinions regarding perceptual image quality. Although variations of some may occur, the following non-exhaustive list of perceptual tests have appeared in publications, and are applicable to perceived image quality.

Perceptual image tests can be categorized either as single stimulus or double stimulus methods. In single stimulus experiments, observers are shown an image or a pair of images once, then asked to perform some task with the stimulus. The task may be assigning a number to an image, choosing which image is better, or placing the image into a position relative to other images. Double stimulus experiments involve exposing an observer to an image, removing the image, then exposing the image to the observer again, before asking the observer to complete a task. It

is common in double stimulus experiments for a reference image to be shown, then a test image, followed by the reference image and finally the test image.

The most common tasks for an observer to be instructed to perform during perceptual image testing are: (1) Assign a numerical value representing some attribute such as sharpness or noisiness to an image. [69] (2) Sort an image into predefined categories. [70] (3) Sort a set of images into ascending or descending order of some attribute such as sharpness or noisiness. [5] (4) Choose the image from a pair which appears to have the higher attribute level. [70] (5) Choose the image from a pair which appears to have the higher attribute level and assign a numerical value to quantify the difference. [69]

Images used in a perceptual test may be printed, projected, or electronically displayed. Images are frequently ordered randomly to prevent responses based on expected patterns and to reduce the learning effects which may occur in psycho-physical experiments.

Since it is best to use the simplest theory which is adequate in describing the situation under test, only the Paired Image Comparison (a.k.a. the Two Alternative Forced Choice Test) and the Categorical Sort Test were applied in the research presented here. Further details regarding other methods of perceptual testing then are not included.

5.2 Test Conditions

In part 1 of ISO standard 20462 [61], standards for viewing conditions are established. These are excellent for allowing experiment results to be directly compared with others conducted under the same conditions. Unfortunately, image analysts will not be particular in setting luminance levels or ensuring that reflectivities of prints are according to standards. In fact, the actual conditions that will be encountered by image analysts are unknown and will certainly vary by organization and by individual observer. Ultimately, observers will adjust whatever conditions they have control over to maximize their image analysis abilities. This may include adjustment of ambient lighting, variations in viewing distance, angle at which an image is viewed, etc. Further, many conditions will be uncontrollable by the analysts and will still vary by establishment—printer quality, image paper reflectivity, lighting type (fluorescent, incandescent, natural, etc.), and a host of others. For this reason, it was decided that whatever reasonable facilities were available would be used for testing without regards to strictly following established standards. The results then represent an “average” analyst in “average” conditions.

5.3 Categorical Sort

In the Categorical Sort Test, observers are presented with one image at a time, with a task of sorting the images into the category they feel is most accurate. For the current application, observers are asked to sort a series of images into the categories of Excellent, Good, Fair, Poor or Unusable, in terms of the usefulness of the imagery to launch imagery analysts. The “Unusable” category then is not unusable in the sense that the image content cannot be recognized, but that important image information such as recognition and identification of vehicular damage cannot

be extracted. Images must be placed in exactly one category. Results are tabulated in a matrix such as that shown in Table 10. Each row in the data matrix corresponds to a single image presented in the test, and the sum across each row equals the number of observers. Each column of the data matrix represents a category in which the image could be sorted into. The top row of Table 10 indicates that the first image was considered excellent by 3 observers, good by 6 observers, fair by 4 observers, poor by 2 observers, and unusable by none of the 15 observers.

Table 10. Example of a data matrix resulting from Categorical Sort Testing. Columns correspond to categories and rows correspond to images.

3	6	4	2	0
1	6	6	1	1
0	2	11	1	1
0	0	6	7	2
0	2	5	6	2
1	1	1	10	2
1	0	3	6	5
0	1	0	5	9

Standard analysis of the perceptual test data is available through references [70, 71]. The analysis process begins with transforming the probability matrix of Table 10 into a cumulative probability matrix. Applying assumptions about the category dispersions and correlations reduces the amount of data required for analysis, but also restricts the results. Least squares data fitting yields data scale values (arbitrary but necessary) as well as scale values representing the category boundary values. By plotting the metric value for a given image against its assigned scale value (Figure 34), a linear plot (assumed in the least squares data fitting process) can be assigned. This allows interpolation and extrapolation to the scale values of the category

boundary values. These boundary values can then be converted to metric values using the slope and intercept found in the linear plot.

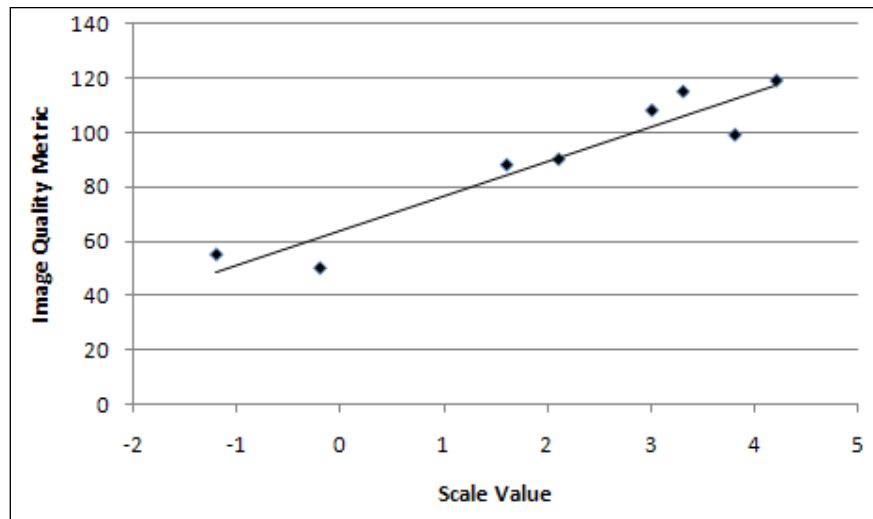


Figure 34. Standard analysis of perceptual test data yields a scale value for each “image point” and scale values corresponding to category cutoffs. Using the linear relationship, boundary cutoffs can be converted to metric values.

After obtaining category boundary values under various parametric variations, trends can be determined to allow interpolation and extrapolation of the breakpoints to other untested values (Figure 35).

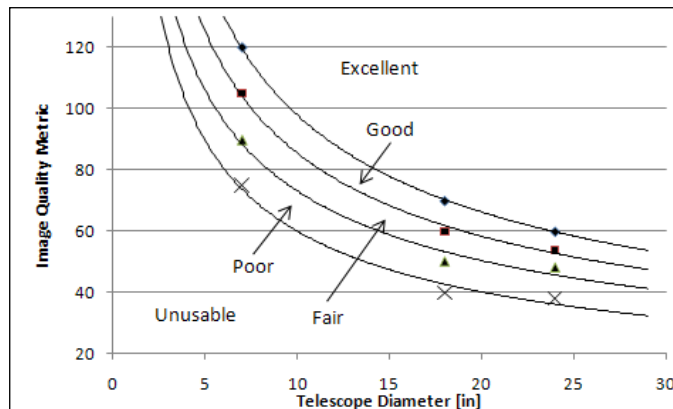


Figure 35. Hypothetical results of perceptual image quality testing at three data points.

5.4 Paired Image Comparisons

The Paired Image Comparison Test is another perceptual test [71] which differs significantly from the categorical sort in format and purpose. In the Paired Image Comparison, observers are presented with image pairs (Figure 36) which vary in a single attribute, their task being to choose which of the pair they consider to be better, brighter, etc.



*Original image used in simulations from <http://www.nasa.gov>

Figure 36. A sample pair of images presented to an observer in the paired image comparison test. The observer's task is to select which image of the pair is of higher quality.

The purpose of this test is to determine Just Noticeable Differences of parameters. Each image pair consists of a “reference” image and a “test” image. Image pairs vary in a single image attribute or metric and may be very close in quality. In most cases, to discover any useful information, a sequence of image pairs must be presented, each in the sequence containing the same reference image, but the test images varying in attribute or metric.

As an example, a sequence of images may consist of a reference image and six images varying in amount of third order spherical aberration (Figure 37). This creates six image pairs to be presented.



Figure 37. Just Noticeable Differences are determined from a sequence of paired comparisons. The reference image (outlined in red) is paired with each of the remaining 6 test images, creating six pairs of images.

After presenting the sequence of image pairs to all observers in the group, a data table is constructed using the format shown in Table 11. Each row corresponds to a single image pair, the left column containing the attribute value present in the test image, and the right column is the number of times the reference was selected over the test image. Standard analysis of the

perceptual test data is available through reference [71]. Results of the analysis lead to the attribute Just Noticeable Difference quantity.

Table 11. Paired comparison data. The left column is the attribute value, the right is the number of times the reference image was selected by the group.

0.05	1
0.09	2
0.11	4
0.16	8
0.18	9
0.19	9
0.25	13
0.34	15

5.5 Just Noticeable Differences

A Just Noticeable Difference (JND) is the minimum amount of change in some image attribute or image quality metric (i.e. aberrations, Strehl Ratio, wavefront variance, etc.) that results in detection by human observers, and it is generally considered to be governed by the Weber-Fechner Law. The minimum detectable change may vary slightly between observers so it is defined probabilistically for a group of observers.

It is assumed that if two images differing by one 50% JND (one JND) are compared, and an observer is instructed to pick the better quality image, the correct image will be chosen 50% of the time. The remaining 50% of the time, the observer is unable to determine which is of higher quality, and randomly chooses one image, each image having an equal probability of being

chosen. That leads to a 75% success rate of the correct image being chosen—50% from proper selection, and 25% from random selection when a difference is not discernable to the observer.

Stated mathematically:

$$p_c = p_d + \frac{1 - p_d}{2} = \frac{1 + p_d}{2} \quad (5-3)$$

where p_c is the probability of a correct response (the higher quality image is chosen, even if by random) and p_d is the probability of detection (higher quality image is recognized and chosen).

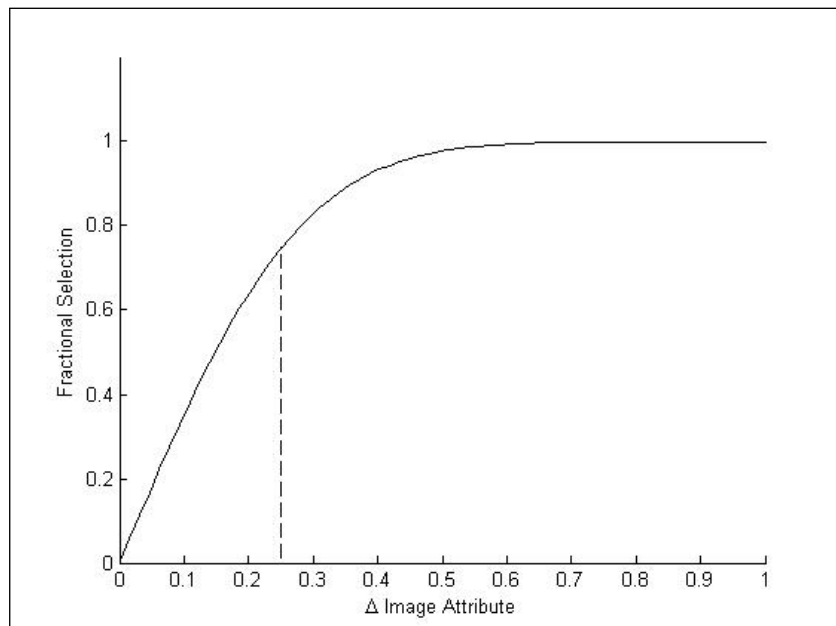


Figure 38. After a sequence of image pairs has been presented to a group of observers, the fractional selection of the reference image over the test image is determined for the group. The change in image attribute necessary to generate a 0.75 fractional selection defines the Just Noticeable Difference of that attribute, here, about 0.25 units.

As an example, focal length variations are expected to yield no changes in perceived image quality. If images generated with several different focal lengths are compared with a reference image which is generated with a known focal length, the amount of focal length change needed to create a Just Noticeable Difference (JND) will be determined. If the focal length change needed to create a single JND is very small, image quality is then highly sensitive to the focal length. However, if the change in focal length needed to create a single JND is very high, then image quality is insensitive to focal length, and no categorical testing for focal length variations is necessary.

6.0 SIMULATED IMAGERY

Throughout this research, several perceptual tests were conducted in order to extract the effects of various parameters on the overall opinion of the quality or usefulness of images. To generate such imagery with broad ranges of aperture diameters, focal lengths, and aberrations using photographic equipment would be nearly impossible. Instead, software was created which simulates imagery by synthesizing an exit pupil, allowing the introduction of aberrations, changing focal lengths, or modifying aperture diameters. The flexibility of using software generated imagery includes the ability to maintain relative color content and brightness in images. The difficulty in using synthetic digital imagery is the lack of natural scaling of imagery with object distance or focal length induced changes in magnification. To achieve this, one would need to introduce interpolation degradations inherent with rescaling digital imagery. To avoid this, all images were kept the same size and were considered in metric evaluation to have undergone appropriate display magnification changes which would support this common sized imagery.

6.1 Size, Resolution, Content

The image content used in subjective evaluation tests for this research was chosen to be familiar to the observers, allowing the recognition of the subject matter and knowledge of the size of object features. Object-representing images were bitmap format to prevent compression losses. High quality images were chosen to represent objects, and all imagery was displayed electronically on a high resolution monitor set to 1140×900 for categorical sort tests and to

1920×1200 for paired image comparison tests. Image sizes were selected such that the images (or pairs of images) could be displayed in their entirety without the need to scroll the display.

The image size varied by image and consisted of images of the “Space Shuttle Atlantis on the launch pad at night” (Figure 39), “house with fence” (Figure 40), “trees” (Figure 41), and “house with shrub” (Figure 42). The Space Shuttle image is 768×960 pixels with a 24 bit image depth, has an actual width of 8 inches and a height of 10 inches, with a resolution of 96dpi . The house with fence, trees, and house with shrub images are all 794×971 pixels with 24 bit image depth, and have actual widths of 4.4375 inches and heights of 5.375 inches, with resolutions of 96dpi.

The space shuttle image was chosen for the categorical sort testing so that rankings would be established for relevant image content. Since the paired image comparisons were used to establish a general phenomenon, scenes were chosen to:

1. Primarily consist of man-made objects (a house and a fence).
2. Primarily consist of natural objects (trees against the sky).
3. Consist of a combination of man-made and natural objects (a shrub in front of a house).

Although portraits and human subjects were not included in the above selection, since the primary application of this research is to long range imaging telescopes, humans are unlikely to be the subjects of the imagery, and portraits would certainly not be included in the application.



*Reproduced from <http://www.nasa.gov>

Figure 39. Image of the Space Shuttle Atlantis on the pad, used extensively throughout perceptual tests conducted for this research. The image is shown here at 50% of its actual 8"×10" size.



Figure 40. House with fence image used in paired image comparisons. This image shown at actual size.



Figure 41. Trees image used in paired image comparisons. This image is shown at actual size.



Figure 42. House with shrub image used in paired image comparisons. This image is shown at actual size.

6.2 Simulation Generation

The software developed for the synthetic generation of digital imagery used in perceptual testing operates on the object plane convolution of the object with a Point Spread Function (PSF), as

discussed previously. The software generates a complex pupil function based on user-defined aperture diameter, focal length, obscuration ratio, and aberrations (third order and lower). From the complex pupil function, a PSF is generated using Fourier Theory. This PSF is then convolved with an input bitmap picture file representing an object. The convolution operation is performed using Fourier Transforms, as shown in Equation (6-1), to improve computational efficiency by avoiding the unnecessary use of system resources required for direct convolution operations.

$$\text{Image} = \text{Geom. Image} ** \text{PSF} = \mathfrak{I}^{-1}(\mathfrak{I}(\text{Geom. Image}) \times \mathfrak{I}(\text{PSF})) \quad (6-1)$$

The complex pupil function is generated based on a single wavelength. Diffraction effects are then encountered only for this wavelength and not for the entire visible band. Further, since bitmap format image are used, the image is broken into its three constituent color planes (red, green, blue), and the convolution is performed on each color plane separately. The convolution of the PSF and “geometrical image” represented by the bitmap is performed with a single monochromatic PSF for all three color planes. After the convolution, the color planes are reassembled into a bitmap image representing the image output of the telescope. This process is illustrated in Figure 43.

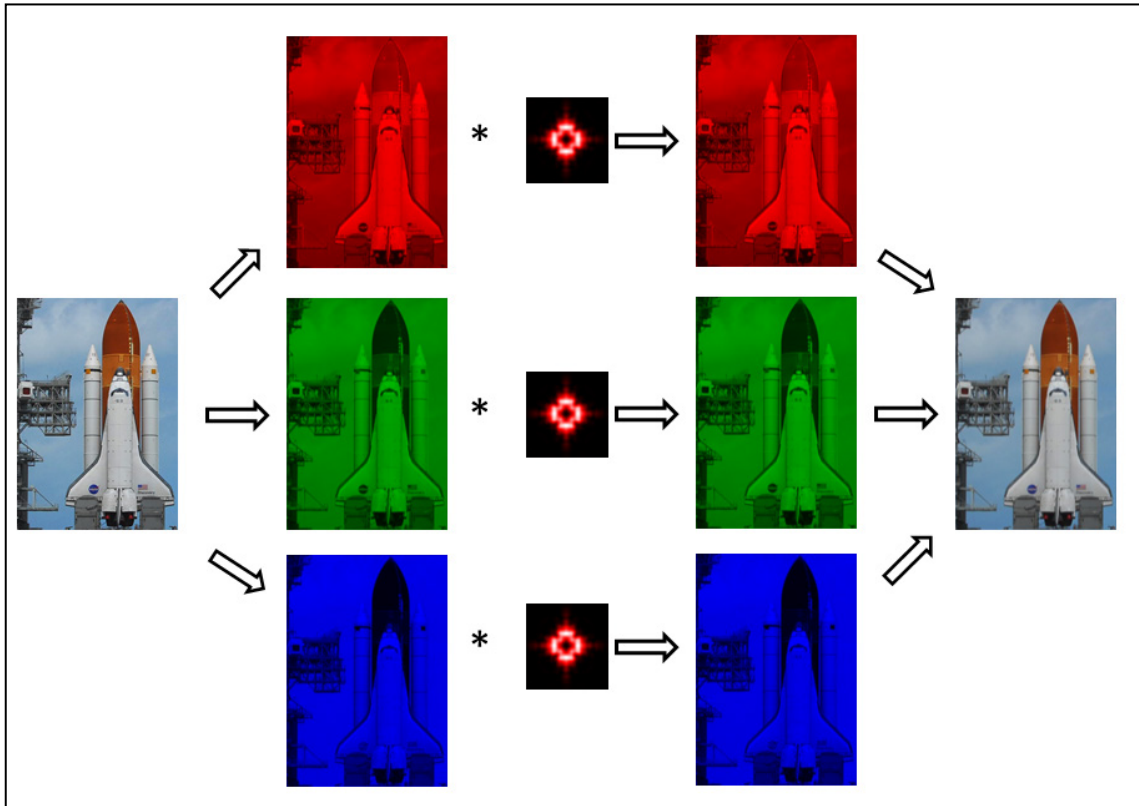


Figure 43. Left to Right, a bitmap image representing the “object” , is split into its red, green, and blue constituent color planes, each color plane is convolved with a single monochromatic PSF. The color planes are recombined into a single output bitmap file representing the “image”.

To avoid the undesirable distortions and degradations introduced by interpolation, simulated images are left at the original size of the bitmap image. Hence, a display magnification is assigned for the largest image magnification encountered in the testing, (based on an assumed detector size) and all other images are assigned a display magnification such that the images generated all have the same final display size. The adjustment of display magnification compensates for decreases in image sizes caused by increases in object range or decreases in focal length. Assumptions employed in synthesizing images are discussed in the following chapter.

7.0 RESEARCH ASSUMPTIONS

As is the case in most practical applications of physics and engineering, a number of assumptions were made to reduce the computational intensity associated with a complete system model, increase simplicity and intuition, and to reduce the amount of perceptual testing that would be otherwise necessary. A reasonably exhaustive list of assumptions made in image synthesis and perceptual testing are shown categorically below, followed by a brief discussion of each and the implications of making such assumptions.

The categories of assumptions are: General, Computer Modeling, and Perception/ Perceptual Testing. The General category is for assumptions made in the modeling process and include assumptions about how imagery would be used by analysts and under what conditions. Also included in this category are expectations of who will use the information presented in this dissertation. The Computer Modeling Category includes assumptions and approximations made in image synthesis. Perception/ Perceptual Testing assumptions are based on the way perceptual testing is conducted and the assumptions made in data collection and analysis. Also included in this category are assumptions about perceptual effects.

7.1 General Assumptions

It is assumed that third order aberrations dominate and higher order aberrations can be neglected, and are therefore not modeled in the image simulation software. Aberrations such as fifth order spherical aberration are then not modeled, although they may be present in telescope implementation. This assumption is made in part because it is logical, but also in part due to restrictions in the interferometric analysis software used in the TIME Tool maintenance process. The interferometric analysis software computes aberration coefficients through a much higher order than third, but only reports the Seidel aberrations. Thus, the presence and magnitude of higher order aberrations are transparent to the optical testing and analysis personnel.

It is assumed that telescope operators maximize image quality and the optimum quality corresponds to aberrations which are balanced to minimize RMS wavefront error. The aberration combinations which yield minimum RMS wavefront error are shown in Table 3. The low order aberrations used to balance higher order aberrations are tilt and defocus, both of which are assumed controllable by telescope operators. Tilt would be introduced by an operator by decentering the launch vehicle, and defocus would be controlled by focus adjustments. Operators may not have control over tilt and defocus in cases where the telescope has a pre-programmed trajectory for tracking. If manual control is allowed, the operator is assumed to adjust the focus to create the best perceptual image quality and it is assumed that the operator and image analyst would agree (within reason) on what is the best image quality.

It is assumed that monochromatic modeling of diffraction is adequate for extraction of quality boundaries for the average analyst through perceptual testing. Strictly speaking, diffraction effects are wavelength-dependent and should vary over the visible spectrum. However, bitmap images are used to represent objects, and immediately reduce the ability to introduce such wavelength-dependent diffraction to three colors (red, green, and blue). To reduce the programming complexity that would result from performing the diffraction calculations for three colors, diffraction is only calculated for a single color, selected as the wavelength used for interferometry (typically 632.8nm). If the RGB bitmap color planes are considered to have wavelengths of 475nm, 510nm, and 633nm, respectively, there is then a 25% error in diffraction blur size for blue, relative to red. Although this is a significant error, it is justified by the computational resource limitations imposed by the budget. It is an error born of necessity.

LVIT are rather narrow field instruments, which leads naturally to the assumption that the field dependence of aberrations such as astigmatism can be neglected and that the quantity of aberrations measured by the interferometry can be applied uniformly across the field. This assumption is further justified in that single on-axis interferograms are captured and analyzed for each telescope yielding no information about the field-dependent portion of aberrations.

It is assumed that LVIT are corrected for all chromatic aberrations to a high enough degree to prevent the necessity of inclusion of such aberrations in the modeling. The LVIT were originally designed to be well-corrected for longitudinal and transverse chromatic aberrations. After off-the-shelf Barlow lenses were included in the optical train, the level of achromatism was

decreased significantly. However, it is assumed that the presence of chromatic aberrations does not change the usefulness of imagery for an analyst, only the aesthetic appeal. The assumption that LVIT are achromatic extends to higher order chromatic aberrations such as spherochromatism and other color-dependent aberrations.

It is assumed that no atmospheric turbulence effects (PSF broadening, wandering, scintillation) are present. This assumption will almost never be satisfied, even approximately. However, since the atmosphere is out of the control of LVIT test and maintenance personnel, it is neglected to allow best case decisions to be made. Although atmospheric effects will likely dominate LVIT applications, the presence of diffraction and aberrations will still have a significant impact on image quality, particularly when atmospheric conditions are moderate or good.

It is further assumed with no justification that vibrations are negligible. Although the exclusion is unjustified, it is necessary since no vibration measurement data is available for inclusion.

It is assumed that detector/digitization effects are small compared to geometrical effects and aberrations. Since the upgrade of nearly all Eastern Range telescopes to high definition cameras, it is a reasonable assumption that all detector effects are relatively small.

7.2 Computer Modeling Assumptions

It is assumed that bitmap picture formats provide an adequate object representation. Although a single planar object (a bitmap image) is used to represent a three dimensional object (i.e. a launch vehicle), the variation of focus with depth that would occur in reality is insignificant as a result of the object distance. Taking a minimum range of 1500 feet and considering an approximated maximum depth of field expected to be 300 feet (about the height of the space shuttle or a large rocket), a difference of approximately $0.1\mu\text{m}$ occurs between the image plane locations. Although this may be expected to yield a small change in image quality for far and near regions of the object, this is a worst case and would require the space shuttle to be pointed exactly away from the telescope. Useful imaging through the exhaust of the vehicle would be impossible. Considering a more likely tracking scenario of a vehicle with a 30 foot depth and nearly perpendicular to the telescope would yield a difference of image planes for maximum and minimum depths of field to be on the order of 40nm —rather insignificant.

It is assumed that a PSF of at least 25 points in width (interpolated to object coordinates) provides adequate modeling accuracy. The PSF width was chosen somewhat arbitrarily and the accuracy is as dependent on the bitmap resolution as the PSF width.

It is assumed that PSF and MTF interpolations have little effect in image quality analysis. Interpolation of the PSF to object coordinates is directly connected to the PSF minimum width mentioned above. Interpolation of the MTF is not for changing scales dramatically, but simply to find more convenient samples of the MTF. This is then used in two dimensional integral

calculations with MTF arrays generally on the order of 300×300 points. Interpolation between data points with such fine sampling will yield little error, particularly compared with errors that can occur in the perceptual testing in which the metric values are used.

It is assumed that image interpolations may significantly alter the perceived image quality and should therefore be avoided. Although PSF and MTF interpolations are considered to contribute only small errors, it is expected that image interpolations (needed in resizing operations such as zooming) have a rather significant effect on perceived image quality. The interpolation process may artificially sharpen the image, raising the perceived quality (up to a point where over-sharpening would be considered to lower quality), or it may artificially blur edges, immediately lowering the perceived quality. Interpolations may cause color changes in the blurring and sharpening, and it may cause “blockiness” of the image. Perceptual testing assumes that only a single image quality parameter (aperture diameter, noise, contrast, etc.) changes in a given test. If any other changes of image quality occurred due to image resizing or zooming, analysis of the test results would be invalid. Hence, it is important that the image resizing that would occur from changes in magnification be considered to be compensated by varied display magnification such that the image bitmap can remain the same size in all cases.

7.3 Perception/ Perceptual Testing Assumptions

Within the applicable range of obscuration ratios, it is assumed that changes in the obscuration ratio for LVIT have no discernable effect on perceived image quality. The obscuration ratios encountered on the LVIT are 0.3 or 0.35. It is assumed that changes between those two values has little effect on the perceived image quality. Shown (Figure 44) are MTF curves for 0.3 and 0.35 in the presence of various amounts of third order spherical aberration, balanced appropriately with defocus to minimize RMS wavefront error. Note how little variation there is between pairs as the magnitude of spherical aberration increases.

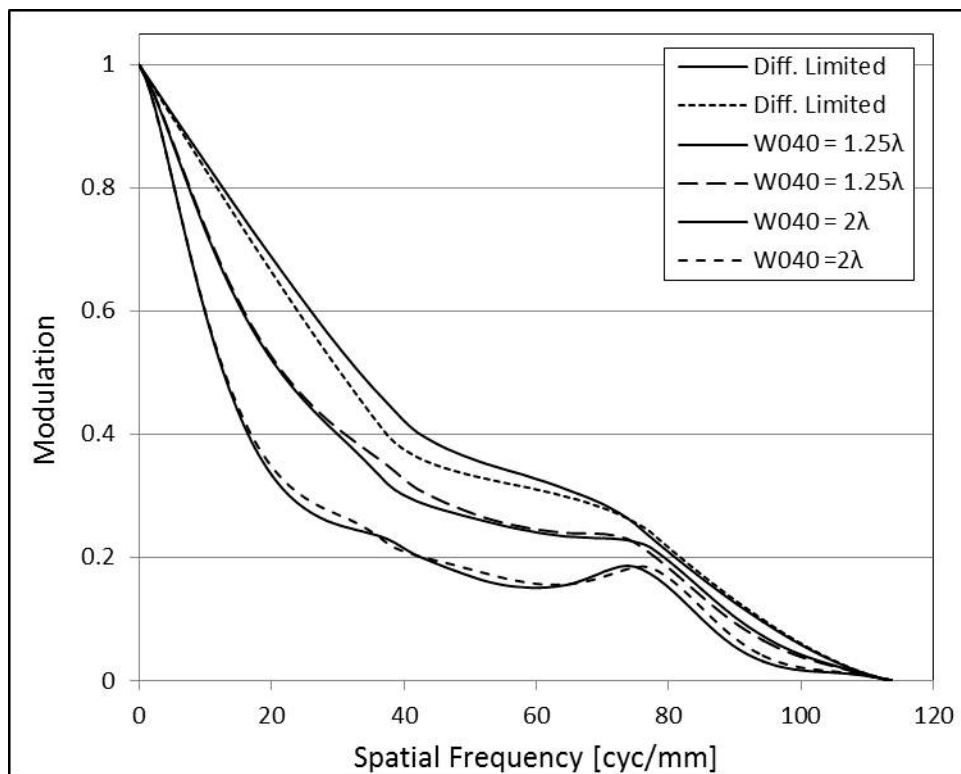


Figure 44. MTF curves for obscuration ratios of 0.3 (solid curves) and 0.35 (dashed curves) for diffraction-limited, 1.25λ of balanced spherical aberration, and 2λ of balanced spherical aberration.

It is assumed that the induced change in perceived image quality resulting from rotation of aberrations is negligible. For rotationally-symmetric aberrations such as third order spherical aberration, there is obviously no difference. However, for coma and astigmatism, changes may be detectable under certain conditions. The contrast threshold function (CTF) of the human eye is frequently approximated by a rotationally symmetric function, as done throughout this research. In reality, the CTF has angular dependence with minimum threshold contrast occurring at multiples of 90° with maximum threshold contrast at multiples of 45° . Thus, horizontally and vertically oriented objects are easier to resolve than those at other orientations. For telescope aberrations which are not circularly symmetric, it is conceivable that there is an optimum orientation of the aberrations to maximize the image quality. Further, there is then an expected change of perceived image quality as the PSF (and associated MTF) are rotated.

It is assumed that for two images with equal feature sizes (same sized images in display), the image with the smallest visible feature is generally the image with greater usefulness. Naturally, there is more than limiting resolution that is considered in a judgment of image quality or usefulness, but in general, observers will compare blur levels in two images. At some level of blur, some features will lose enough contrast to become invisible, and this will lead to a rapid loss of perceived quality. This assumption also serves as justification for allowing images to remain the same size when optical magnification changes due to variation of object distance.

Similarly, it is assumed that if two images are not displayed with equal size, the relative usefulness of the two images cannot in general be determined. This assumption is based on the

fact that post launch analysis of images will include optional display magnifications. Therefore, the inherent visibility (or lack thereof) may change with increased magnification, changing the apparent usefulness of the imagery. To make an accurate judgment of the relative usefulness of two images would then require they be compared at some equal display size.

8.0 FOCAL LENGTH INVARIANT PERCEIVED IMAGE QUALITY

From the development in section 4.14.1 it is shown that the object space MTF is independent of focal length.

$$MTF_{obj}(u_x, u_y) = G\left(\frac{f \lambda u_x}{mD}, \frac{f \lambda u_y}{mD}\right) = G\left(\frac{R \lambda u_x}{D}, \frac{R \lambda u_y}{D}\right) \quad (8-1)$$

Also in section 4.14.1 it is shown that the CTF in object space is dependent on the magnification, and hence on the focal length.

$$CTF_{obj}(u_x, u_y) = CTF_{disp}\left(\frac{u_{disp\ x}}{mM}, \frac{u_{disp\ y}}{mM}\right) \quad (8-2)$$

Figure 45(a) illustrates the MTF and CTF curves for two different focal lengths and fixed display magnification (M). Equation (8-1) predicts identical MTF curves for the two focal lengths. However, since optical magnification (m) varies with focal length, Equation (8-2) predicts two different CTF curves result, yielding a difference in perceptual image quality for the two focal lengths.

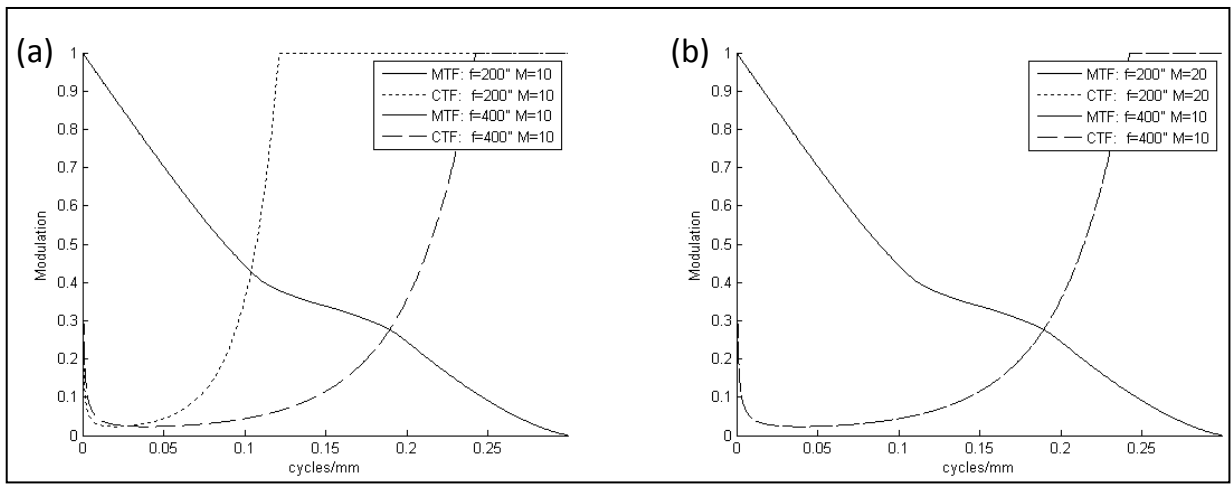


Figure 45. MTF curves for $f=200''$, and $f=400''$ are identical. (a) CTF curves vary for fixed display magnification (M). (b) CTF curves are identical when the display magnification (M) is varied in reciprocal proportion to the change in optical magnification (m).

As implied by Equation (8-2), if the display magnification (M) is varied in reciprocal proportion to the change in optical magnification (m), then the CTF becomes invariant under focal length changes, illustrated in Figure 45(b). This results in images of identical perceptual image quality.

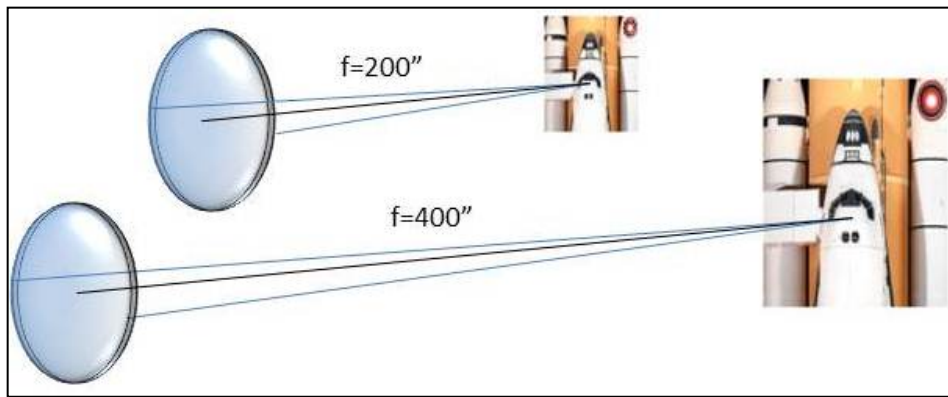


Figure 46. Although a shorter focal length yields a smaller PSF, the smaller resulting magnification creates a smaller geometrical image. The result is a PSF which is the same size relative to image features as for a larger focal length. The focal length then does not affect image content.

8.1 Perceptual Testing

In order to validate the focal length invariance of image quality, an experiment was conducted using a paired image comparison test technique. Images were simulated to vary in focal length with display magnification varying in inverse proportion to the optical magnification, yielding constant displayed image. All other parameters within each of the four data sets were held constant. Each data set contains five images, a reference and four test images. The reference image was simulated with a 50 inch focal length and the test images were simulated at focal lengths of 50 inches, 150 inches, 550 inches, and 1150 inches. The simulation parameters for each data set are shown in Table 12.

Table 12. Parameters used for simulating the four data sets used in paired image comparisons.

Data Set Label	Aperture Diameter [in.]	Object Distance [miles]	Obscuration Ratio	W_{040} [waves]
HQ house/fence	24	0.25	0.3	0
HQ trees	24	0.50	0.3	0
LQ trees	24	1.00	0.3	4.0
LQ house/shrub	5	0.50	0.3	0

The data set labeled as “HQ house/fence” is a high quality image with negligible blur introduced to the original image of Figure 40. The data set labeled “HQ trees” uses the base image of Figure 41 with very slight image degradation introduced. The data set labeled “LQ house/shrub” is a set of significantly blurred images using Figure 42, blurred using diffraction from a small aperture diameter. The final data set is labeled “LQ trees” and consists of a set of images with an

original image shown in Figure 40 and blurred significantly using a combination of longer object distance and the presence of a significant quantity of third order spherical aberration (W040) balanced with defocus.

The paired image comparison testing was conducted with 15 individuals each observer being presented with each image pair twice. Images were presented on a single laptop in a single environment, illuminated normally (with standard ceiling-mounted fluorescent lighting fixtures). Image pairs were presented at random, and the location (left or right side of the monitor) of the reference image was random, lowering the effect any non-uniformity of the display would have on the result. The observer was not able to continue before selecting an image from the pair by clicking the button corresponding to the image they considered to be “more useful”. Observers were allowed to adjust the monitor angle and their distance from the monitor to maximize their viewing comfort. Viewing distances varied, generally from 16 inches to 30 inches. Observers normally using corrective lenses for image information extraction were asked to use them during the perceptual testing. Total observation times were on the order of 12 minutes per observer with some variation. The assumption that trials and observers can be considered equivalent was applied.

Each observer was presented with a hard copy of the test instructions to follow along as the instructions were read to them. The instructions were as follows: “You will be presented with pairs of images—one on the left, and one on the right. For each pair of images, please provide your opinion of which image is more useful in terms of contained image information. Provide

your opinion by clicking the left button to indicate you believe the left image is more useful, or by clicking the right button to indicate the right image is more useful. You must choose an image as being more useful before you can continue to the next pair. There is no limit on time and there is a total of 36 pairs of images”.

8.2 Experimental Data

The data collected from the experiment described above are shown in Figure 47 through Figure 50. The associated error bars are calculated using the normal approximation to the binomial distribution for a 95% confidence interval unless otherwise noted. For data corresponding to a fractional selection of 0.50, there is no perceived difference between the test image (focal length of 50 inches) and the appropriate test image. The first data point in each set represents the reference image paired with itself. This provides a bit of an alternative error in the measurements. If the fractional selection between two identical images is not 0.50, then the difference between the actual fractional selection and the theoretical value of 0.50 provides a measure of the statistical uncertainty encountered.

The data of Figure 47 indicates that no perceived difference in quality occurred for the house/fence image with different focal lengths. This is the highest quality data set tested and validates the mathematically derived focal length invariance under the condition of very slight introduced blur.

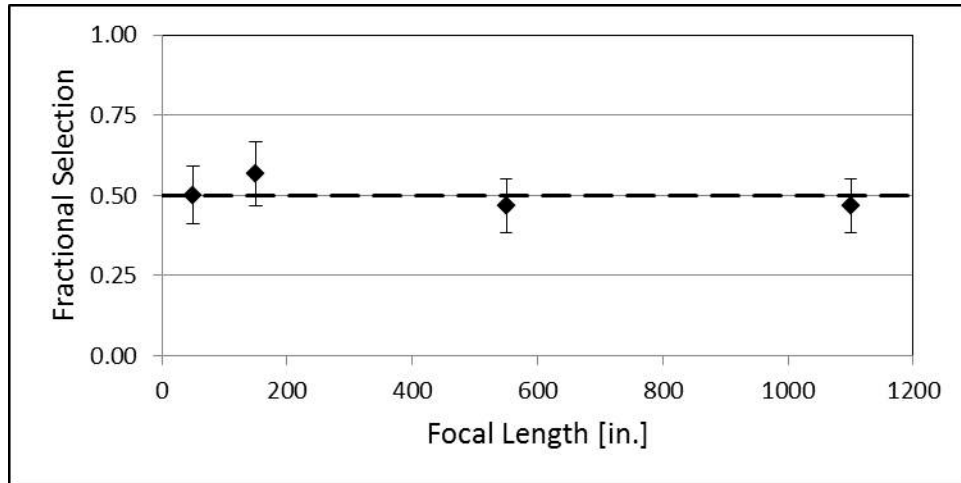


Figure 47. Fractional selection of the reference image as having higher usefulness for the HQ house/fence data set.

For an image of trees with slightly more but still very slight blur introduced, the data is shown in Figure 48. This provides mixed results of perceived differences between focal lengths as they varied. An image with focal length of 50 inches is not seen to have a difference in quality between itself or the same image with a focal length of 550 inches. However, images with focal lengths of 150 inches and 1150 inches were lower in quality than the reference 50 inch image. There is no pattern to the data results for this data set which could be used to extract the Just Noticeable Difference data indicating how much difference in focal length could be tolerated before a noticeable difference in quality can be observed.

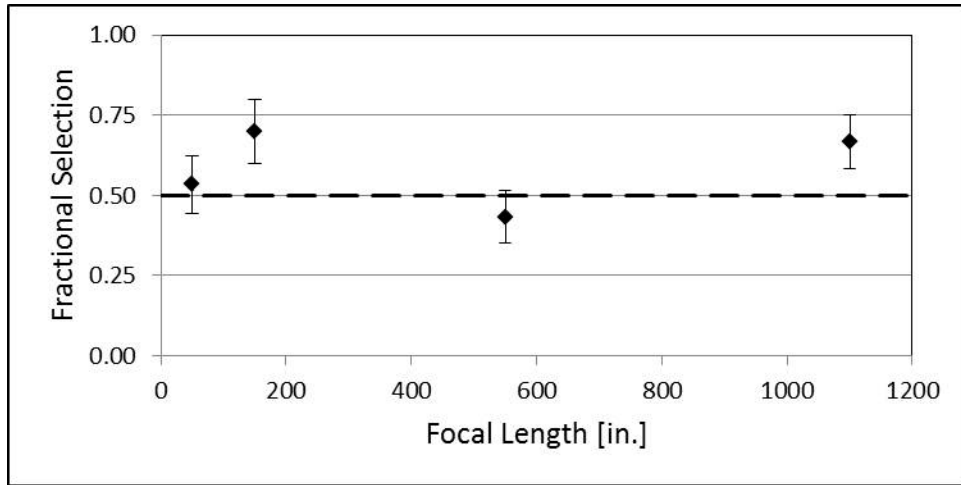


Figure 48. Fractional selection of the reference image as having higher usefulness for the HQ trees data set.

Considering now a case of an image with significant diffraction-induced blur, the associated errors are much higher. Here the fractional selection for the 50 inch focal length paired with itself had a value of 0.63, indicating an error of 0.13. This difference exceeded the errors derived from the 95% confidence interval and were therefore used instead. The resulting data then indicates no perceived quality difference between the reference image and test images of 50 inches, 150 inches, and 550 inches. The image simulated at a focal length of 1150 inches does not agree with the expected fractional selection of 0.50 and indicates a preference of the higher focal length image over the reference image. This is the opposite result of the previous data set.

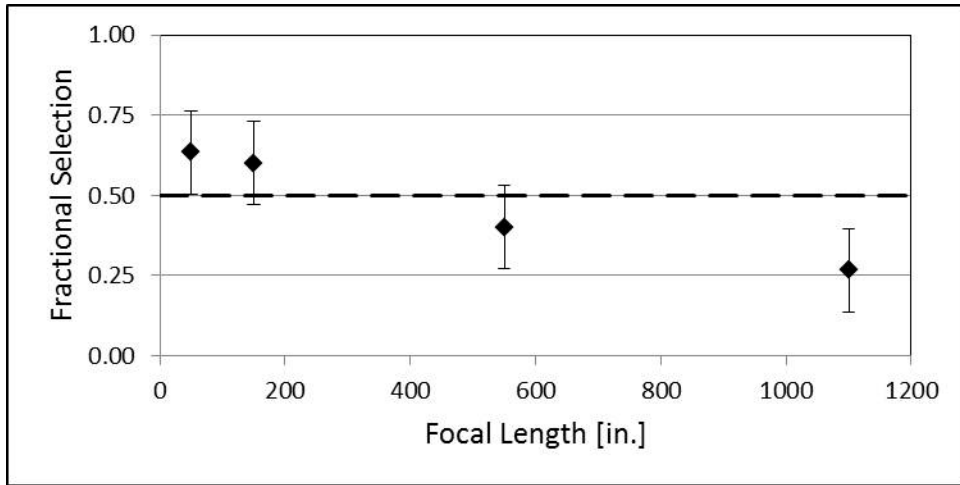


Figure 49. Fractional selection of the reference image as having higher usefulness for the LQ trees data set.

Finally, for a data set with significant aberration-induced blur (Figure 50), all images were considered by observers to be higher quality than the reference 50 inch focal length image, with the exception of the reference image compared to itself. This data set yields a pattern from which JND data could be extracted, estimated to be about 100 inches of focal length.

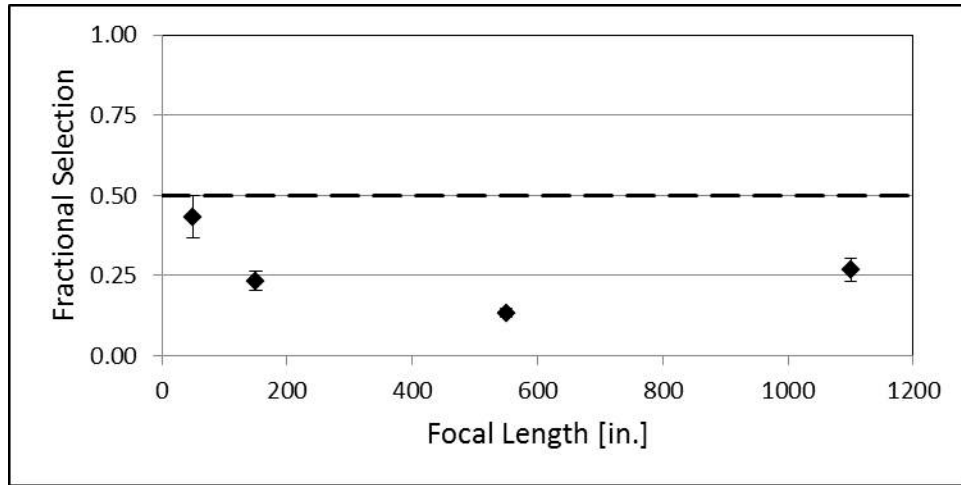


Figure 50. Fractional selection of the reference image as having higher usefulness for the LQ house/shrub data set.

8.3 Data Analysis

A summary of the data from the previous section with omission of the reference image paired with itself is provided in Table 13.

Table 13. Summary of the results of data presented in the previous section.

Focal Length	House/Fence High Quality	Trees High Quality	Trees Low Quality	House/Shrub Low Quality
150 in.	No Preference	50 in. Preferred	No Preference	150 in. Preferred
550 in.	No Preference	No Preference	No Preference	550 in. Preferred
1150 in.	No Preference	50 in. Preferred	1150 in. Preferred	1150 in. Preferred

Consider one focal length (row) at a time. For a focal length of 150 inches, a case of high quality and a case of low quality yielded no observer preference to the focal length of 50 inches.

Additionally, one high quality image and one low quality image yielded opposite preferences, the high quality trees image favoring the shorter focal length and the low quality house/shrub image favoring the longer focal length.

For a focal length of 550 inches, no preference is found for the two high quality images or the low quality trees image, but preference is given to the longer focal length image of the house/shrub.

For a focal length of 1150 inches, one high quality image (house/fence) yields no preference. The remaining three images (one high quality and two low quality images) yield mixed preference, the high quality image favoring the shorter focal length and the two low quality images favoring the longer focal lengths.

The lack of pattern of image preference in the first three data sets indicates statistical fluctuation around the 0.50 fractional selection line. This result supports that image quality is invariant under changes in focal length for imagery displayed at a constant size. The final data set does not support the invariance, but the reason is suspected to be a combination of two factors. The first is the obvious statistical nature, which although 30 trials (15 observers with two trials each) were taken, this may be insufficient to prove the desired result. The second factor is the interpolation processes used in image simulation. Since the Point Spread Function increases in size as the focal length increases and the geometrically scaled object simultaneously experiences a change in magnification, both are exposed to interpolation processes. Although the ratio is

maintained, both the PSF and the geometrical image scales are changed. The resulting interpolation of the PSF to the scale of the geometrical image then has numerical variation which can potentially introduce small variations in image quality. For very high quality imagery where the PSF is approximately the size of an image pixel, this small change would be harder to notice than for a case where the PSF is significantly larger than an image pixel, such as in the last two data sets.

It is then concluded that for high quality imagery, perceived image quality is invariant under changes in focal length if the displayed image size remains constant. For low quality imagery, the invariance of image quality will be highly dependent on interpolation accuracy if simulated imagery is used. Note that if real imagery is used in an attempt to validate the invariance, very high resolution detectors must be used over a fairly limited range of display magnifications, effectively limiting the range of focal lengths that could be verified as invariant. Further, the process of increasing the display magnification applies an interpolation process, which will likely interfere with results. Thus, it would be very difficult to validate the image quality invariance using real imagery.

9.0 THRESHOLDS FOR CHANGES IN APERTURE DIAMETER

A single model is desired which can allow the imaging performance capacity ranking of LVIT. To achieve this, the metric values for quality category (Excellent, Good, Fair, etc.) boundaries are necessary. These can be acquired by two means: (1) Perform perceptual testing for each telescope, limiting the model to only telescopes which are currently in service, or (2) Perform perceptual testing over a sizable range of telescope aperture diameters including the values corresponding to the actual LVIT in service. Because of the few aperture sizes for LVIT, interpolation or extrapolation from these limited data points (there would be only three data points) would not be very accurate. The second approach allows for better aperture spacing so that a more generic and extendable model with greater applicability results. The resulting model is then able to function if new telescopes are employed, of different diameter than those currently in service, without the need to conduct new perceptual testing and updating of the model. The second approach is the more logical one for this application and was applied, with perceptual testing details and results provided in the next section.

9.1 Perceptual Testing

Perceptual testing for the aperture diameter parametric variation included the synthesis of 70 images of the Space Shuttle Atlantis on the pad, shown in Figure 39, at a constant range of 15 miles. The images varied in simulated aperture diameter from 7 inches, to 30 inches, including the three aperture diameters of LVIT on the Eastern Range, namely 9 inches, 18 inches, and 24 inches. Approximately 8 images were generated for each aperture diameter, the 8 image

sequence varying in magnitude of third order spherical aberration balanced with defocus. Categorical Sort testing was conducted with 6 individuals familiar with both the TIME Tool and LVIT imagery, each observer being presented with each image twice. Images were presented on a single laptop in a single environment, illuminated normally (with standard ceiling-mounted fluorescent lighting fixtures). Images were presented at random, not allowing the observer to continue before “rating” the current image by clicking the button corresponding to the appropriate descriptor (Excellent, Good, Fair, etc.). Observers were allowed to adjust the monitor angle and their distance from the monitor to maximize their viewing comfort. Viewing distances ranged from 16 inches to 30 inches, generally dependent on the age of the observer. Observers normally using corrective lenses for image information extraction were asked to use them during the perceptual testing. Total observation times were on the order of 12 minutes per observer with some variation.

Perceptual test data was analyzed using Class II, Condition B outlined by Torgerson [71] and Engeldrum [70]. Further, the assumption that trials and observers can be considered equivalent was applied. Analysis was performed using the SQRI, the SQRI normalized to the diffraction limit (henceforth referred to as SQRI_{norm}), the TTP base metric, the TTP base metric normalized to the diffraction limit (henceforth referred to as TTP_{norm}), and the SQF.

9.2 Experimental Data

Results of the normalized analyses are shown in Figure 51 and Figure 52. The results of the perceptual test analyses are presented first as normalized metrics, then as a non-normalized metrics.

The SQRI_{norm} boundary curves of Figure 51 make sense intuitively in that higher aberration magnitudes are tolerable for larger aperture diameters. The SQRI asymptotes also make sense as a true zero value of the metric requires extreme levels of aberration (a result stemming from the MTF normalization to unity at zero spatial frequency). Further, it becomes increasingly difficult to achieve high quality imagery for smaller apertures due to diffraction limitations. Note that an SQRI_{norm} value of 100 corresponds to the diffraction limit, indicating that for diameters below approximately 17 inches, excellent quality imagery can never be obtained at this object distance. Also note that this figure is valid only for the object distance of 15 miles, but the curve forms are assumed independent of object distance, and thus, an appropriate scaling (vertical shift) of the values makes the figure valid for other ranges. For longer object ranges, the curves would shift upward, making a given image quality more difficult to obtain. Similarly, a closer object range shifts the curves downward, indicating higher tolerable aberrations for a given image quality category.

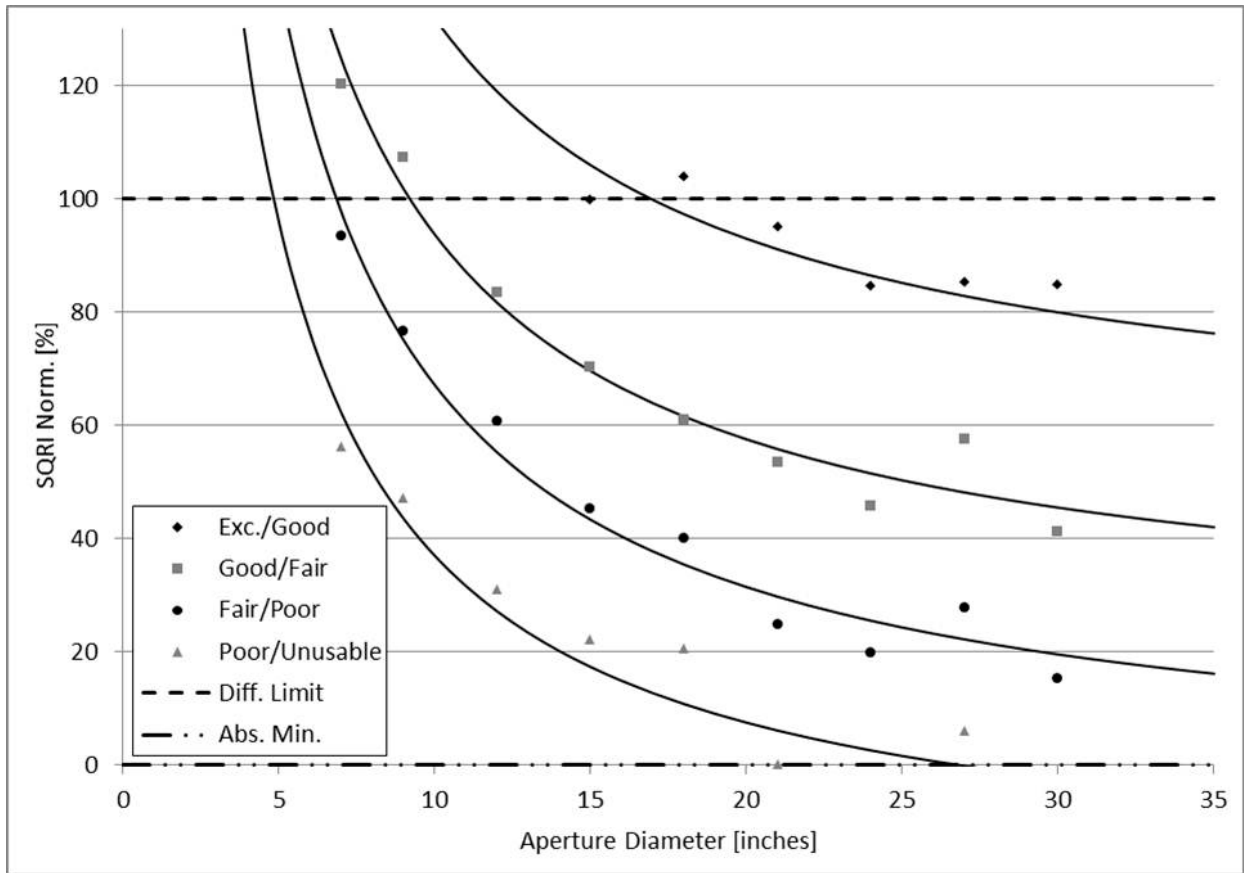


Figure 51. Normalized SQR I (SQR I norm) boundary values resulting from categorical sort testing for aperture diameter trends. Solid curves are inversely proportional to the aperture diameter with excellent R^2 values.

Although the SQRInorm boundary curves are intuitive, the TTPnorm boundary curves of Figure 52 for aperture diameter variation are less intuitive. The linear curves resulting from the analysis seem to indicate that lower quality images will no longer exist as higher aperture diameters are encountered. This is concluded from the horizontal axis crossings of the curves and is clearly not the case encountered in reality since badly aberrated optics will create bad imagery regardless of the size of the aperture. This apparent inaccuracy of the TTPnorm curves is discussed further in the next section.

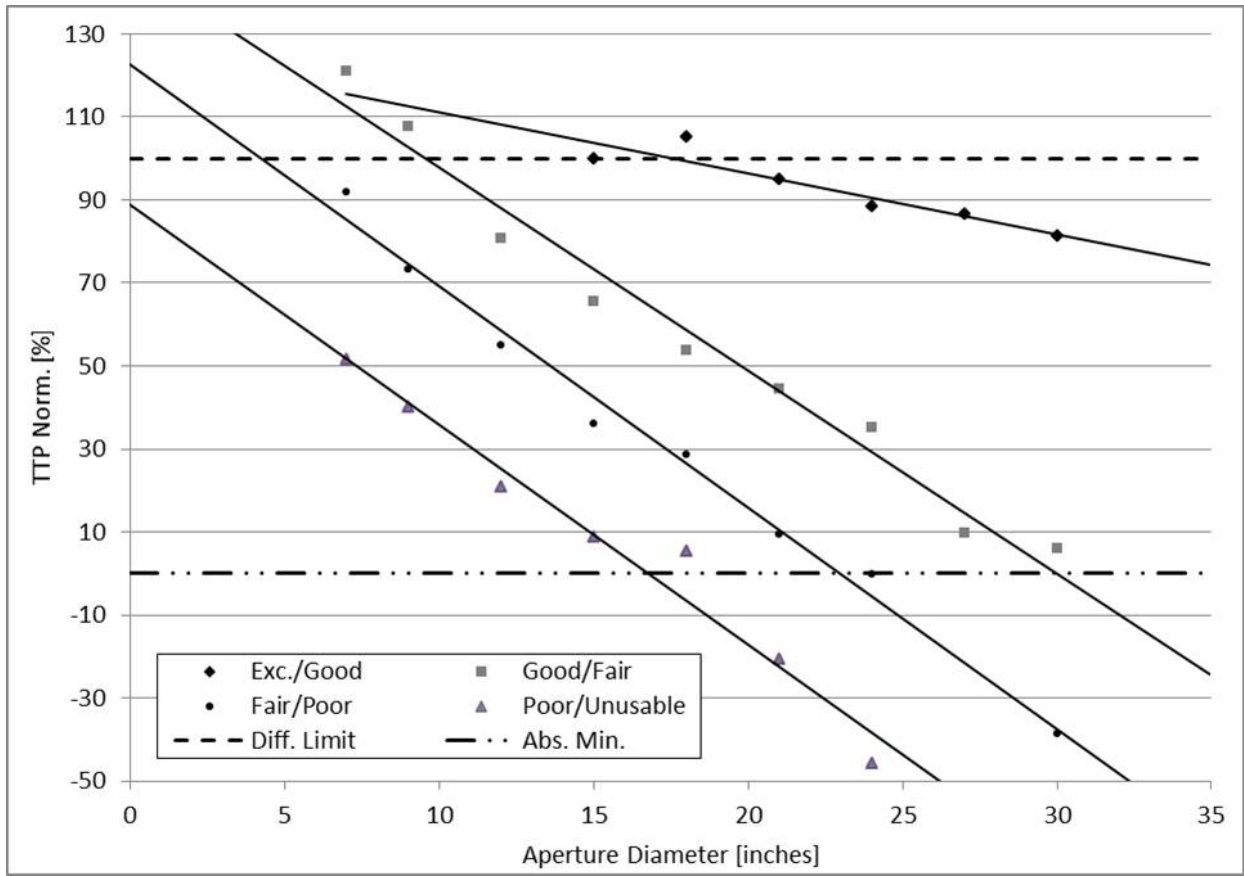


Figure 52. Normalized TTP (TTP norm) boundary values resulting from categorical sort testing for aperture diameter trends. Solid curves are proportional to the aperture diameter with excellent R^2 values.

Considering now the non-normalized SQRI image quality boundary curves (Figure 53), entirely different functional forms occur. The boundary curves appear to asymptotically approach the diffraction limit as the aperture diameter decreases, with boundaries becoming more closely spaced. This is consistent with the normalized SQRI curves of Figure 51 which asymptotically approach a vertical line at lower apertures with the inverse diameter curves becoming closer to each other.

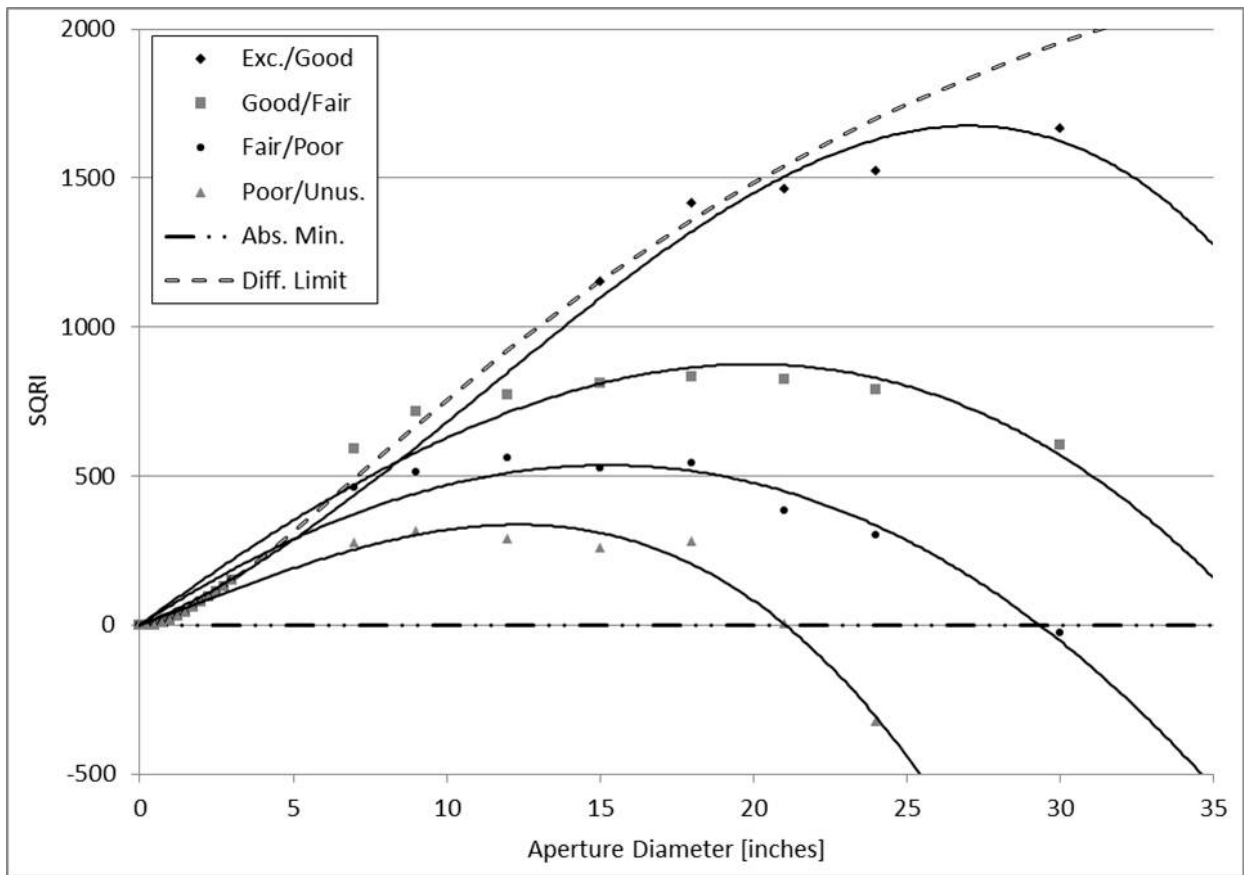


Figure 53. SQRI boundary values resulting from categorical sort testing for aperture diameter trends. Solid curves are cubic with excellent R^2 values.

In the non-normalized case, the curves are cubic in form, and curves of such form have been fit to the data and displayed in Figure 53. Since the SQRI should be zero for a diameter of zero, an intercept of zero was forced in the fitting process. This causes fitted curves to fall significantly below zero and then rebound to the zero intercept (approaching zero diameter from higher values). To prevent this, artificial data was inserted at the diffraction level of the SQRI for diameters from 0 inches to 3 inches. This helps weight the curves to fall on the diffraction curve as they should for very small apertures. The resulting coefficients of determination (R^2) are very high (Table 14), indicating that the selected curve forms fit the data well.

Table 14. Coefficients of cubic curves fit to the SQRI data shown in Figure 53.

	Cubic Coef.	Quad. Coef.	Lin. Coef.	Constant	R ²
E/G	-0.1142	3.874	40.751	0.000	0.9957
G/F	-0.0286	-1.049	76.176	0.000	0.9631
F/P	-0.0129	-1.922	67.458	0.000	0.9496
P/U	-0.1044	0.345	38.919	0.000	0.9620

As was the case for the TTPnorm curves, the SQRI quality boundaries intercept the horizontal axis, apparently indicating that lower quality imagery can be eliminated by using larger diameter telescopes. This phenomenon will be discussed in the next section.

For the case of non-normalized TTP quality boundary curves, the same behavior is observed as in the case of the non-normalized SQRI, namely that the curves asymptotically approach the diffraction limit at lower diameters, and appear to be cubic in form. Further, apparent image quality category extinction occurs for the TTP, which is discussed in the next section. As with the SQRI, diffraction-limited values were introduced at aperture diameters of 0 inches to 3 inches to prevent the data fitting curves from crossing zero and then rebounding to the required intercept. Again, the resulting coefficients of determination (R²) are very high (Table 15), indicating that the selected curve forms fit the data well.

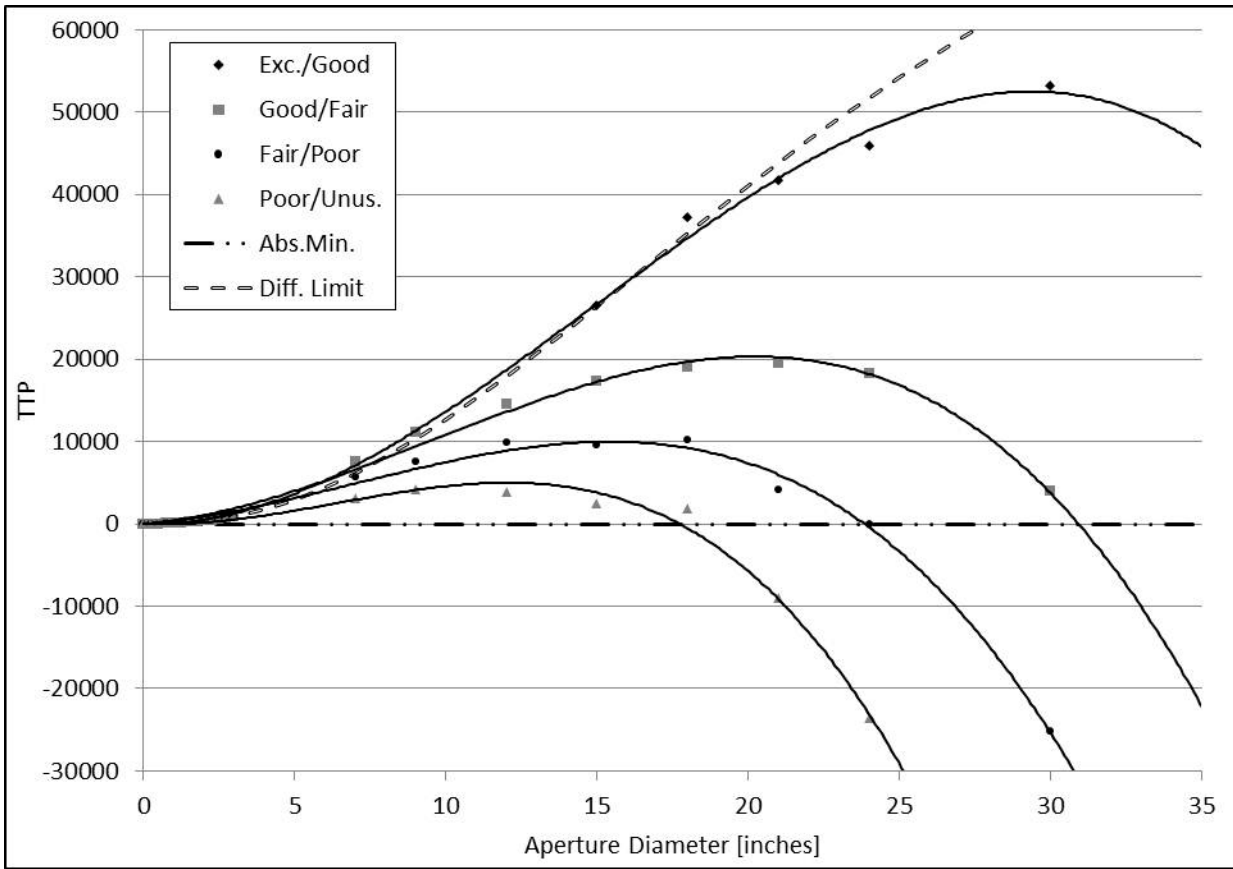


Figure 54. TTP boundary values resulting from categorical sort testing for aperture diameter trends. Solid curves are quadratic with excellent R² values.

Table 15. Coefficients of cubic curves fit to the TTP data shown in Figure 54.

	Cubic Coef.	Quad. Coef.	Lin. Coef.	Constant	R ²
E/G	-4.27	189.810	-103.420	0.000	0.9983
G/F	-4.1355	117.590	318.030	0.000	0.9906
F/P	-4.1721	87.023	296.890	0.000	0.9905
P/U	-6.755	128.180	-148.540	0.000	0.9851

As with the TTP and SQRI, the SQF curves calculated from the categorical test results (Figure 55) are cubic in form. The lower three boundary curves have excellent R^2 fit values, indicating that the curves fit the data well (Table 16). The boundary separating Excellent quality and Good quality however, has a negative R^2 value, indicating the curve is not a good model for the data. Since the lower boundaries all indicate a cubic form is best suited for the data, and since the Excellent/Good boundary data visually fits the cubic form well, it is hypothesized that the Excellent/Good boundary should also follow the general cubic form as displayed.

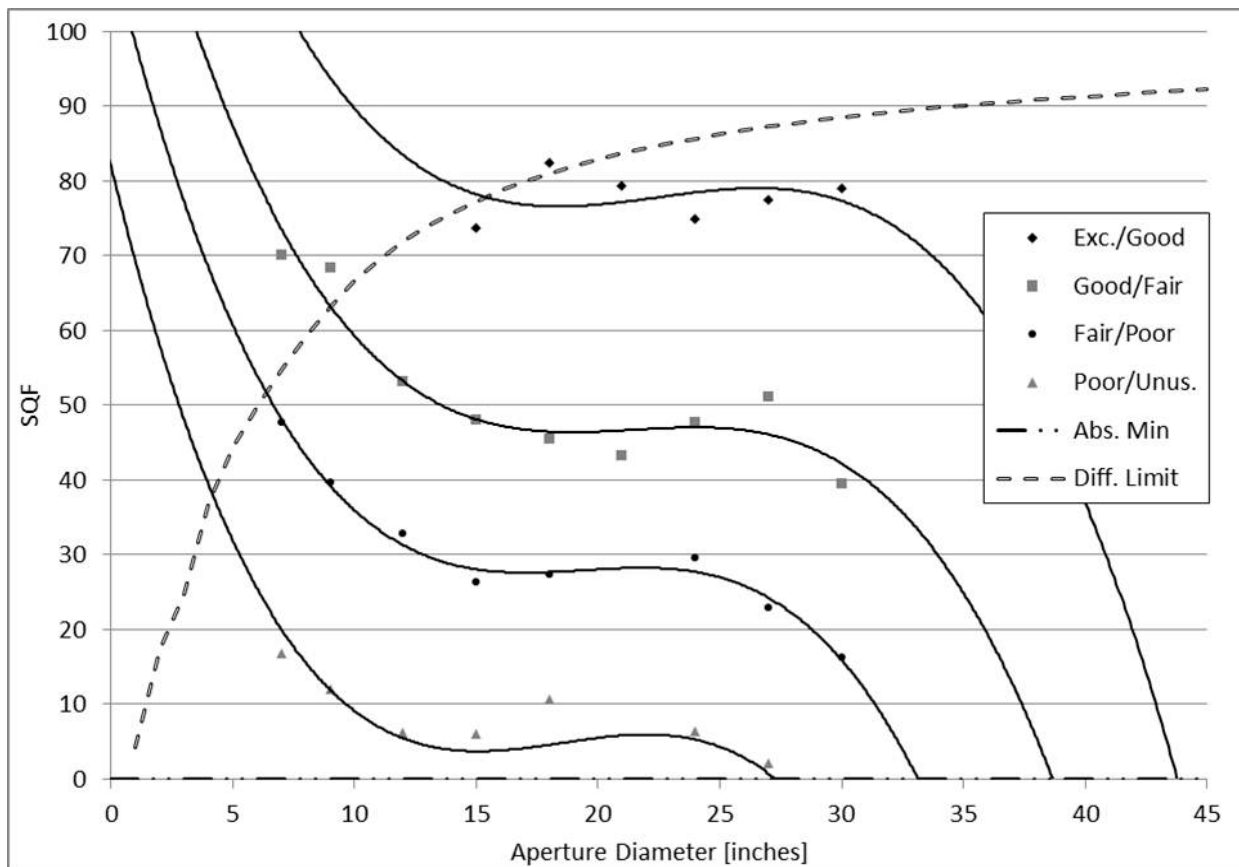


Figure 55. SQF boundaries resulting from categorical sort testing for aperture diameter trends. Solid curves are cubic curves with excellent R^2 values.

Table 16. Coefficients of quartic curves fit to the SQF data shown in Figure 55.

	Cubic Coef.	Quad. Coef.	Lin. Coef.	Constant	R ²
E/G	-0.009	0.6078	-13.206	170.00	-0.5190
G/F	-0.0098	0.6309	-13.345	139.43	0.9089
F/P	-0.0119	0.6929	-13.246	111.00	0.9828
P/U	-0.0135	0.7528	-13.464	82.00	0.4853

Remembering that the SQF is a normalized quantity (normalized to an ideal condition, not to the diffraction limit), the absolute minimum value of SQF is 0. Considering then the curves shown in Figure 55, according to the SQF metric, it would be difficult for an imaging system to exist in poor enough condition to yield Unusable quality imagery for aperture diameters between 12 inches and 27 inches, and impossible for an imaging system to yield unusable imagery for systems with aperture diameters greater than 27 inches. Similarly, noting the zero crossings of the boundary curves, the SQF appears to indicate that simply by making an aperture large enough, lower quality imagery can be made extinct, regardless of the quality of the system components. This is the same phenomenon present in all of the metrics presented here except the normalized SQRI which asymptotically approaches the zero values for all but the lowest boundary curve. This phenomenon is further discussed in the next section.

9.3 Data Analysis

As seen in the previous section, essentially five metrics were analyzed for image quality boundaries: SQRI, SQRInorm, TTP, TTPnorm, and SQF. These yielded several significantly different plots, even though the same set of image rankings was used for the analysis of all. The cause of the difference in curve types is worth some attention, and to summarize, a list of the metrics and the resulting curve types are listed below.

Table 17. Summary of boundary forms for each of the metrics investigated.

Metric	Definition	Boundary Form
TTP	$TTP = \int_0^{f_{max}} \sqrt{\frac{C_{TGT} MTF}{CTF}} df$	Cubic
TTPnorm	$TTP_{norm} = \frac{\int_0^{f_{max}} \sqrt{\frac{MTF}{CTF}} df}{\int_0^{f_{max}} \sqrt{\frac{MTF_{diff}}{CTF}} df}$	Linear
SQRI	$SQRI = \frac{1}{\ln(2)} \int_0^{f_{max}} \sqrt{\frac{MTF}{CTF}} \frac{df}{f}$	Cubic
SQRInorm	$SQRInorm = \frac{\int_0^{f_{max}} \sqrt{\frac{MTF}{CTF}} \frac{df}{f}}{\int_0^{f_{max}} \sqrt{\frac{MTF_{diff}}{CTF}} \frac{df}{f}}$	Inverse Square
SQF	$SQF = \int_{10}^{40} \int_0^{2\pi} MTF(f, \theta) d\theta d \log(f)$	Quartic

To address the apparent termination of image quality categories as aperture diameter increases for all but the SQRI_{norm}, requires a discussion of the metric frequency weighting mechanisms. Summarized in Table 18 are the spatial frequency weighting mechanisms for the TTP, SQRI, and SQF. Naturally, the normalized forms of the TTP and SQRI have the same weighting mechanisms as the metrics they are derived from. Both the TTP and SQRI include a CTF weighted spatial frequency, although one could consider the SQF to also have a CTF weighting present—it is simply a bandpass CTF rather than a continuous CTF.

Table 18. Summary of spatial frequency weighting for the metrics of interest.

Metric	MTF spatial frequency weighting mechanism	Minimum weighted spatial frequencies	Maximum weighted spatial frequencies
TTP	CTF weighted frequencies	High and very low spatial frequencies	Mid spatial frequencies
SQRI	CTF weighted frequencies with additional 1/f weighting	Mid-to-high and very low spatial frequencies	Low-to-mid spatial frequencies
SQF	1/f frequency weighting	Highest in-band spatial frequencies	Lowest in-band frequencies

Now considering the integrated weight of spatial frequencies, the TTP treats all frequencies as equally contributing to perceived image quality. The SQRI on the other hand, has an inverse weighting on frequencies such that lower frequencies are considered to contribute more to perceived image quality. The SQF also provides for higher contributions from lower spatial frequencies with an inverse frequency weighting. For conditions where enough display magnification is present such that the CTF cutoff frequency is similar to that of the optics (a

reasonable approximation for the purpose of this argument), the spatial frequencies with the highest weights for each metric can be qualitatively established. For the TTP, the highest weighted spatial frequencies are the mid spatial frequencies, corresponding to the minimum in the CTF curve. The SQRI has highest weighted frequencies occurring at the low-to-mid spatial frequencies, above the spatial frequencies corresponding to peak CTF values, and below spatial frequencies that quickly lower the weighting from the inverse frequency weight. The SQF is essentially band-limited (to approximate the CTF) and weighted inversely with spatial frequency, making the highest weight spatial frequencies the lowest which occur in band. The weighting mechanisms and minimum/maximum weighted spatial frequencies are summarized in Table 18 and illustrated in Figure 56.

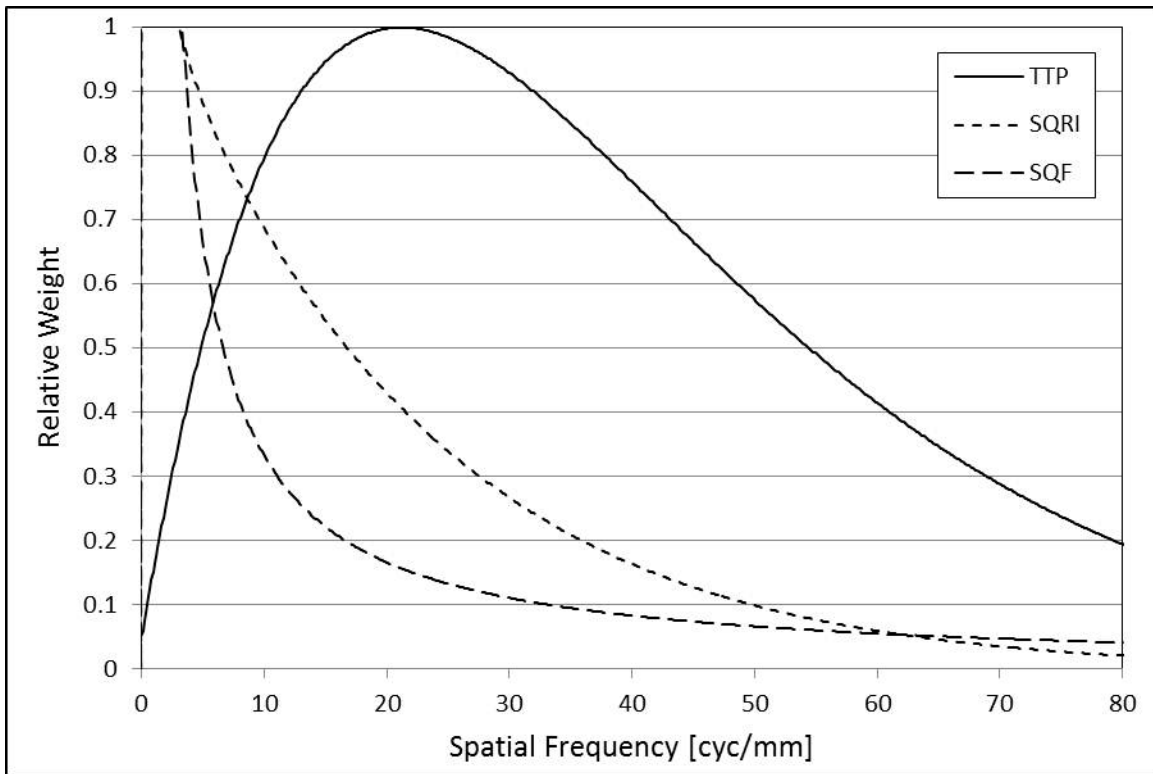


Figure 56. Relative spatial frequency weighting functions for the SQRI, TTP, and SQF.

To fully address the phenomenon of the metric trends indicating that lower categories of image quality become extinct in a methodical fashion as aperture diameter increases requires answering three questions:

1. Would this phenomenon be observed in reality with large aperture telescopes?
2. What causes the apparent extinction of image quality categories in all but the SQRI_{norm}?
3. Why is the SQRI_{norm} different in that boundary termination does not occur in general?

The first question can be answered simply by considering a case with a very large amount of defocus present. Although it violates the assumption that was made concerning the telescope operator's ability to remove defocus, it is the simplest case to illustrate with. If the detector is located well behind the optimal image plane (on the order of several inches), a very bad image will result regardless of the aperture size. Thus, it is theoretically possible to introduce enough optical distortions (generally through misalignments) to degrade the image adequately to compensate for the improvement resulting from a large diameter. This is of course not what is predicted by the curves above. The metric prediction of terminating image quality categories is then inaccurate.

The second question is answered by considering the data analysis process. When the raw data is processed, arbitrary scale values are assigned to the observer opinions, and boundary values are determined relative to the established scale values. In most cases, the boundary values do not coincide with a particular image that was generated. To overcome this problem, the image quality metrics are plotted against the scale values and a line is fit to the data. This line is used to

interpolate or extrapolate as necessary to determine the corresponding metric value associated with a boundary. Since the presence of very large aberrations tends to cause the metric values to lose correlation to observer opinions of the corresponding image quality, images were not used that contained more than a moderate level of aberration. Thus, for larger aperture sizes that can tolerate aberrations more easily, extrapolation is almost always necessary. The extrapolation process is completely independent of the metric function and does not account for the non-negativity constraint of the metrics considered. The result is that predicted metric values that correspond to negative metric values occur, along with the accompanying apparent termination of image quality categories.

A more valid form of the data would allow the same general form of the curves, but rather than crossing the horizontal axis and becoming negative, they would instead become asymptotic to it. This is discussed and illustrated in the next section.

Finally, the SQRI_{norm} will be addressed. This metric is different from the SQRI, TTP, TTP_{norm}, and SQF in the fact that its quality boundary curves do not become extinct (except in the case of the lowest boundary which has the poorest R^2 value). The difference stems from a combination of the normalization and the spatial frequency weighting. In the SQRI, low-to-mid spatial frequencies (relative to the human visual cutoff frequency) are highest weighted, quickly decreasing the metric as aberrations increase. The SQRI spatial frequency weighting function is shown in Figure 57 as the bold dashed line. Note that this weighting function is not on the same scale as the MTF plots.

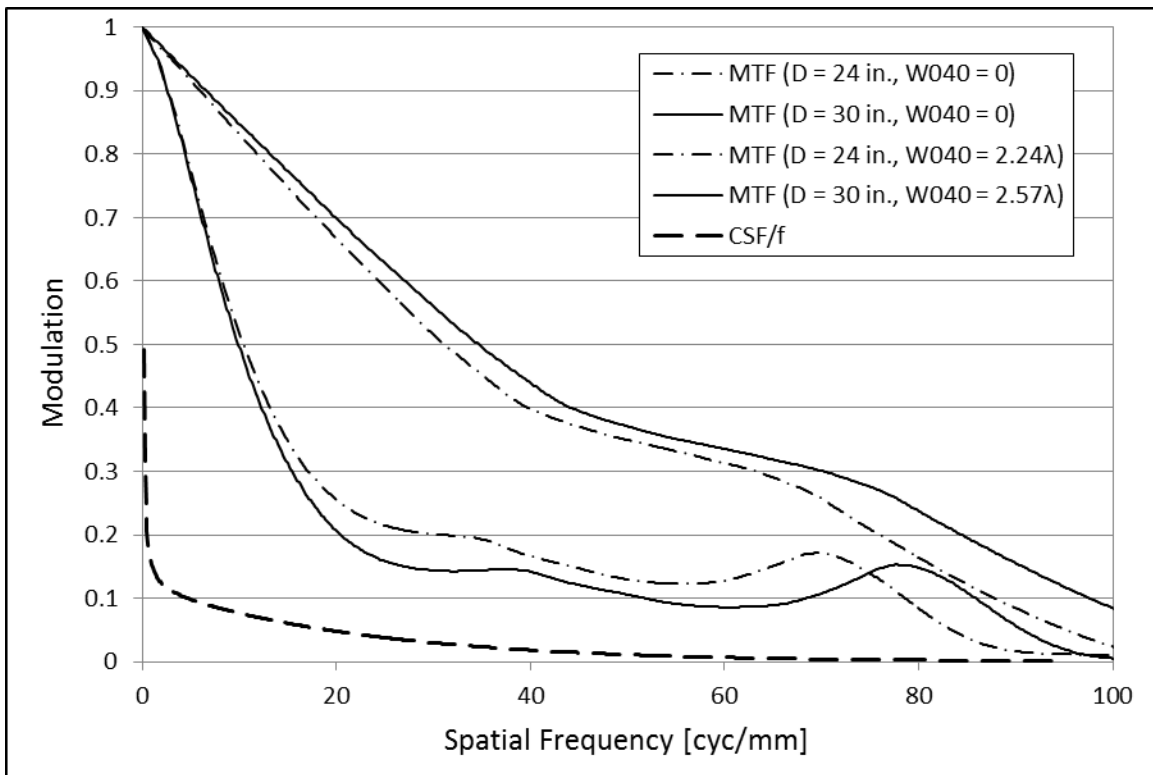


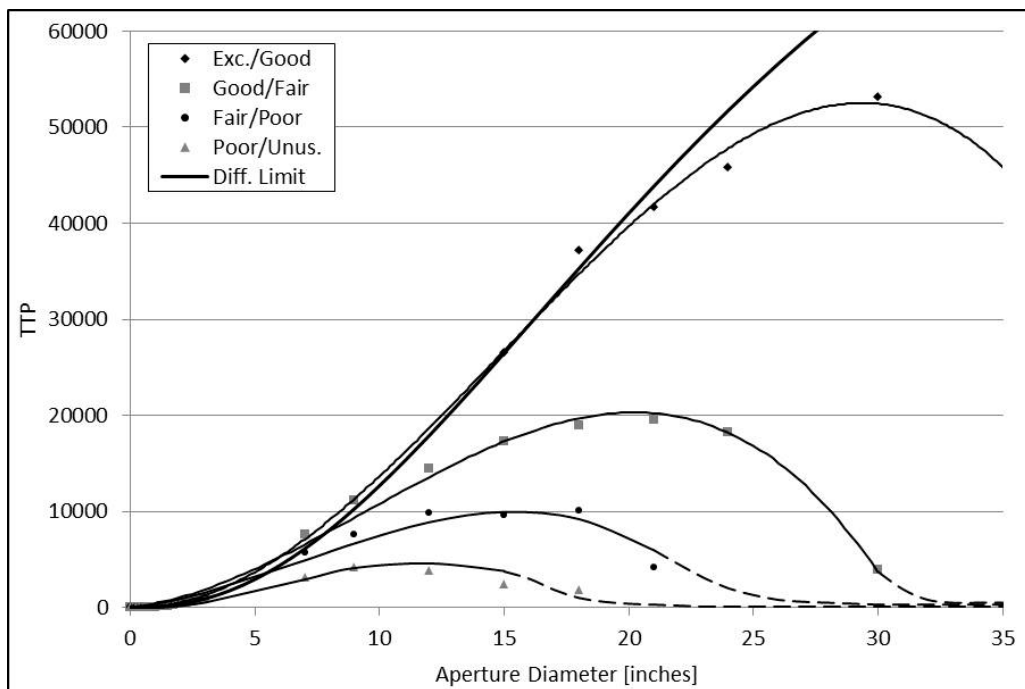
Figure 57. MTF curves for 24 inch and 30 inch diameter telescopes at diffraction limit, and in the presence of aberrations. Also shown is the SQRI spatial frequency weighting function (bold dashed curve).

Consider now that the low spatial frequencies of MTF curves are relatively constant as a result of normalization to unity at the zero frequency point. This phenomenon occurs for diffraction limited MTF curves as well as MTF curves in the presence of aberrations and is illustrated in Figure 57. Furthermore, as the diameter increases (into the region in which the boundary curves become asymptotic to a horizontal line), the MTF scales to larger frequencies, causing its own slowly varying spatial frequencies to correspond to the low-to-mid-spatial frequencies of the human visual system. This yields slowly varying MTF values to be highest weighted in the numerator of the metric, yielding a slow decrease of the numerator as aberrations increase. As

the diameter increases, the denominator increases, but at a decreasing rate due to the frequency weighting function. Thus, in the case of a normalized SQRI, as diameter increases, the numerator slowly decreases and the denominator increases at a decreasing rate, causing the apparent asymptotic nature observed.

9.4 Threshold Adjustments

As indicated previously, the boundary curves for the TTP, TTPnorm, and SQRI are expected to become asymptotic to the horizontal axis rather than crossing it. For the sake of completeness, the previous boundary curves are shown in the figures below with the expected behaviors artificially included. Note that the solid lines are derived from data and the dashed lines are theoretical extrapolations based on the expected behavior.



Figure

58. TTP boundary curves (solid lines) modified to asymptotically approach the horizontal axis (dashed segments).

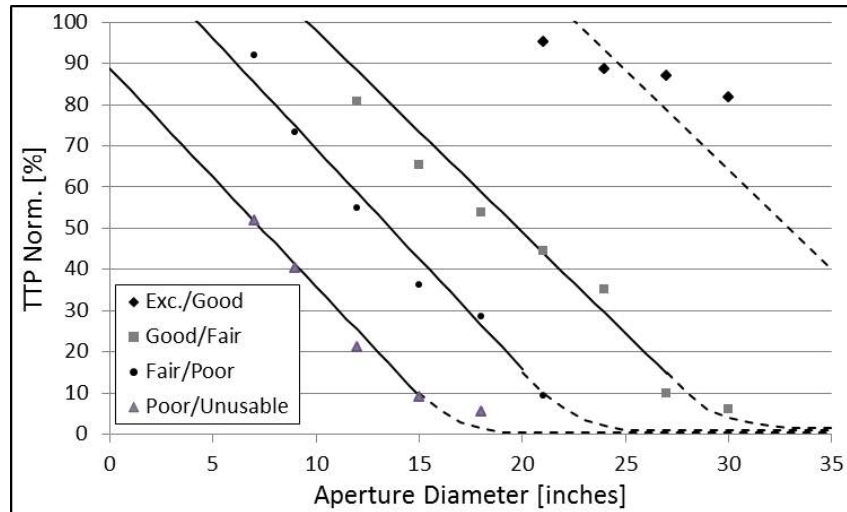


Figure 59. TTPnorm boundary curves (solid lines) modified to reflect the expected asymptotic behavior in as the boundaries approach the horizontal axis (dashed segments).

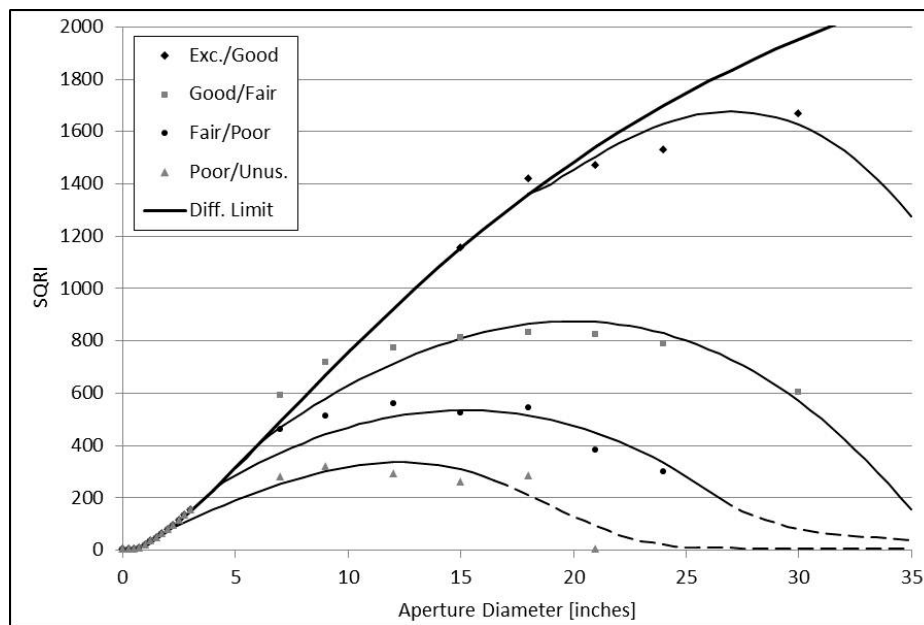


Figure 60. SQRI boundary curves (solid lines) modified to asymptotically approach the horizontal axis (dashed segments).

Note that since the SQF is not of particular interest, the expected form of the SQF boundaries is not included.

10.0 THRESHOLDS FOR CHANGES IN OBJECT RANGE

The image quality boundaries established in the previous chapter are valid for a single object distance. To increase the utility of the model requires knowledge of how the quality boundary curves scale with object distance.

10.1 Perceptual Testing

Perceptual testing for the object distance parametric variation included the synthesis of 40 images of the Space Shuttle Atlantis on the pad, shown in Figure 39, with a constant aperture diameter of 24 inches. The images varied in object distance from 15 miles, to 45 miles. For each range, 5 images were generated, the 5 image sequence varying in magnitude of third order spherical aberration balanced with defocus. Categorical Sort testing was conducted with 6 individuals familiar with both the TIME Tool and the entire image set was presented to each observer twice.

10.2 Experimental Data

Results of the analysis for this data set are shown in Figure 61 through Figure 63. The data appears at a glance to be linear in nature for the TTPnorm, SQRInorm, and SQF, and indeed,

plotting linear curves to the data seems to support such a conclusion. The high coefficients of determination shown in Table 19 through Table 21 are provided to quantify this conclusion.

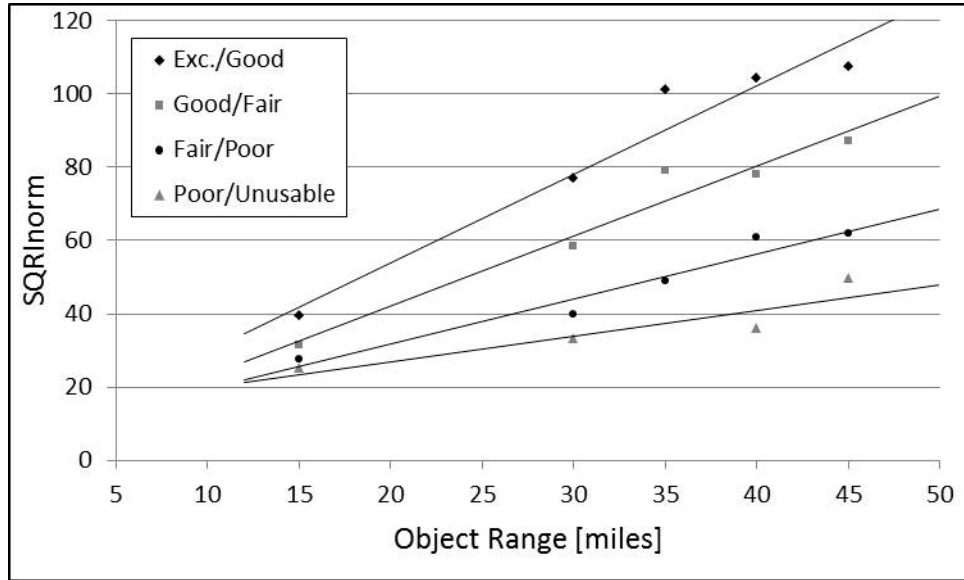


Figure 61. SQRInorm boundary values resulting from categorical sort testing for object range trends. The data appears linear and is fitted with lines.

Table 19. SQRInorm slopes and constants resulting from the data fitting shown in Figure 61 with resulting coefficients of determination listed.

	Lin. Coef.	Constant	R ²
E/G	2.4202	5.7021	0.9466
G/F	1.9101	3.8075	0.9558
F/P	1.2309	7.1386	0.9475
P/U	0.7059	12.636	0.8265

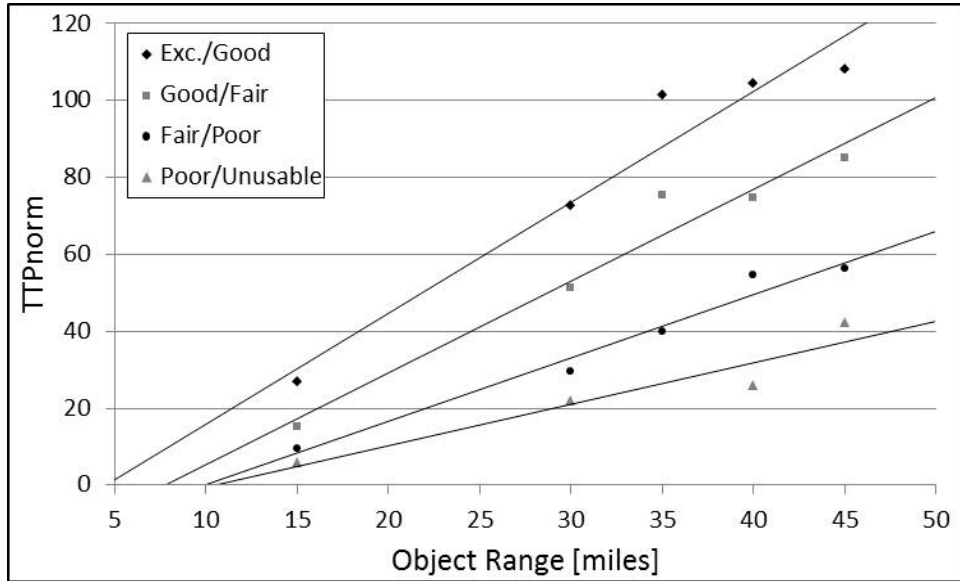


Figure 62. TTP boundary values resulting from categorical sort testing for object range trends appears linear and is fitted with lines.

Table 20. TTPnorm slopes and constants resulting from the data fitting shown in Figure 62 with resulting coefficients of determination listed.

	Lin. Coef.	Constant	R ²
E/G	2.8877	-12.858	0.9409
G/F	2.3859	-18.433	0.9563
F/P	1.6502	-16.489	0.9711
P/U	1.0791	-11.464	0.9079

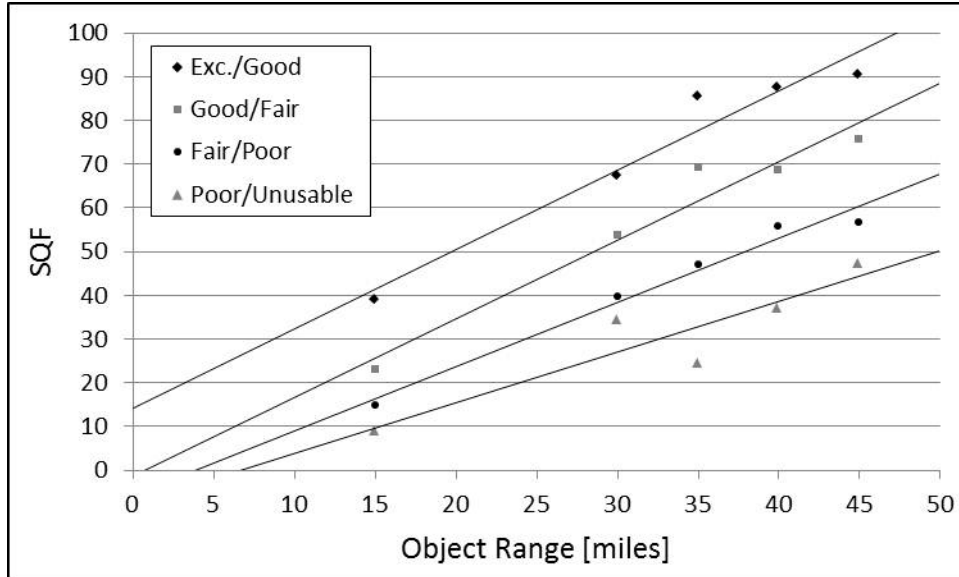


Figure 63. SQF boundary values resulting from categorical sort testing for object range trends appears linear and is fitted with lines.

Table 21. SQF slopes and constants resulting from the data fitting shown in Figure 63 with resulting coefficients of determination listed.

	Lin. Coef.	Constant	R ²
E/G	1.8173	14.095	0.9485
G/F	1.7926	-1.1225	0.9517
F/P	1.4651	-5.5775	0.9777
P/U	1.1555	-7.7008	0.8408

It is important to note that since the simulated image size is kept constant, the CTF is constant, then the normalized metrics differ from the non-normalized forms by only a multiplicative constant. To avoid the redundancy, the non-normalized forms are not shown.

10.3 Data Analysis

In the previous section, linear fits were provided based on the apparent linearity and supporting high values of corresponding coefficients of determination. However, in order to properly fit the data to curves, one must consider what type of curves should be fit to the data, not just what looks good. This can be determined from the boundaries established for the diameter variations of the previous chapter and by considering Equation (10-1) first introduced in Chapter 4.

$$MTF_{obj}(u_x, u_y) = G\left(\frac{f \lambda u_x}{m D}, \frac{f \lambda u_y}{m D}\right) = G\left(\frac{R \lambda u_x}{D}, \frac{R \lambda u_y}{D}\right) \quad (10-1)$$

From this, it can be seen that both the object distance (R) and aperture diameter (D) scale the MTF, a consequence of the similarity theorem. The range and diameter act as inverses of each other, and a doubling of the range can be considered equivalent to a halving of the aperture diameter. Considering the diameter variation data from the previous chapter was obtained at a constant range of 15 miles, the ratio of R/D can be calculated for each data point (Table 22). From this constant, the corresponding values of range for a constant aperture diameter of 24 inches can be determined, the results of which are shown in Table 22 (right column).

Table 22. Diameters at a constant range (left column) are converted to ratios of diameter to range (center column), from which corresponding ranges can be found for a constant diameter (right column).

D @ 15 miles	D [in]/R [miles]	R @ 24 in.
7	0.47	51.4
9	0.6	40.0
12	0.8	30.0
15	1.0	24.0
18	1.2	20.0
21	1.4	17.1
24	1.6	15.0
30	2.0	12.0

Since the data collected is valid not for a particular diameter or range, but rather for a particular ratio of the two, the results can be used to determine the optimal shape of range variation curves. This is accomplished by plotting the metric data against the range values determined above. When this is done for the SQRInorm, purely linear curves ($R^2 = 1$) are predicted, shown in Figure 64.

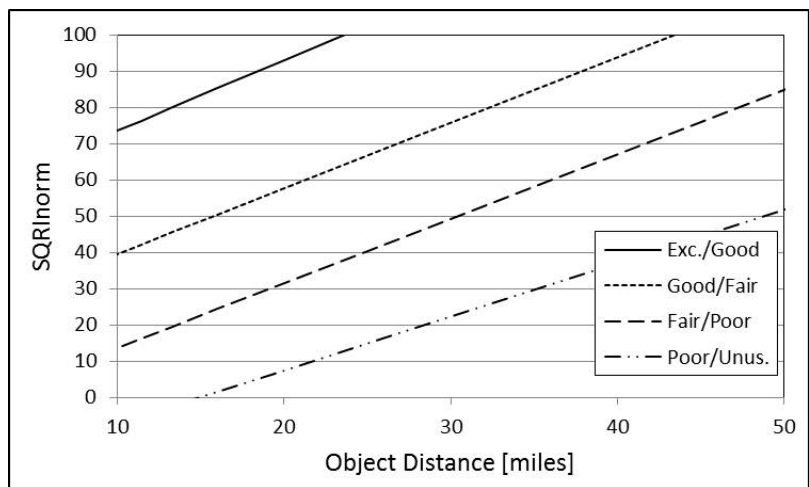


Figure 64. Predicted boundary curve forms of the SQRInorm.

Repeating the process for the TTPnorm yields curves that are non-linear, as shown in Figure 65. Also shown are third order polynomial curves fitted to the predicted data curves. The coefficients of determination from approximating the predicted curve forms by polynomials all exceed 0.99, indicating very high quality fits over the valid data range (object distances corresponding to the values of diameters from 7 inches to 30 inches, and metric values between 0 and 100).

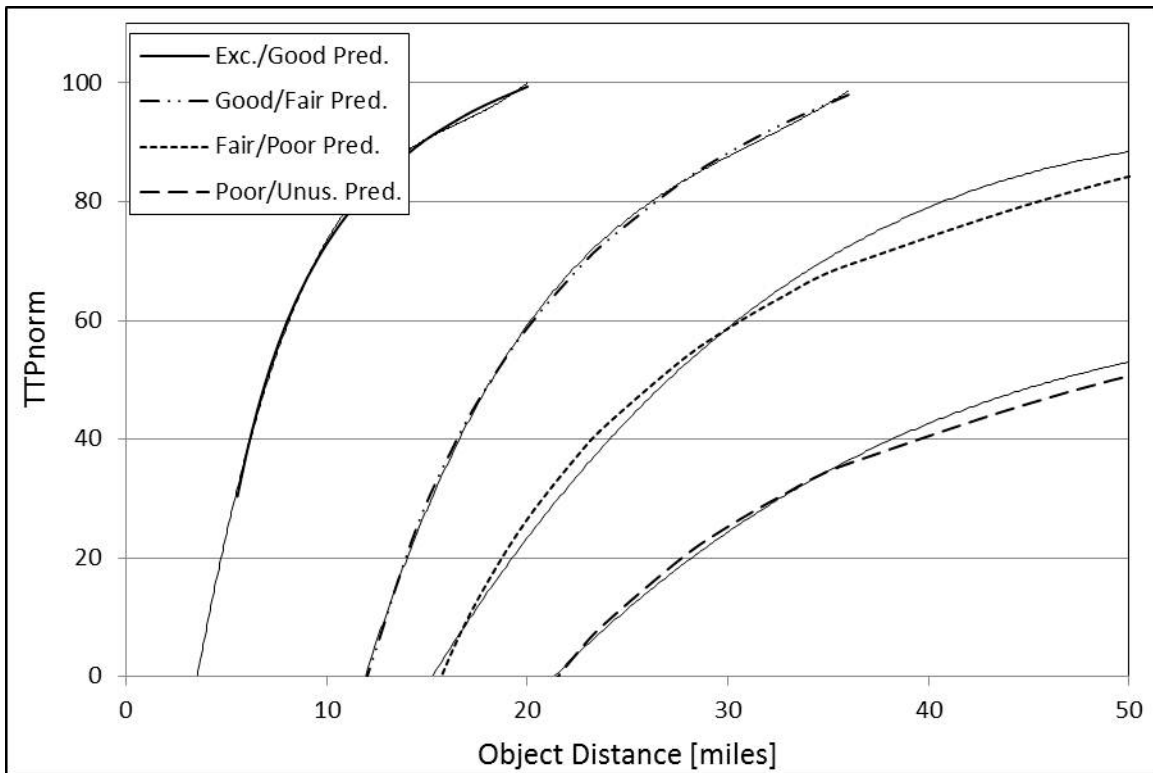


Figure 65. Predicted boundary curve forms of the TTPnorm shown with third order polynomial approximations.

The process is repeated for SQF, again with non-linear results. The predicted range varying boundary curves are fit with third order polynomials, shown in Figure 66. In this case, the

coefficients of determination all exceeded 0.96, and it can be easily seen from the figure why linear curves fit the raw data collected so well.

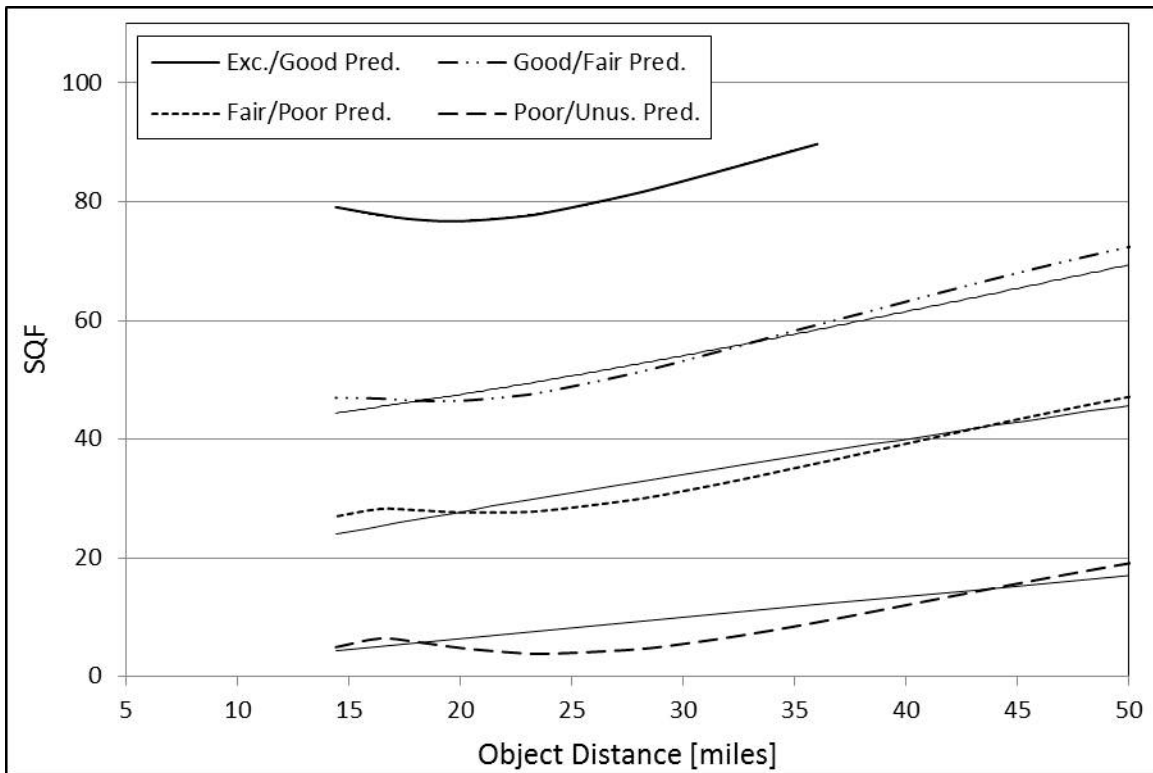


Figure 66. Predicted boundary curve forms of the SQF shown with third order polynomial approximations.

Now having predicted boundary curve forms for the SQRInorm, TTPnorm, and SQF, the data can be fit to the appropriate forms. Since the SQRInorm boundaries are predicted to be linear, the results shown in Figure 61 and Table 19 are valid and need no modifications. The TTPnorm data is fit with second order polynomial curves, although third order polynomial is predicted. This is certainly not a violation of the prediction, but rather, can be considered third order with cubic coefficients of zero. The resulting boundary curves are shown in Figure 67 and

summarized in Table 23. Data fits the predicted curve types quite nicely with the exception of the Poor/Unusable boundary which has only three data points available for fitting. The results validate the boundary curve form found from aperture diameter variation, as well as confirming the predicted object range variation.

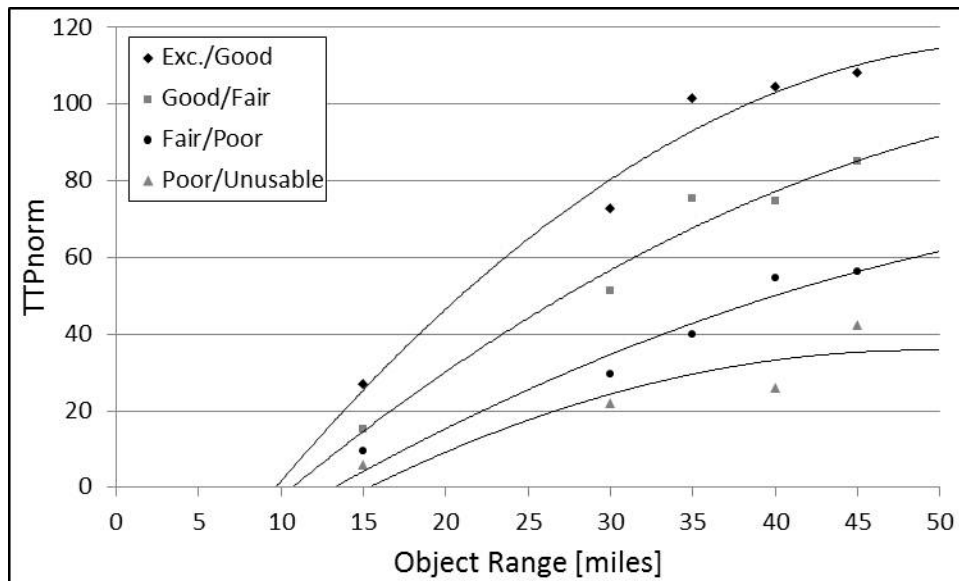


Figure 67. TTPnorm data shown with predicted curve form best fit polynomials.

Table 23. Resulting second order polynomial curves from fitting to the data.

	Quadratic Coeff.	Linear Coeff.	Constant	R ²
Exc./Good	-0.0557	6.169	-54.532	0.9707
Good/Fair	-0.0301	4.1603	-40.968	0.9693
Fair/Poor	-0.0195	2.9081	-35	0.9441
Poor/Unus.	-0.0315	3.0901	-40	0.7813

Unlike the TTPnorm, the SQF requires non-zero coefficients for all three polynomial orders in the data fitting process in order to obtain good fit results. The raw data and best fit third order polynomial curves are shown in Figure 68 and summarized in Table 24. Data fits the predicted curve types reasonably with the exception of the Poor/Unusable boundary, indicating that slight modifications to the diameter variation data and/or the object distance boundaries may be required if the SQF were of particular interest.

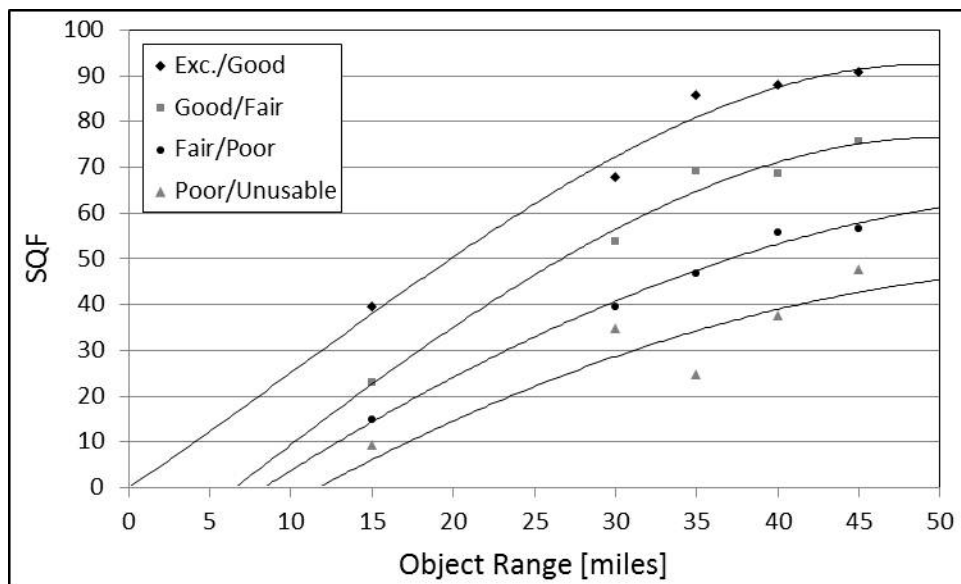


Figure 68. SQF data shown with predicted curve form best fit polynomials.

Table 24. Resulting third order polynomial curves from fitting to the data.

	Cubic Coeff.	Quadratic Coeff.	Linear Coeff.	Constant	R ²
Exc./Good	-0.0006	0.0179	2.3919	0	0.9753
Good/Fair	-0.0004	0.0039	2.7427	-18	0.9809
Fair/Poor	-7.00E-05	-0.0148	2.5285	-20	0.9915
Poor/Unus.	0	-0.019	2.3607	-25	0.8092

11.0 SUMMARY AND CONCLUSIONS

Though many quantitative measures of image quality exist, few account for perceptual effects of the human observer. The three most mature perceptual image quality metrics are the Subjective Quality Factor (SQF), the Square Root Integral (SQRI), and the Targeting Task Performance Metric (TTP), all of which are Modulation Transfer Function (MTF) based. These were introduced in 1971, 1990, and 2004 respectively. The SQF is the least robust of the three, suffering from a poorly approximated Contrast Sensitivity Function (CSF).

Traditionally, MTF-based metrics are evaluated by applying the image plane MTF. This however neglects the image quality change from object distance. By shifting the MTF to the object plane, the object distance-induced quality change can be accounted for. This planar shift is accomplished by simply scaling the spatial frequencies by the appropriate linear magnification terms in the complete optical system. This adjustment is described in Chapter 4.

Also in Chapter 4, modifications to the TTP and SQRI are introduced such that the metrics are normalized to the diffraction-limited values. This creates additional intuitive utility to the metrics, allowing maximum image quality for a given optical system to be quickly determined. This normalization process removes the object distance parameter from the metrics, requiring additional perceptual testing to recover such information. The methods of perceptual testing applied in this research are the Paired Image Comparison Test, and the Categorical Sort Test, both of which are reviewed in Chapter 5.

To best predict the perceived image quality of various telescopes, knowledge of the metric quality dependence on the various parameters is necessary. The metrics are designed to be applied for a single system at a single object distance. As the MTF varies for that given set of parameters, perceived image quality is highly correlated to the metric values. To compare the capability of various telescopes having different parameters, the metric correlation to observer opinions of image quality was previously unknown and required testing. The parameters of interest are obscuration ratio, focal length, aperture diameter, and object distance.

The obscuration ratio varies very little for current Launch Vehicle Imaging Telescopes (LVIT) and is then considered constant for this investigation. Justification for this in terms of MTF variation caused by changes to the obscuration ratio over the limited region of interest was provided graphically in Chapter 7.

In Chapter 8, the focal length was investigated and proven mathematically to not affect the perceived image quality if the displayed image size was fixed, requiring display magnification to compensate for focal length induced changes in optical magnification. This phenomenon was explored experimentally using simulated imagery. For high quality imagery with a constant display size, it was found that no difference in perceived image quality could be detected by observers. For more significantly blurred imagery, the results were less definitive. The reason is hypothesized to be primarily due to interpolation errors caused by the simulation software. Applying real imagery to attempt to validate the focal length invariance of perceived image quality requires images to be magnified, an interpolation-dependent process for digital imagery.

In Chapter 9, the metric effects caused by changing the aperture diameter were investigated. For non-normalized metrics, the TTP and SQRI showed similar forms. The SQF yielded results with far less utility. The normalized TTP and SQRI varied significantly in forms. Nearly all of the metrics and forms thereof included data with negative metric values, causing metric trends to imply the extinction of image quality categories (Excellent, Good, Fair, Poor, or Unusable) at larger aperture diameters. This is counterintuitive and, in fact, inaccurate. The causes of negative metric data and the quality category extinction were discussed.

By using the data acquired through the research, the amount of third order spherical aberration (appropriately balanced with defocus to minimize RMS wavefront error) can be extracted from the metrics. The boundary curves can then be displayed as a function of aperture diameter and spherical aberrations, shown in Figure 69. Here, except for the boundary between Excellent and Good, the data is fit to logarithmic curves. The Excellent/Good boundary fails to follow the form of the other boundaries because of psychological tendencies of observers to shy away from the highest quality category in perceptual testing.

It is true that instead of using the perceptual metrics in the perceptual testing, the spherical aberration could have been used as the metric. This would have yielded Figure 69 directly. However, since the perceptual metrics are generic in terms of aberrations, spherical aberration can be substituted by any aberration or combination of aberrations. Thus curves similar to Figure 69 but with different aberrations can be created by extracting the quantity of aberrations of interest from the SQRI or TTP trends.

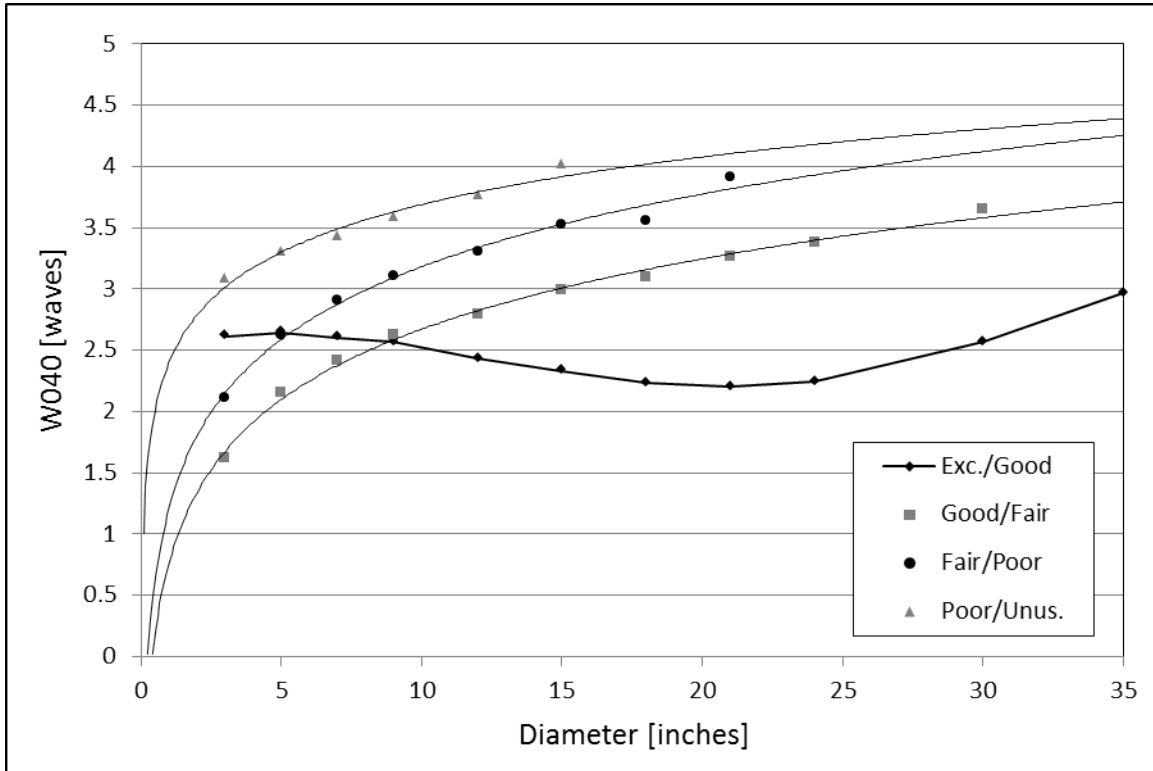


Figure 69. Perceptual image quality boundary curves for spherical aberration as a function of aperture diameter.

By considering the MTF dependence on the aperture diameter and object distance, it can be seen that both act simply to scale the MTF. The manner of scaling of distance and diameter are inverses of each other, indicating that one can be converted to the other. Using the experimentally determined trends of metric versus aperture diameter and converting diameter to object distance, metrics versus object distance predictions were made in Chapter 10. Though the predicted values did not agree explicitly with the experimentally determined values, the curve forms did fit the experimental data quite well. The predicted forms for metric as a function of object distance were then numerically fit to the experimental data.

In a manner similar to that shown in Figure 69, the boundaries are displayed as a function of object distance and spherical aberration. The data is plotted along with logarithmic curves. The curve crossings indicate that significantly outside of the valid, tested range of object distances (15 miles to 45 miles), the model becomes unreliable.

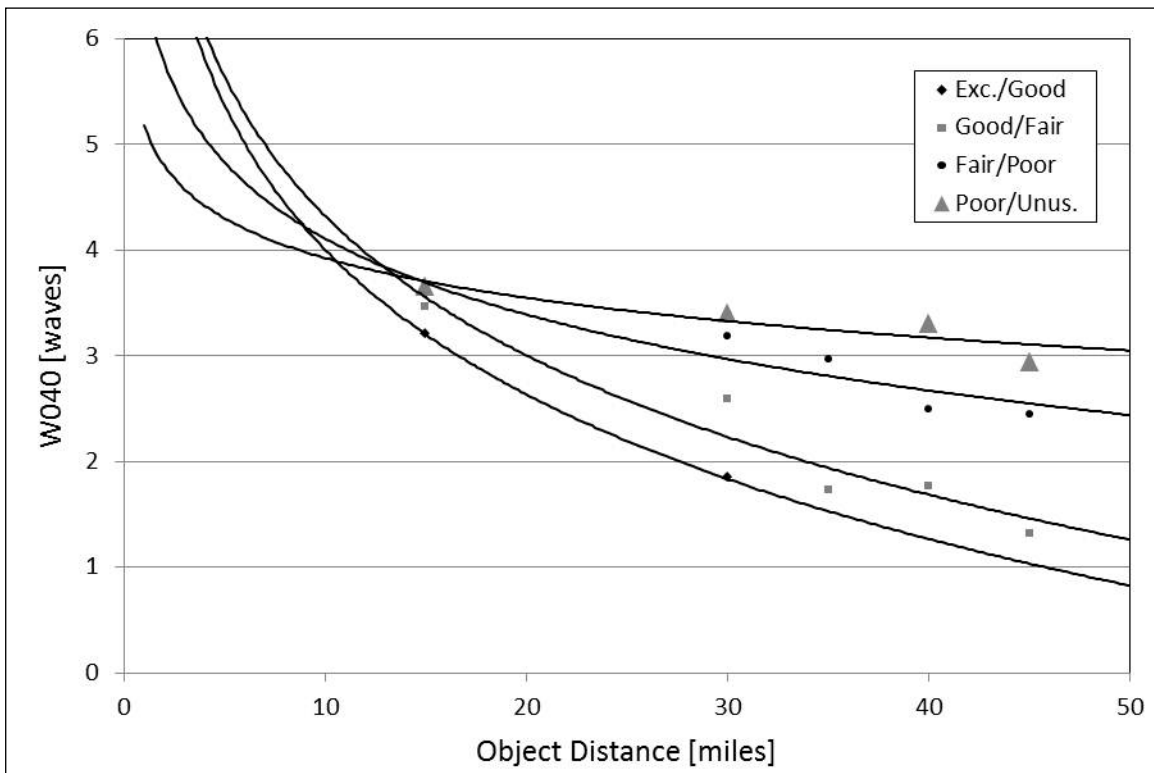


Figure 70. Perceptual image quality boundary curves for spherical aberration as a function of object distance.

It is important that the results obtained from this research not be applied blindly. The assumptions made in Chapter 7 restrict the validity of the results to the following:

1. Telescopes dominated by third and lower order aberrations such that higher order aberrations can be neglected.

2. Achromatic telescopes corrected well enough to ignore lateral and longitudinal chromatic aberrations as well as higher order chromatic effects.
3. Telescopes with narrow enough field such that aberrations can be considered constant across the field.
4. Third order aberrations are always balanced with lower order aberrations such that the RMS wavefront error is minimized.
5. The absence of atmospheric effects is strictly assumed.
6. Vibrations are negligible.
7. Detector and sampling concerns are negligible.

The problem of creating predictions of image quality for various telescopes based on interferometric test results was the goal of the research, and although the above assumptions create an unrealistic scenario, they were necessary to reduce the problem to one which is manageable. Refinements to the model can be made and extension to more realistic conditions can be achieved through additional research. The results of the research presented have yielded a management maintenance decision aid that has been distributed to multiple ranges across the country, and has been awarded three patents.

REFERENCES

1. Atchison, D.A., Smith, George, *Optics of the Human Eye*. 2000, Woburn, MA: Butterworth-Heinemann.
2. Holst, G., *Electro-Optical Imaging System Performance*. 2006, Bellingham, WA: SPIE.
3. Mahajan, V.N., *Strehl ratio for primary aberrations: some analytical results for circular and annular pupils*. *Journal of the Optical Society of America*, 1982. **72**(9): p. 231-239.
4. Geary, J.M., *Introduction to Lens Design*. 2002, Richmond, VA: Willmann-Bell Inc.
5. Keelan, B., *Handbook of Image Quality: Characterization and Prediction*. 2002, New York, NY: Marcel Dekker, Inc.
6. Charman, W.N. and A. Olin, *Tutorial--Image Quality Criteria for Aerial Camera Systems*. *Photog. Sci. Eng.*, 1965. **9**(6): p. 385-397.
7. Riehl, K., *HDOS-Itek Reconnaissance Systems*. SPIE, vol. 2829: p. 322-334.
8. Irvine, J.M., *National Imagery Interpretability Rating Scales (NIIRS): Overview and Methodology*. SPIE, vol.3128: p. 93-103.
9. Crane, E., *An Objective Method for Rating Picture Sharpness: SMT Acutance*. SMPTE, 1964. **73**: p. 643-647.
10. Leachtenauer, J.C., et al., *General Image Quality Equation: GIQE*. *Applied Optics*, 1997: p. 8322-8328.
11. Schade, O., *Electro-Optical Characteristics of Television Systems. Part I: Characteristics of Vision and Visual Systems*. *RCA Review*, 1948. **IX**: p. 5-37.
12. Schade, O., *Electro-Optical Characteristics of Television Systems. Part II: Electro-Optical Specifications for Television Systems*. *RCA Review*, 1948. **IX**: p. 245-286.
13. Schade, O., *Electro-Optical Characteristics of Television Systems. Part III: Electro-Optical Characteristics of Camera Systems*. *RCA Review*, 1948. **IX**: p. 490-530.
14. Schade, O., *Electro-Optical Characteristics of Television Systems. Part IV: Correlation and Evaluation of Electro-Optical Characteristics of Imaging Systems*. *RCA Review*, 1948. **IX**: p. 653-686.

15. Schade, O., *Image Gradation, Graininess and Sharpness in Television and Motion Picture Systems. Part I: Image Structure and Transfer Characteristics*. SMPTE, 1951. **56**: p. 137-171.
16. Schade, O., *Image Gradation, Graininess and Sharpness in Television and Motion Picture Systems. Part II: The Grain Structure of Motion Picture Images--An Analysis of Deviations and Fluctuations of the Sample Number*. SMPTE, 1952. **58**: p. 181-222.
17. Schade, O., *Image Gradation, Graininess and Sharpness in Television and Motion Picture Systems. Part III: The Grain Structure of Television Images*. SMPTE, 1953. **61**: p. 97-164.
18. Schade, O., *Image Gradation, Graininess and Sharpness in Television and Motion-Picture Systems. Part IV: Image Analysis in Photographic and Television Systems*. SMPTE, 1955. **64**(11): p. 593-617.
19. Schade, O., *An Evaluation of Photographic Image Quality and Resolving Power*. SMPTE, 1964. **73**(2): p. 81-119.
20. Kopeika, N., *A System Engineering Approach to Imaging*. 1998, Bellingham, WA: SPIE.
21. Burke, M.W., *Image Acquisition Handbook of Machine Vision Engineering Vol.1*. 1996, The Alden Press: Oxford, Great Britain.
22. Lamberts, R.L., G.C. Higgins, and R.N. Wolfe, *Measurement and analysis of the distribution of energy in optical images*. J. Opt. Soc. Am., 1958. **48**: p. 487-490.
23. Ingelstam, E., *Nomenclature for Fourier transforms of spread functions*. J. Opt. Soc. Am., 1961. **51**: p. 1441.
24. Lamberts, R.L., *Relationship between the sine-wave response and the distribution of energy in the optical image of a line*. J. Opt. Soc. Am., 1958. **48**: p. 490-495.
25. Lamberts, R.L., *Measurement of sine-wave response of a photographic emulsion*. J. Opt. Soc. Am., 1959. **49**: p. 425-428.
26. Lamberts, R.L., *Sine-wave response techniques in photographic printing*. J. Opt. Soc. Am., 1961. **51**: p. 982-987.
27. Lamberts, R.L., *Application of Sine-Wave Techniques to Image-Forming Systems*. SMPTE, 1962: p. 635-640.
28. Snyder, H. *Modulation Transfer Function Area as a Measure of Image Quality*. in *Visual Search*. 1970.
29. Bracewell, R.N., *The Fourier Transform and Its Applications*. 2000: McGraw-Hill Companies.

30. Granger, E.M. and K.N. Cupery, *An optical merit function (SQF), which correlates with subjective image judgments*. Photogr. Sci. Eng., 1972. **16**: p. 221-230.
31. Rogers, H.F. *Development of a Picture Sharpness Test for Still Cameras*. in *Photogr. Opt. Sys. Eval. Seminar*. 1967: SPIE.
32. Donofrio, R.L., *A New Approach to Determining The Image Response of a Color Picture Tube*, in *IEEE Transactions on Broadcast and Television Receivers*. 1973. p. 143-148.
33. Snyder, H.L., *Image Quality and Observer Performance*, in *Perception of Displayed Information*, L.M. Biberman, Editor. 1973, Plenum Press: New York, NY.
34. Navajas, D., et al., *Evaluation of polychromatic image quality by means of transfer function*. Journal of Optics, 1982. **13**(5): p. 283-288.
35. Juvells, I., et al., *Numerical evaluation of the two-dimensional modulation transfer function by means of spot diagram. Comparison with experimental measurements*. Journal of Optics (Paris), 1983. **14**(6): p. 293-297.
36. Bosch, S., I. Juvells, and J.R.D.F. Moneo, *Polychromatic MTF-based criteria for evaluating photographic image quality*. OPTICA ACTA, 1985. **32**(11): p. 1397-1405.
37. Bosch, S., I. Juvells, and F. Abbad, *Volume defined by the two-dimensional modulation transfer function surface: Approximation obtained from its sagittal and tangential sections. Application to image quality criteria* Journal of Optics (Paris), 1985. **16**(5): p. 219-223.
38. Barten, P.G., *Evaluation of subjective image quality with the square-root integral method*. J. Opt. Soc. Am., 1990: p. 2024-2031.
39. L Desponds, C.D., M Grecescu, C Hessler, A Samiri and J F Valley, *Image quality index (IQI) for screen-film mammography*. Phys. Med. Biol., 1991. **36**: p. 19-33.
40. Gonzalez, R.C. and R.E. Woods, *Digital Image Processing (3rd Edition)*. 2008, Upper Saddle River, NJ: Pearson Prentice Hall.
41. Eskicioglu, A.M. and P.S. Fisher, *Image Quality Measures and Their Performance*. 1995. **43**(12).
42. Westen, S.J.P., R.L. Legendijk, and J. Biemond. *Perceptual image quality based on a multiple channel HVS model*. in *Proceedings of ICASSP 1995*. Detroit, MI.
43. Wang, Z. and A.C. Bovik, *A universal image quality index*. IEEE Signal Processing Letters, 2002. **9**(3): p. 81-84.

44. Liu, M. and X. Yang, *A New Image Quality Approach Based on Decision Fusion*, in *Fifth International Conference on Fuzzy Systems and Knowledge Discovery*. 2008: Jinan Shandong. p. 10-14.
45. Medda, A. and V. DeBrunner, *Color Image Quality Index Based on the UIQI*, in *Proceedings of the 2006 IEEE Southwest Symposium on Image Analysis and Interpretation*. 2006, IEEE Computer Society.
46. Yi, Y., et al., *Image Quality Assessment Based on Structural Distortion and Image Definition*, in *2008 International Conference on Computer Science and Software Engineering*. 2008.
47. Sakuldee, R., N. Yamsang, and S. Udomhunsakul, *Image Quality Assessment for JPEG and JPEG2000*, in *Proceedings of the 2008 Third International Conference on Convergence and Hybrid Information Technology - Volume 01*. 2008, IEEE Computer Society.
48. Martens, J.-B. and L. Meesters, *Image dissimilarity*. *Signal Process.*, 1998. **70**(3): p. 155-176.
49. Miyahara, M., K. Kotani, and V.R. Algazi, *Objective picture quality scale (PQS) for image coding*. *IEEE Transactions on Communications*, Sept 1998. **46**(9): p. 1215-1226.
50. Algazi, V.R., et al., *Important distortion factors in the encoding of very high quality images*, in *Applications of Digital Image Processing XVII*, A.G. Tescher, Editor. 1994, SPIE. p. 2-12.
51. Silva, E.A., P. Karen, and S.S. Agaian. *Quantifying image similarity using measure of enhancement by entropy*. 2007: SPIE.
52. Shnayderman, A., A. Gusev, and A.M. Eskicioglu, *An SVD-based grayscale image quality measure for local and global assessment*. *IEEE Transactions on Image Processing*, 2006. **15**(2): p. 422-429.
53. Chandler, D.M. and S.S. Hemami, *VSNR: A Wavelet-Based Visual Signal-to-Noise Ratio for Natural Images*. *IEEE Transactions on Image Processing* 2007. **16**(9): p. 2284-2298.
54. Lu, Q., L. Du, and X. Xiao, *An Edge Weighted RS image Quality Evaluation Method*, in *International Conference on Computer Science and Software Engineering*. 2008. p. 197-200.
55. Sendashonga, M. and F. Labeau, *Low Complexity Image Quality Assessment Using Frequency Domain Transforms*, in *2006 IEEE International Conference on Image Processing* 2006. p. 385-388.
56. Carnec, M., P.L. Callet, and D. Barba, *Objective quality assessment of color images based on a generic perceptual reduced reference*. *Image Commun.*, 2008. **23**(4): p. 239-256.
57. Wang, S., et al., *An accurate method for image quality evaluation using digital watermarking*. *IEICE Electronics Express*, 2005. **2**(20): p. 523-529.

58. Sazzad, Z.M.P., Y. Kawayoke, and Y. Horita, *No reference image quality assessment for JPEG2000 based on spatial features*. *Image Commun.*, 2008. **23**(4): p. 257-268.
59. Lee, B. and J. Harris, *Contrast Transfer Characteristics of Visual Short-term Memory*. *Vision Res.*, 1996. **36**(14): p. 2159-2166.
60. I. Sanz and M. L. Calvo, M.C., V. Lakshminarayanan, *Perception of High-Contrast Blurred Edges*. *Journal of Visual Communication and Image Representation*, 2001. **12**: p. 240-254.
61. *ISO 20462-1 Photography — Psychophysical experimental methods for estimating image quality —Part 1:Overview of psychophysical elements*. 2005.
62. *ISO 20462-2 Photography — Psychophysical experimental methods for estimating image quality —Part 2:Triplet comparison method*. 2005.
63. *ISO 20462-3 Photography — Psychophysical experimental methods for estimating image quality —Part 3:Quality ruler method*. 2005.
64. Keelan, B. and U. Hitoshi. *ISO 20462: a psychophysical image quality measurement standard*. in *Image Quality and System Performance*. 2003: SPIE.
65. Richard H. Vollmerhausen, E.J., Ronald G. Driggers, *New metric for predicting target acquisition performance*. *Optical Engineering*, 2004. **43**(11): p. 2806-2818.
66. Richard H. Vollmerhausen, T.B. *Using a targeting metric to predict the utility of an EO imager as a pilotage aid*. in *Infrared Imaging Systems: Design, Analysis, Modeling, and Testing XVII*. 2006: SPIE.
67. H. Barrett, K.M., *Foundations of Image Science*. 2004, Hoboken, NJ: Wiley.
68. Gaskill, J., *Linears Systems, Fourier Transforms, and Optics*. 1978, New York, NY: Wiley.
69. Wu, H.R. and K.R. Rao, *Digital Video Image Quality and Perceptual Coding*. 2006.
70. Engeldrum, P.G., *Psychometric Scaling: A Toolkit for Imaging Systems Development*. 2004: Marcel Dekker, Inc.
71. Torgerson, W.S., *Theory and Methods of Scaling*. 1958: John Wiley & Sons, Inc.